

1

CAMPINAS STATE UNIVERSITY

2

DOCTORAL THESIS

3

4 **Search of Z and Higgs boson decaying into $\Upsilon + \gamma$**
5 **in pp collisions at CMS/LHC**

6

7 *Author:*

Felipe Torres da Silva de Araujo

Supervisor:

Dr. José Augusto Chinellato

Co-Supervisor:

Dr. Alberto Franco de Sá Santoro

8

*A thesis submitted in fulfillment of the requirements
for the degree of Doctor of Physics*

10

in the

11

Graduate Program of
"Gleb Wataghin" Institute of Physics

12

13

August 10, 2020

¹⁴ “Sometimes science is a lot more art than science. A lot of people don’t get that.”

¹⁵

Rick Sanchez

¹⁶ “Então, que seja doce. Repito todas as manhãs, ao abrir as janelas para deixar entrar o sol ou o
¹⁷ cinza dos dias, bem assim, que seja doce. Quando há sol, e esse sol bate na minha cara amassada do
¹⁸ sono ou da insônia, contemplando as partículas de poeira soltas no ar, feito um pequeno universo;
¹⁹ repito sete vezes para dar sorte: que seja doce que seja doce que seja doce e assim por diante. Mas,
²⁰ se alguém me perguntasse o que deverá ser doce, talvez não saiba responder. Tudo é tão vago como
²¹ se fosse nada.”

²²

Caio Fernando Abreu

23 CAMPINAS STATE UNIVERSITY

24 *Abstract*

25 "Gleb Wataghin" Institute of Physics

26 Doctor of Physics

27 **Search of Z and Higgs boson decaying into $\Upsilon + \gamma$ in pp collisions at CMS/LHC**

28 by Felipe Torres da Silva de Araujo

29 Searches for Standard Model Higgs and Z bosons decaying to a $\Upsilon(1S, 2S, 3S)$ and a photon, with
30 subsequent decay of the $\Upsilon(1S, 2S, 3S)$ to $\mu^+ \mu^-$ are presented. The analyses is performed using
31 data recorded by CMS detector from proton-proton collisions at center-of-mass energy of 13 TeV
32 corresponding to an integrated luminosity of 35.86 fb^{-1} . We put a limit, 95% confidence level, on
33 $H \rightarrow \Upsilon(1S, 2S, 3S) + \gamma$ decay branching fraction at $(6.8, 7.1, 6.0) \times 10^{-4}$ and on $Z \rightarrow \Upsilon(1S, 2S, 3S) +$
34 γ decay branching fraction at $(2.6, 2.3, 1.3) \times 10^{-6}$. Contributions to operation, maintenance and
35 R&D of Resistive Plate Chambers (RPC) of CMS are also presented. **EXPANDIR**

DRAFT

36

Acknowledgements

37 I would like to thank:

- 38 • the Campinas State University for providing the institutional support for this study;
- 39 • the Rio de Janeiro State University for the cooperation with Campinas State University in
40 their high-energy physics program. This was a key factor for this study;
- 41 • the National Council for Scientific and Technological Development (CNPq) for the financial
42 support for this work;
- 43 • the European Laboratory for Particle Physics (CERN) for the construction and operation of
44 the Large Hadron Collider (LHC);
- 45 • the Compact Muon Solenoid (CMS) collaboration for the construction, operation and provi-
46 sion of the instrumental means for this study.

DRAFT

47 Contents

48	Abstract	iii
49	Acknowledgements	v
50	1 Introduction	1
51	2 Rare Z and Higgs decays to quarkonia	3
52	2.1 Standard Model and Local Gauge Invariance	3
53	2.2 Recent results	7
54	3 Experimental Setup	9
55	3.1 Tracker	10
56	3.2 Electromagnetic Calorimeter	10
57	3.3 Hadronic Calorimeter	10
58	3.4 Muon System	10
59	3.4.1 DT	10
60	3.4.2 CSC	10
61	3.4.3 RPC	10
62	3.4.4 GEN	10
63	3.5 Trigger and Data Acquisition	10
64	3.6 Simulation, reconstruction and computing	10
65	3.7 Particle Flow Algorithm	10
66	4 Physics Analysis	11
67	4.1 Datasets and simulated events	11
68	4.1.1 Data samples	11
69	4.1.2 Simulated datasets	11
70	4.2 Contribution of the $\Upsilon(nS)$ polarisation	13
71	4.3 Kinematical studies using MC generator	13
72	4.4 Event selection	17
73	4.5 Trigger and physics object selection (Group I)	17
74	4.5.1 Trigger	17
75	4.5.2 Muon Identification	17
76	4.5.3 Photon Identification	19
77	4.5.4 Kinematical distributions	19
78	4.6 Kinematical selection (Group II)	29

79	4.7	Event categorization and yields	37
80	4.7.1	R9 reweighting	37
81	4.7.2	Event counting and yields	37
82	4.8	Background modeling	39
83	4.9	Signal modeling	47
84	4.10	Systematic uncertainties	53
85	4.10.1	Uncertainties on the predicted signal yields	53
86	4.10.2	Uncertainties that affect the signal fits	54
87	4.11	Modeling Cross checks	57
88	5	Results and conclusion	63
89	5.1	The CL_s formalism for upper limits setting at CMS	63
90	5.2	Branching fraction upper limits	63
91	6	CMS Resistive Plate Chambers - RPC	65
92	6.1	Resistive Plate Chambers	65
93	6.2	CMS Resistive Plate Chambers	65
94	6.2.1	Electronics and Readout	67
95	6.2.2	Performance	67
96	6.3	RPC Operation - Shifts and Data Certification	68
97	6.4	RPC Online Software	69
98	6.5	iRPC R&D	70
99	6.6	LS2 and the RPC Standard Maintenance	76
100	6.6.1	HV maintenance	76
101	6.6.2	LV and control maintenance	77
102	6.6.3	Detector commissioning	78
103	Bibliography		81

¹⁰⁴ 1 Introduction

¹⁰⁵ INTRODUÇÃO
¹⁰⁶ USAR UM PAPER DE CMS MUON PERFORMANCE PARA DIZER PORQUE
¹⁰⁷ TRABALHAR COM DETECTORES DE MUONS

DRAFT

¹⁰⁸ 2 Rare Z and Higgs decays to quarkonia

¹⁰⁹ 2.1 Standard Model and Local Gauge Invariance

¹¹⁰ Physics understands the matter and how it interacts in terms of two components: four funda-
¹¹¹ mentals forces and elementary particles. From the weakest to the strongest, the fundamental forces
¹¹² are: gravitational, weak, electromagnetic and strong. All share common characteristics like, being
¹¹³ mediated by particles ¹, being relevant within some effective range and have a associate a charge-like
¹¹⁴ quantity (i.e. intrinsic characteristic of the object) that defines whether or not, particles might be
¹¹⁵ subjected to a specific interaction.

¹¹⁶ Along with the fundamental interactions, the Standard Model (or simply *SM*) defines every
¹¹⁷ existing matter in the Universe as a set of fundamental quantum objects, with properties that define
¹¹⁸ their interaction. Those objects are said to be fundamental since, in the context of the SM, they
¹¹⁹ are the smallest possible components of matter. We shall refer to them as fundamental particles.
¹²⁰ There four of those mediating particles (force carriers), gluon (g - for the strong interaction), photon
¹²¹ (γ - for the electromagnetic interaction), Z and W (for weak interaction), all of them being vector
¹²² bosons (spin 1). Besides the interaction mediators, described at Table 2.1, the fundamental particles
¹²³ are divided in two groups (*quarks* and *leptons*), with three generations, each. These are not force
¹²⁴ carriers, but elementary particles, endowed with charge-like characteristics that allow them to by
¹²⁵ exchange the vector bosons. Those are the building blocks of Matter in our Universe.

¹²⁶ Figure 2.1 summarizes their properties. Table 2.1 presents the relative strength and effective
¹²⁷ range, for each one of the four fundamental interactions. The gravitational force is not study subject
¹²⁸ of the Standard Model.

Table 2.1: Relative strength (with respect to the strong force) and effective range of action for the four fundamentals interactions.

	Mediator	Relative Strength	Effective Range
Gravitational	Graviton	10^{-41}	∞
Weak	W and Z bosons	10^{-16}	10^{-18} m
Electromagnetic	Photon	10^{-3}	∞
Strong	gluons	1	10^{-15} m

¹²⁹ There are six quark, up and down (u and d - first generation), charm and strange (c and s -
¹³⁰ second generation), top and bottom (t and b - first generation), in increasing invariant mass order
¹³¹ of the generations. Since they interact thought all the three fundamental forces of the SM, they are
¹³² said to possess electrical charge, flavour and color. Their generational counterparts, the leptons,

¹There is no evidence of the existence of the Graviton (force carrier associated to the gravitational force), even though, it is theorized by models that wish to comprehend gravity in a quantum perspective.

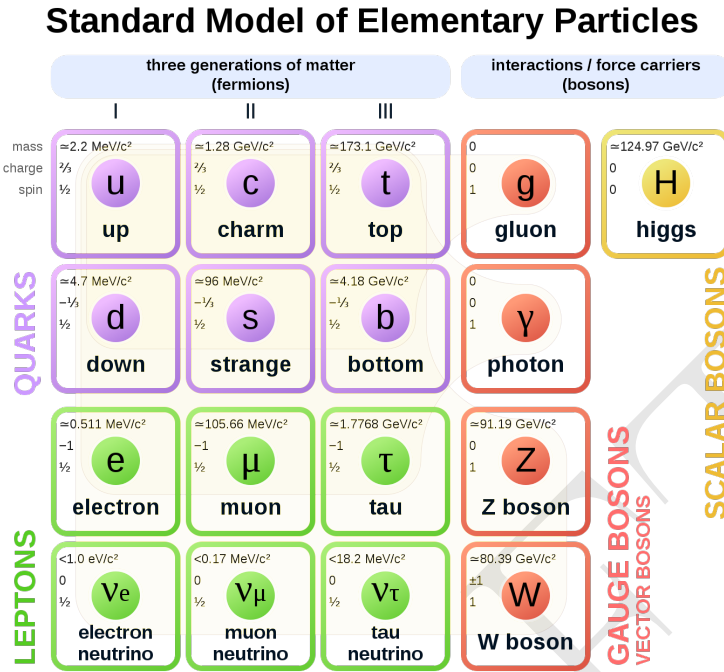


Figure 2.1: Elementary particles of the Standard Model, with their masses charges and spin. Those particles can be divided in two classes: boson (the interaction/force carriers) and the fermions, which are divided in three generations. Source: [1].

133 don't interact via strong interaction, that is why they are said to have only flavours and electric
 134 charge. The leptons are electron and electron neutrino (e and ν_e - first generation), muon and muon
 135 neutrino (μ and ν_μ - second generation) and tau and tau neutrino (τ and ν_τ - third generation).
 136 The neutrinos, within the SM, are massless, even though, experimental measurements have shown
 137 that they actually have mass [2]. Neutrinos are also electrically neutral, meaning that they only
 138 interact through weak interactions.

139 Figure 2.1 also presents the Higgs Boson (H) which is part of the SM and shall be discussed
 140 later.

141 Within the Standard Model, the theoretical basis that describe the fundamental interactions are
 142 derived from a common principle: the local gauge invariance. According to Salam and Ward [3]:

143 "Our basic postulate is that it should be possible to generate strong, weak and electro-
 144 magnetic interaction terms [...], by making local gauge transformations on the kinetic-
 145 energy terms in the free Lagrangian for all particles."

146 Taking the Quantum Electrodynamics (QED) as an example: the quantum field theory that
 147 describes the x

148 The fundamental theories that compose the Standard Model are all derived from a fundamental
 149 principle call

150 The electromagnetic force, in the context of fundamental interactions, is describe by a gauge
 151 theory called quantum electrodynamics.

152 **Electroweak**

Higgs discovery Production modes Decay modes
Yukawa coupling
Higgs results at CMS

The rare decays of the Higgs boson [4, 5] to a quarkonium state and a photon provide a unique sensitivity to the magnitude of the Yukawa couplings of the Higgs boson to quarks [6–8]. These couplings are difficult to access on hadronic collisions through direct decay of Higgs in quark-antiquark, due to the immense background from QCD [9].

Among the channels available to explore Yukawa’s couplings of light quarks [7, 8] are those with heavy-quarkonia. The rare modes of decay of the Z boson have attracted attention focused on establishing its sensitivity to New Physics [10], being configured as an alternative environment to investigate the Yukawa couplings of the Higgs boson.

Also, the exclusive rare decays of vector bosons (Z, W) provide a favorable environment for testing the factorization of QCD, thus allowing an approach in a context where the power of corrections are definitely under control. The main focus of this kind of analysis are the hadronic radioactive decays, $Z \rightarrow M\gamma$, where M can be a pseudoscalar or a vector meson ($J/\psi, \phi, \Upsilon_n$).

They offer the perfect way to explore some of the leading order properties of the light-cone distribution amplitudes (LCDAs) [11] of several mesons, but they present a difficulty, considering that in the LHC energy scale the branching ratio of these processes is very small. There are theoretical predictions [12, 13] that point out a branching ratio for several decay channels in the Standard Model, as shown in the Table 2.2.

Physics Processes	Branching Ratio (BR_{SM}):
$H \rightarrow \Upsilon(1S) + \gamma$	5.22×10^{-9}
$H \rightarrow \Upsilon(2S) + \gamma$	1.42×10^{-9}
$H \rightarrow \Upsilon(3S) + \gamma$	9.10×10^{-10}
$Z \rightarrow \Upsilon(1S) + \gamma$	4.88×10^{-8}
$Z \rightarrow \Upsilon(2S) + \gamma$	2.44×10^{-8}
$Z \rightarrow \Upsilon(3S) + \gamma$	1.88×10^{-8}

Table 2.2: Summary of cross section and branching ratio for $H/Z \rightarrow \Upsilon(1S, 2S, 3S) + \gamma \rightarrow \mu^+ \mu^- + \gamma$ analysis. The effective cross-section will be discussed in section 4.1.2.

Recent studies on exclusive Higgs boson decays [14–16] in final states containing a simple vector meson and a photon have caused interest in these physics topics. It was proposed to use these decays as a possible way to explore non-standard Yukawa couplings of the Higgs boson. Such measures are quite challenging in the LHC environment. The observation of hadronic decays of vector bosons provides could provide a new frontier for the nature of heavy quarkonia production in hadronic collisions.

Along the same lines, the simple exploration of rare SM decays, even in scenarios where anomalous couplings are, in principle, ruled out by direct measurements [17], as in the case of this analysis ($H \rightarrow \Upsilon(nS) + \gamma$), are still important as a stress test of the SM and as reference for future measurements. Specially the later one, when you consider that the small predicted cross sections from Table 2.2, most probably, would imply that an observation of this decay would be unlikely even in the HL-LHC [18].

This measurement is sensitive to the direct and indirect production (Figure 2.2). The *direct* process consists in the decay of boson (Higgs or Z) to a quark anti-quark pair, in which, one of the quarks radiates a photon and the pair hadronizes to a meson (a $\Upsilon(nS)$, for this study), while in *indirect* process, the decay happens to a $\gamma\gamma^*(Z)$, with the subsequent decay of the $\gamma^*(Z)$ to a quark anti-quark that hadronizes.

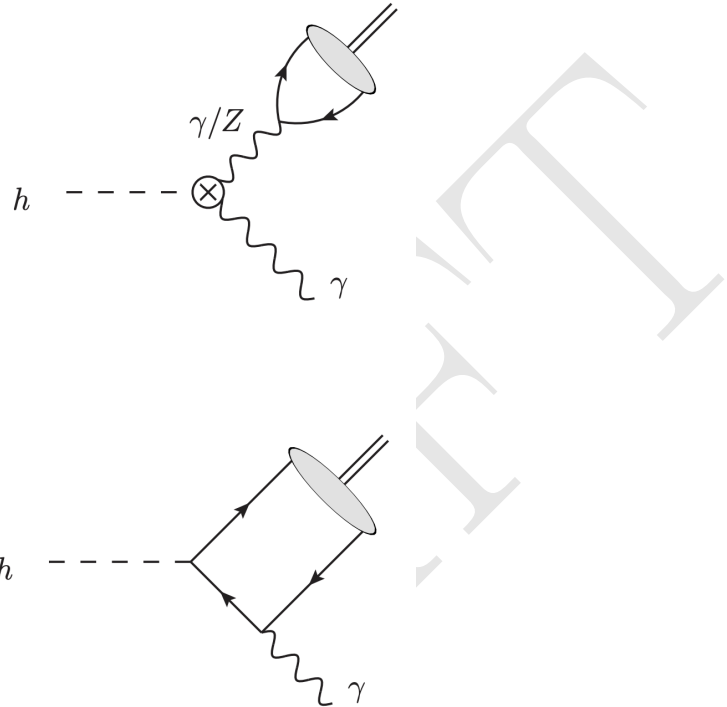


Figure 2.2: Example of leading order diagrams for the indirect (top) and direct (bottom) production mechanisms. In the diagrams, the h can also be understood as a Z boson.

Clearly, only the direct process is sensible to the Yukawa coupling of the boson with the quarks, but, since both processes are indistinguishable in their final state, the indirect process needs to be taken into account. In this study, a dimuon final state is used to tag the $\Upsilon(nS)$.

Even though there are different theoretical predictions for the cross section of this process and its twin brother ($H \rightarrow J/\Psi + \gamma$), each one taking into account different levels of complexity, the 2013 paper [6], from G. Bodwin, F. Petriello, S. Stoynev and M. Velasco, summarizes very well and in a simpler manner, the most relevant phenomenological results on these decays. For the decay to $J/\Psi + \gamma$, the quantum interference with the indirect amplitude, enhances the directed production, leading to a larger, and potentially observable, cross section. This is not true for the $\Upsilon(nS) + \gamma$ decay, since the interference is destructive, diminishing the cross sections.

Another interesting aspect of this study is that, for both $Hc\bar{c}$ and $Hb\bar{b}$ direct coupling measurements are not sensible to the sign of the Yukawa coupling, while the presence of the indirect process in the $H \rightarrow M + \gamma$ (M standing for J/Ψ or $\Upsilon(nS)$) decays resolve this ambiguity.

Finally, since the $\Upsilon(nS) + \gamma$ decay has a much smaller cross section, because of the destructive quantum interference between direct and indirect production mechanisms, a small deviation in the $Hb\bar{b}$ Yukawa coupling, can lead a large increase in the expected branching ratio, making this channel

206 sensible any non-Standard Model process that might interfere in this final state. This becomes clear
 207 when we look to Figure 2.3.

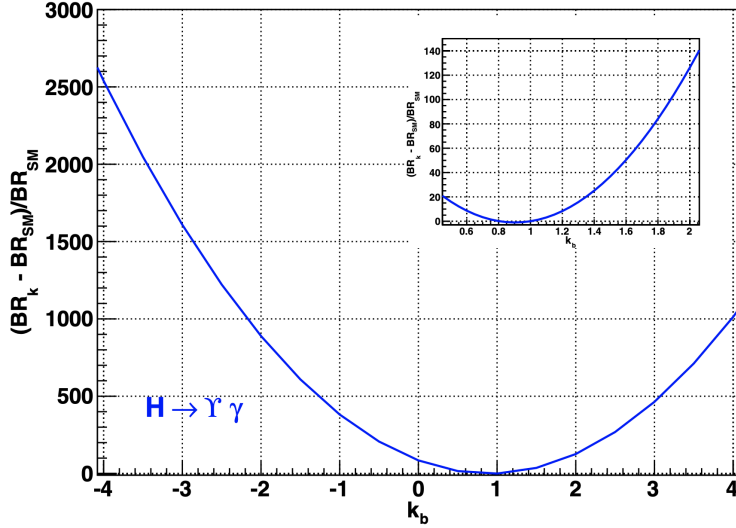


Figure 2.3: Expected relative variation of the branching ratio for the $H \rightarrow \Upsilon(nS) + \gamma$ to k_b , where $k_b = g(Hb\bar{b})/g(Hb\bar{b})_{SM}$ is the ratio for the observed and expected Yukawa coupling oh $Hb\bar{b}$. [6]

208 2.2 Recent results

209 The ATLAS experiment [19] already have two results on this decays [20, 21]. The first one
 210 corresponds to data taken from 2015, while the former one, corresponds to data from 2016 (the
 211 same data taking period to which this study refers).

212 The what concerns the most updated result, the study corresponded to 36.1 fb^{-1} at $\sqrt{s} = 13$
 213 TeV and no significant excess was found by the experiment. Upper limits for the were obtained,
 214 assuming the Standard Model branching fractions predictions, at 95% confidence level, according
 215 to table 2.3.

Decay	\mathcal{BF} at 95% CL
$H \rightarrow J/\Psi + \gamma$	$< 4.5 \times 10^{-4}$
$H \rightarrow \Psi(2S) + \gamma$	$< 2.0 \times 10^{-3}$
$H \rightarrow \Upsilon(1S) + \gamma$	$< 4.9 \times 10^{-4}$
$H \rightarrow \Upsilon(2S) + \gamma$	$< 5.9 \times 10^{-4}$
$H \rightarrow \Upsilon(3S) + \gamma$	$< 5.7 \times 10^{-4}$
<hr/>	
$Z \rightarrow J/\Psi + \gamma$	$< 2.3 \times 10^{-6}$
$Z \rightarrow \Psi(2S) + \gamma$	$< 4.5 \times 10^{-6}$
$Z \rightarrow \Upsilon(1S) + \gamma$	$< 2.8 \times 10^{-6}$
$Z \rightarrow \Upsilon(2S) + \gamma$	$< 1.7 \times 10^{-6}$
$Z \rightarrow \Upsilon(3S) + \gamma$	$< 4.8 \times 10^{-6}$

Table 2.3: Observed upper limits, by the ATLAS experiment, on the branching fractions for the Higgs and Z decays (last result). Detailed comparisons with the results obtained in this study will be presented in chapter 5.

216 It is worth it to mention that the ATLAS papers present a broader analysis, including the decays
 217 to $J/\Psi + \gamma$ and $\Psi(2S) + \gamma$.

218 CMS [22] also have a result on $J/\Psi + \gamma$ and $\Psi(2S) + \gamma$ decay channel, of the Higgs and Z
 219 boson [23]. The observed upper limit on the branching fraction for these decays are presented in
 220 table 2.4.

Channel	Polarization	$\mathcal{B}F$ at 95% CL
$Z \rightarrow J/\Psi + \gamma$	Unpolarized	$< 1.4 \times 10^{-6}$
	Transverse	$< 1.5 \times 10^{-6}$
	Longitudinal	$< 1.2 \times 10^{-6}$
$H \rightarrow J/\Psi + \gamma$	Transverse	$< 7.6 \times 10^{-4}$

Table 2.4: Observed upper limits, by CMS, on the branching fractions for the Higgs and Z decays. The number are compatible with the ones obtained by ATLAS. The results presented for different polarization scenarios of the J/Ψ .

221 No result on the Z and Higgs decays to $\Upsilon(nS) + \gamma$ have been published by CMS, yet.

222 The results presented here, are a subset of a broader topic related to the rare decays of Standard
 223 Model (SM) boson, involving quarkonia. Sticking only to CMS results, we can cite:

- 224 • Search for Higgs and Z boson decays to J/ψ or Υ pairs in proton-proton collisions at $\sqrt{s} =$
 225 13 TeV [24].
- 226 • Observation of the $Z \rightarrow \psi\ell^+\ell^-$ decay in pp collisions at $\sqrt{s} = 13$ TeV [25]. This one specifically,
 227 is the first observation a such decay, involving a Z boson.

228 **verificar resultados se outros foram publicados.**

²²⁹ 3 Experimental Setup

²³⁰ The central feature of the CMS apparatus is a superconducting solenoid of 6 m internal diameter,
²³¹ providing a magnetic field of 3.8 T. Within the solenoid volume are a silicon pixel and strip tracker,
²³² a lead tungstate crystal electromagnetic calorimeter (ECAL), and a brass and scintillator hadron
²³³ calorimeter (HCAL), each composed of a barrel and two endcap sections. Forward calorimeters ex-
²³⁴ tend the pseudorapidity coverage provided by the barrel and endcap detectors. Muons are detected
²³⁵ in gas-ionization chambers embedded in the steel flux-return yoke outside the solenoid.

²³⁶ The silicon tracker measures charged particles within the pseudorapidity range $|\eta| < 2.5$. It
²³⁷ consists of 1440 silicon pixel and 15 148 silicon strip detector modules. For non-isolated particles of
²³⁸ $1 < p_T < 10 \text{ GeV}$ and $|\eta| < 1.4$, the track resolutions are typically 1.5% in p_T and 25–90 (45–150) μm
²³⁹ in the transverse (longitudinal) impact parameter [26]

²⁴⁰ The ECAL consists of 75 848 lead tungstate crystals, which provide coverage in pseudorapidity
²⁴¹ $|\eta| < 1.48$ in a barrel region (EB) and $1.48 < |\eta| < 3.0$ in two endcap regions (EE). Preshower
²⁴² detectors consisting of two planes of silicon sensors interleaved with a total of $3X_0$ of lead are
²⁴³ located in front of each EE detector [27]. In the barrel section of the ECAL, an energy resolution of
²⁴⁴ about 1% is achieved for unconverted or late-converting photons that have energies in the range of
²⁴⁵ tens of GeV. The remaining barrel photons have a resolution of about 1.3% up to a pseudorapidity
²⁴⁶ of $|\eta| = 1$, rising to about 2.5% at $|\eta| = 1.4$. In the endcaps, the resolution of unconverted or late-
²⁴⁷ converting photons is about 2.5%, while the remaining endcap photons have a resolution between
²⁴⁸ 3 and 4% [28]. When combining information from the entire detector, the jet energy resolution
²⁴⁹ amounts typically to 15% at 10 GeV, 8% at 100 GeV, and 4% at 1 TeV, to be compared to about
²⁵⁰ 40%, 12%, and 5% obtained when the ECAL and HCAL calorimeters alone are used.

²⁵¹ Muons are measured in the pseudorapidity range $|\eta| < 2.4$, with detection planes made using
²⁵² three technologies: drift tubes, cathode strip chambers, and resistive plate chambers. The single
²⁵³ muon trigger efficiency exceeds 90% over the full η range, and the efficiency to reconstruct and
²⁵⁴ identify muons is greater than 96%. Matching muons to tracks measured in the silicon tracker
²⁵⁵ results in a relative transverse momentum resolution, for muons with p_T up to 100 GeV, of 1% in
²⁵⁶ the barrel and 3% in the endcaps. The p_T resolution in the barrel is better than 7% for muons with
²⁵⁷ p_T up to 1 TeV [29].

²⁵⁸ A two-tiered trigger system [30]. The first level (L1), composed of custom hardware processors,
²⁵⁹ uses information from the calorimeters and muon detectors to select events at a rate of around
²⁶⁰ 100 kHz within a time interval of less than 4 μs . The second level, known as the high-level trigger
²⁶¹ (HLT), consists of a farm of processors running a version of the full event reconstruction software
²⁶² optimized for fast processing, and reduces the event rate to around 1 kHz before data storage.

²⁶³ A more detailed description of the CMS detector, together with a definition of the coordinate
²⁶⁴ system used and the relevant kinematic variables, can be found in Ref. [31].

265 falar do sistema de coordenadas e definir η

266 **3.1 Tracker**

267 FAZER!

268 **3.2 Electromagnetic Calorimeter**

269 FAZER!

270 **3.3 Hadronic Calorimeter**

271 FAZER!

272 **3.4 Muon System**

273 FAZER!

274 **3.4.1 DT**

275 FAZER!

276 **3.4.2 CSC**

277 FAZER!

278 **3.4.3 RPC**

279 FAZER!

280 **3.4.4 GEN**

281 FAZER!

282 **3.5 Trigger and Data Acquisition**

283 FAZER!

284 **3.6 Simulation, reconstruction and computing**

285 FAZER!

286 **3.7 Particle Flow Algorithim**

287 FAZER!

288 4 Physics Analysis

289 **DEFINIR A ANALISE**
290 **EXPLICAR O PROCESSO E EXEMPLOS DE GRAFICO**
291 **EXPLICAR A ESTRATEGIA**

292 4.1 Datasets and simulated events

293 4.1.1 Data samples

294 The data sample used in this analysis consists of the 2016 13 TeV run with 25 ns bunch separation
295 recorded by CMS. This data sample is composed only by events that were certified from all CMS
296 subsystems and reconstruction specialist as good for physics analysis.

297 This data sample corresponds to 35.86 fb^{-1} of integrated luminosity [32].

298 4.1.2 Simulated datasets

299 PILE-UP reweighting

300 A summary of the signal and background Monte Carlo (from here on, simply called MC) samples
301 used is presented in Table 4.1. These simulated data are comparable with the proton-proton collision
302 using 2016 data conditions and the pile-up events are added to the simulated event in this step. The
303 pile-up events distribution used is around 23 events, as recommended by CMS. Detector response in the
304 MC samples is simulated using a detailed description of the CMS detector, based on GEANT4 [33].

305 The signal MC samples are simulated for the Higgs bosons decaying to $\Upsilon(nS)(\rightarrow \mu\mu) + \gamma$ channels
306 with POWHEG v2.0 [34–36], at next-to-leading order (NLO) of Feynman graphs computation, for
307 the following production modes: gluon-gluon fusion (ggF), vector boson fusion (VBF), associated
308 production (VH) and associated top production (ttH), with cross-section summarized at table 4.1.
309 An extensive review of these production modes can be found at [37]. The PYTHIA 8 generator [38,
310 39] is used for hadronization and fragmentation with underlying event tune CUETP8M1 [40]. The
311 parton distribution functions (pdf) NNPDF3.0 [41] are used.

312 For Z decaying to $\Upsilon(nS)(\rightarrow \mu\mu) + \gamma$ channels, the signal samples are simulated with MAD-
313 GRAPH 5 _MC@NLO 2.6.0 matrix element generator [42] at next leading order and the PYTHIA 8
314 generator [38, 39] for hadronization and fragmentation with underlying event tune CUETP8M1 [40].

315 The Drell-Yan process, $pp \rightarrow Z \rightarrow \mu\mu\gamma$, results in the same final state as the signal. This
316 process exhibits a peak in the three-body invariant mass, $m_{\mu\mu\gamma}$, at the Z boson mass, m_Z , and it is
317 a resonant background for this channel, therefore referred to as a Peaking Background.

318 It is taken into account when deriving the upper limit on the branching fraction for $Z \rightarrow \Upsilon(nS) +$
319 $\gamma \rightarrow \mu\mu + \gamma$. The MADGRAPH 5 _MC@NLO 2.6.0 matrix element generator [42] at leading order,

320 interfaced with PYTHIA 8.226 for parton showering and hadronization with tune CUETP8M1 [40],
 321 is used to generate a sample of these resonant background events. The photons in these events are
 322 all produced as final-state radiation from the $Z \rightarrow \mu\mu$ decay and therefore the $m_{\mu\mu\gamma}$ distribution
 323 peaks at the Z boson mass and there is no continuum contribution.

324 Similarly, the Higgs boson Dalitz decay [43], $H \rightarrow \gamma^*\gamma \rightarrow \mu\mu + \gamma$, is a Peaking Background
 325 (resonant) to $H \rightarrow \Upsilon(nS) \rightarrow \mu\mu + \gamma$. It is simulated at NLO with MADGRAPH 5 _MC@NLO
 326 2.6.0 matrix element generator [42] at next-to-leading order and the PYTHIA 8 generator [38, 39] for
 327 hadronization and fragmentation with underlying event tune CUETP8M1 [40]. This Higgs Dalitz
 328 Decay sample, was generated only for the ggF production mode, but its cross-section was rescaled
 329 to the full Higgs cross-section. This process will present a small contribuition of selected events, so
 330 this approximation should be sufficient for the Higgs Peaking Background modeling.

331 There are also background processes that do not give resonance peaks in the three-body invariant
 332 mass spectrum. They are modeled from data, as it will be explained latter in more details.

Physics Processes	Branching Ratio (BR_{SM})	Effective σ (in pb)	Generator	Sample Type
$H \rightarrow \Upsilon(1S) + \gamma$	5.22×10^{-9}	7.14×10^{-9}	POWHEG 2.0	Signal
$H \rightarrow \Upsilon(2S) + \gamma$	1.42×10^{-9}	1.51×10^{-9}	POWHEG 2.0	Signal
$H \rightarrow \Upsilon(3S) + \gamma$	9.10×10^{-10}	1.10×10^{-9}	POWHEG 2.0	Signal
$Z \rightarrow \Upsilon(1S) + \gamma$	4.88×10^{-8}	6.80×10^{-5}	MADGRAPH 5	Signal
$Z \rightarrow \Upsilon(2S) + \gamma$	2.44×10^{-8}	2.69×10^{-5}	MADGRAPH 5	Signal
$Z \rightarrow \Upsilon(3S) + \gamma$	1.88×10^{-8}	2.34×10^{-5}	MADGRAPH 5	Signal
H Dalitz Decay	3.83×10^{-5}	2.13×10^{-3}	MADGRAPH 5	Peaking Background
$Z \rightarrow \mu\mu\gamma_{FSR}$	—	7.93×10^{-2}	MADGRAPH 5	Peaking Background

Table 4.1: Datasets simulated (MC) for 2016 conditions. Assuming that $\sigma(pp \rightarrow H)$, taking into consideration all the simulated Higgs production modes, is 55.13 pb [44] and $\sigma(pp \rightarrow Z \rightarrow \mu\mu)$ is 57094.5 pb , including the next-to-next-to-leading order (NNLO) QCD contributions, and the next-to-leading order (NLO) electroweak corrections from fewz 3.1 [45] calculated using the NLO PDF set NNPDF3.0, with the phase space selection in invariant mass of the dimuon system of $m_{\mu\mu} > 50 \text{ GeV}$. For the Higgs Dalitz σ , we consider only the gluon fusion contribution ($\sigma_{ggF} = 48.6 \text{ pb}$) [44]. The Higgs Dalitz Decay BR_{SM} and the $Z \rightarrow \mu\mu\gamma_{FSR}$ were obtained with MCFM 6.6 [46] (as in the CMS search for Higgs Dalitz Decay in at $\sqrt{s} = 8 \text{ TeV}$ [47]) and with MADGRAPH 5 _MC@NLO, respectively. The $BR_{\Upsilon(1S,2S,3S) \rightarrow \mu\mu}^{PDG} = (2.48, 1.93, 2.18) \times 10^{-2}$ is quoted from Particle Data Group report (PDG) [2]. The "Effective σ " for the signal samples is $\sigma(pp \rightarrow Z(H)) \times BR_{SM} \times BR_{\Upsilon(nS) \rightarrow \mu\mu}^{PDG}$.

333 The number of simulated events is is rescaled by the Effective σ , from table 4.1, in order to match
 334 35.86 fb^{-1} of integrated luminosity, from the recorded data. Being $N = \sigma\mathcal{L}$, N in the number of
 335 events for a process, σ is the cross-section and \mathcal{L} is the integrated luminosity, the reweighting factor,
 336 for a simulated sample is:

$$w_{MC} = \frac{\sigma\mathcal{L}}{N_{sim}}, \quad (4.1)$$

337 where N_{sim} is the number of simulated events for a specific process.

338 The simulated sample are also corrected by the data pile-up distribution, since the pileup dis-
 339 tribution of MC is different from the pileup distribution of data. The way to correct the MC is to

340 assign a weight to each bin of the MC pileup distribution, with respect to the data. The rescaling is
341 defined as the ratio between normalized Pile-up (PU) distribution for Data and MC.

$$w_{PU}(n) = \frac{P_{PU}^{Data}(n)}{P_{PU}^{Sim}(n)}, \quad (4.2)$$

342 where n is the number of interaction per bunch crossing (pile-up).

343 4.2 Contribution of the $\Upsilon(nS)$ polarisation

344 Measurements of quarkonium polarization observables may yield information about quarkonium
345 production mechanisms that are not available from the study of unpolarized cross sections alone.
346 The three polarization states of a $J = 1$ quarkonium can be specified in terms of a particular
347 coordinate system in the rest frame of the quarkonium. This coordinate system is often called the
348 "spin-quantization frame".

349 In a hadron collider, $\Upsilon(1S, 2S, 3S)$ are reconstructed through their electromagnetic decays into
350 a lepton pair. The information about the polarization of the quarkonium state is encoded in the
351 angular distribution of the leptons. This angular distribution is usually described in the quarko-
352 nium rest frame with respect to a particular spin-quantization frame [48]. The polarization of the
353 $\Upsilon(1S, 2S, 3S)$ is not simulated for signal MC sample and we only apply a reweighting scale factor to
354 each event and so we can emulate the polarization effects [49]. Figure 4.1 present the distributions
355 of $\cos \Theta$ of $\Upsilon \rightarrow \mu\mu$, where Θ is the angle between the positive muon and the Υ in the Z (Higgs)
356 rest-frame. At Table 4.2 we show the the analytical functions used to describe the extremes scenar-
357 ios (Unpolarized, Transverse Polarization and Longitudinal Polarization) reweighting, presented in
358 this analysis.

359 It is worth stating that, for the Higgs decay, on the Transverse Polarization is considered. For
360 the Z decay, because of its spin nature, the Unpolarized scenario is used as the nominal one, and
361 the effects of the two other extremes (Transverse Polarization and Longitudinal Polarization) are
362 quoted as systematics.

J_Z	Polarisation Scenario	Analytic Description
± 1	Transverse	$3/4 \times (1 + (\cos \Theta)^2)$
0	Longitudinal	$3/2 \times (1 - (\cos \Theta)^2)$

Table 4.2: Summary of the impact of reweighted of polarization contribution using several scenarios.

363 4.3 Kinematical studies using MC generator

364 Using the PYTHIA 8.226 generator, the Monte Carlo signals are produced for Higgs (Z) boson
365 events decaying in $(\Upsilon(1S, 2S, 3S)) + \gamma$, which are highly boosted. Observing the kinematic generator
366 level distributions in Figure 4.2 for Z boson and Figure 4.3 for Higgs boson, we could conclude that
367 the high- E_T (transverse energy, with respect to the beam line) photon will be back-to-back to the Υ
368 particles being possible to apply an isolation selection to identify a photon in this kinematic topology.

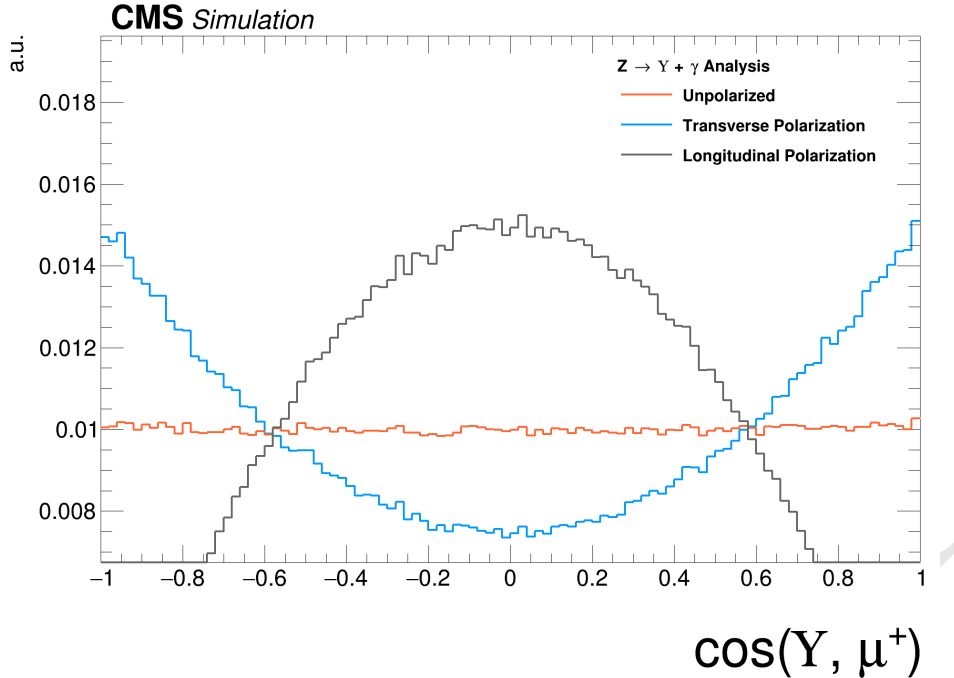


Figure 4.1: Distributions of $\cos\theta$ of $\Upsilon \rightarrow \mu\mu$ and $\gamma^* \rightarrow \mu\mu$. The orange distribution is the $Z \rightarrow \Upsilon(1S, 2S, 3S) + \gamma$ sample before reweighting (Unpolarized); the blue and gray distributions are $Z \rightarrow \Upsilon(1S, 2S, 3S)$ sample after reweighting, for the Transverse and Longitudinal Polarization.

369 Also, we can observe those transverse momenta of the leading/trailing p_T (transverse momemtum,
 370 with respect to the beam line) muon¹ and the photon and distances $\Delta R = \sqrt{\Delta\eta^2 + \Delta\phi^2}$ between
 371 the two muons and between the muons and the photon are a good variable that can be used to
 372 discriminate the contribution between signal and background events. The leading muon transverse
 373 momentum can be greater than 45(30) GeV and trailing muon is greater than 10(20) GeV in Higgs(Z)
 374 decay. ΔR distributions of the two muons and between the muons and the photon in the both cases
 375 show that the two muons are very close and the photon is back-to-back in relation of dimuon system.
 376 Another feature of this kinematic topology is that the production vertex between muons produced
 377 in Υ decaying events and the high- E_T photon is very well defined.

¹In this study we define leading muon and the muon, decaying from the Υ , with highest p_T . Trailing muon is the one with the second hight p_T .

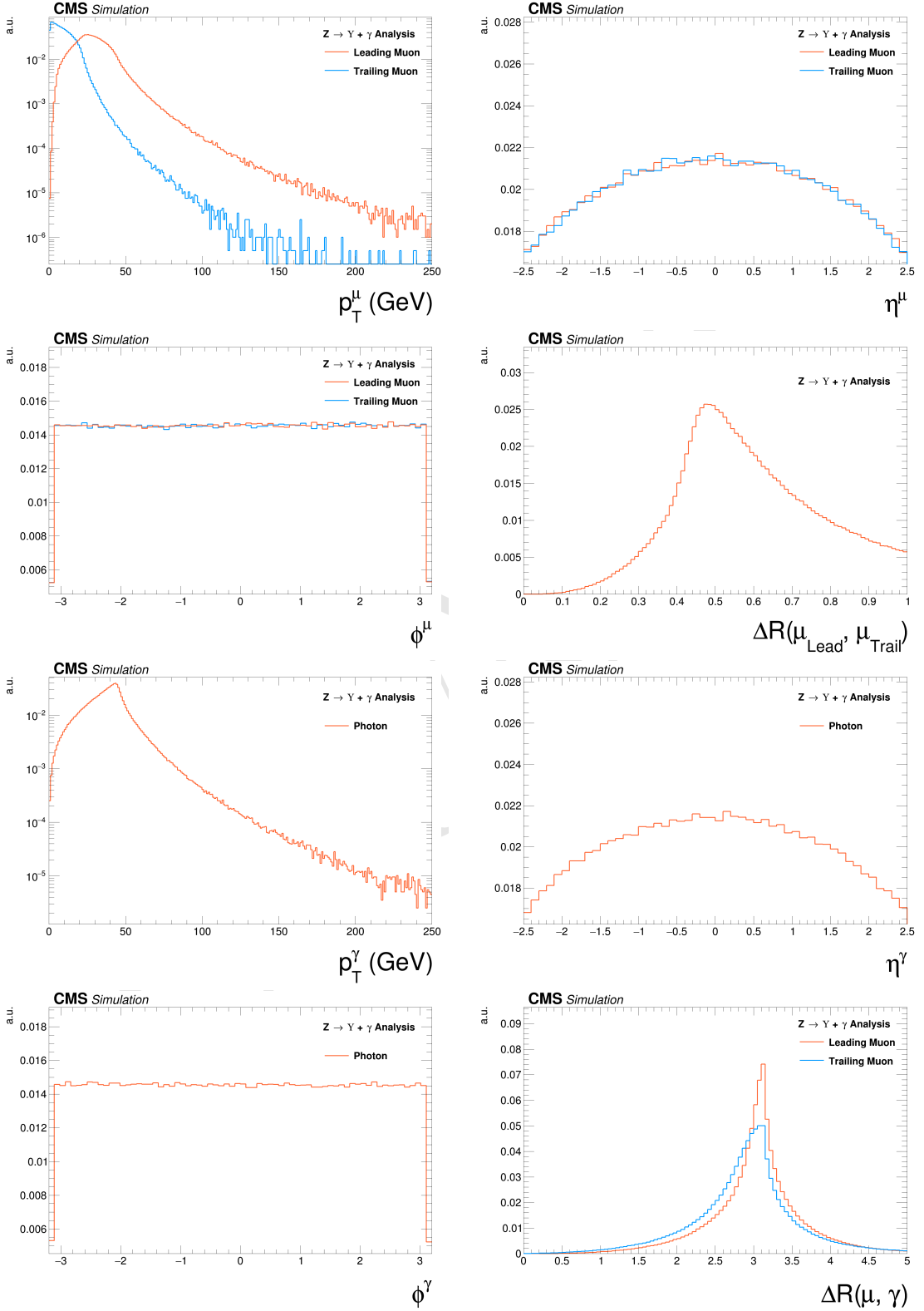


Figure 4.2: Generator level distributions of main variables for $Z \rightarrow \Upsilon(1S, 2S, 3S) + \gamma$: Transverse momenta of the leading/trailing p_T muon and the photon, pseudorapidity (η) and ϕ of the muons and the photon, distances ΔR between the two muons and between the muons and the photon. All the distributions shown in the figure are normalized to the unity of area.

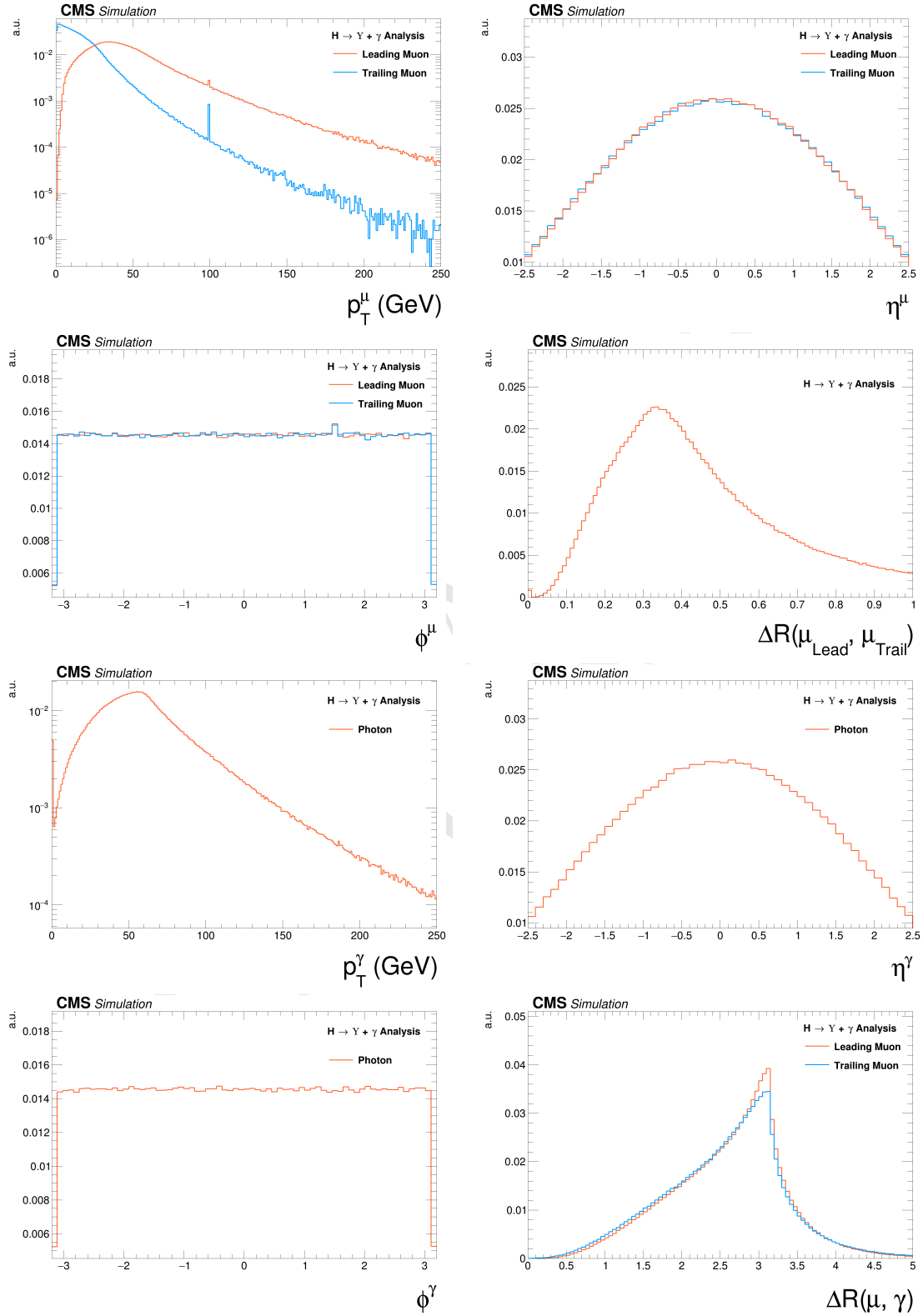


Figure 4.3: Generator level distributions of main variables for $H \rightarrow \Upsilon(1S, 2S, 3S) + \gamma$: Transverse momenta of the leading/trailing p_T muon and the photon, pseudorapidity (η) and ϕ of the muons and the photon, distances ΔR between the two muons and between the muons and the photon. All the distributions shown in the figure are normalized to the unity of area.

378 4.4 Event selection

379 The event selection is divided in two steps. At first, a set of cuts related to trigger and physics
 380 object (muons and photons) selection is applied. High level physics objects at CMS are reconstructed
 381 based of the Particle Flow (PF) algorithm [50]. This selection is called, within this analysis, Group
 382 I.

383 For the events that pass the Group I selection, another set of cuts is applied, this time focusing
 384 on kinematical (phase space) event selection, in order to enhance the signal to background ratio.
 385 This later set is called, within this analysis, Group II. After full selection, three exclusive categories
 386 are defined, based on the photon's η region and its energy spread shape within the ECAL cells (R9).

387 After the full selection, a background and signal modeling process is applied, based on the
 388 invariant mass distributions, which will be explained in the next section.

389 4.5 Trigger and physics object selection (Group I)

390 4.5.1 Trigger

391 In this study, the same trigger requirements are applied to both data and simulated samples.
 392 For the first trigger level (L1), events are selected if they present at least one muon with transverse
 393 momentum greater than 5 GeV and an isolated ² photon or electron with transverse momentum
 394 greater than 18 GeV (at L1, there is no differentiation between photons and electrons). At the
 395 software level of the trigger system (HLT), the events are required to have at least one muon with
 396 transverse momentum greater than 17 GeV and a photon with transverse momentum greater than
 397 30 GeV.

398 In order to compensate any difference in the trigger performance between simulated and data
 399 samples, for every selected MC a proper scale factor is applied, based on the the p_T of the recon-
 400 structed muon and photon. Considering the similarity of this analysis with the $H/Z \rightarrow J/\psi + \gamma$
 401 analysis [23], not only in therm of data samples, but also for triggering and physics object selection,
 402 the same scale factors were applied.

403 4.5.2 Muon Identification

404 Ahead of any selection, a standard CMS "Ghost Cleaning" procedure is applied to all recon-
 405 structed muons in order to avoid that a single physical muon is reconstructed as two or more. For
 406 this procedure, reconstructed muons sharing 50% or more segments in the system are arbitrated.

407 After the cleaning, a muon is chosen when it passes a a two step identification: the **Loose ID**
 408 and the **Tight ID**. Below the muon identification procedure is summarized .

409 For the Loose ID, each muon is required to:

- 410 • have transverse momentum greater than 5 GeV, in order to cope with Particle Flow require-
 411 ments;

²The concept of isolation will be detailed later, but in summary, it means a object which has very small activity (above a certain threshold of energy/momentum) around it. In hadron-hadron collider, isolation is a characteristics of hard interactions.

- be within the muon system acceptance: $|\eta| < 2.4$;
- to have a three dimensional impact parameter uncertainty smaller than 4;
- to have transverse distance smaller than 0.5 cm ($d_{xy} < 0.5$), with respect to the primary vertex (PV);
- to have longitudinal distance greater than 1.0 cm ($d_z < 1$), with respect to the primary vertex (PV).

Muons reconstructed only in the muon system, without a correspondence with the tracker, are rejected. The last three requirements of the Loose ID are imposed in order to suppress muons from in-flight decays.

The primary vertex itself, is determined as the reconstructed vertex with the biggest sum of p_T^2 in the event. This sum is performed, considering all the charged PF candidates clustered by the jet finding algorithms [51, 52] and the MET, which is defined as the p_T vector sum of all the charged and neutral PF candidates associated to that vertex.

For the Tight ID, muons with transverse momentum $p_T < 200$ GeV, are required to have been reconstructed with the Particle Flow (PF) algorithm. If they have $p_T > 200$ GeV, they should be reconstructed with the Particle Flow (PF) algorithm or satisfy the strict tracker requirements (defined in table 4.3).

Requirement	Technical definition
Muon station matching	Muon is matched to segments in at least two stations in the muon system
Good p_T measurement	$\frac{p_T}{\sigma_{p_T}} < 0.3$
Vertex compatibility ($x - y$)	$d_{xy} < 2$ mm
Vertex compatibility (z)	$d_z < 5$ mm
Pixel hits	At least one pixel hit
Tracker hits	Hits in at least six tracker layers

Table 4.3: Conditions for a muon to pass the strict tracker requirements.

To mitigate spurious signal in the detector that would mimic a muon, the leading muon (the one with highest p_T) is required to be isolated within a cone of radius $\Delta R = \sqrt{\Delta\eta^2 + \Delta\phi^2} < 0.3$ in the $\eta - \phi$ plane. The isolation is evaluated in terms of $\mathcal{I}^\mu < 0.35$, defined as:

$$\mathcal{I}^\mu \equiv \left(\sum p_T^{\text{charged}} + \max \left[0, \sum p_T^{\text{neutral}} + \sum p_T^\gamma - p_T^{\text{PU}}(\mu) \right] \right) / p_T^\mu. \quad (4.3)$$

The $\sum p_T^{\text{charged}}$ is the scalar sum of the transverse momenta of charged hadrons originating from the chosen primary vertex of the event. The $\sum p_T^{\text{neutral}}$ and $\sum p_T^\gamma$ are the scalar sums of the transverse momenta for neutral hadrons and photons, respectively. Since the isolation variable is particularly sensitive to energy deposits from pileup interactions, a $p_T^{\text{PU}}(\mu)$ contribution is subtracted, where $p_T^{\text{PU}}(\mu) \equiv 0.5 \times \sum_i p_T^{\text{PU},i}$, where i runs over the momenta of the charged hadron PF candidates not originating from the primary vertex, and the factor of 0.5 corrects for the different fraction of charged and neutral particles in the cone.

439 One should keep in mind that this muon identification is the same as the one used by the
 440 $H \rightarrow ZZ^* \rightarrow 4l$ [53]. This was done in order to keep in phase with other Higgs analysis inside
 441 the collaboration. After the muon identification, an appropriate scale factor is applied to the MC
 442 events based on the leading muon p_T and η , in order to correct any possible discrepancy between
 443 data and simulated samples. The scale factors were taken from the $H \rightarrow ZZ^* \rightarrow 4l$ analysis.

444 In order to cope with trigger requirements, the leading muon should have $p_T > 20$ GeV and the
 445 trailing muon $p_T > 4$ GeV.

446 4.5.3 Photon Identification

447 For the photon identification and selection, standard CMS . The Multivariate (MVA) Photon
 448 identification is used with a working point of 90%, together with a electron veto procedure, to
 449 avoid misidentification of electrons as photons. Kinematically, the photons are requested to have
 450 transverse energy, with respect to the beam line, $E_T > 33$ GeV and reconstructed within the CMS
 451 acceptance for photons $|\eta_{SC}| < 2.5$ ³, excluding the Electromagnetic Calorimeter (ECAL) Barrel-
 452 Endcap intersections.

453 The threshold of 33 GeV for the photon transverse energy is driven by the trigger requirements.

454 The selecte photon, per event, is the one with highest E_T .

455 4.5.4 Kinematical distributions

456 The selection described so far, is called Group I. The plots shown below are related to selected
 457 events after this set.

458 Figures 4.4 to 4.9 presents the p_T , η and ϕ distributions for the leading muon, trailing muon
 459 and the photon, for the Z decaying in $\Upsilon(1S, 2S, 3S) + \gamma$.

460 Figures 4.10 to 4.12 presents the p_T , η and ϕ distributions for reconstructed $\Upsilon(nS)$ ($\mu\mu$ system)
 461 and the reconstructed boson ($\mu\mu\gamma$ system).

462 Figures 4.13 to 4.16 presents the $\Delta R = \sqrt{\Delta\eta^2 + \Delta\phi^2}$ between the photon and the muons, the
 463 ΔR distributions between reconstructed dimuon ($\mu\mu$) system and the photon, the absolute value
 464 of the $\Delta\phi$ between the leading muon and the photon, the ratio for the transverse momentum of
 465 the reconstructed Upsilon and the reconstructed Z mass ($p_T^{\mu\mu}/M_{\mu\mu\gamma}$), the ratio for the transverse
 466 energy of the reconstructed Photon and the reconstructed Z mass ($E_T^{\mu\mu}/M_{\mu\mu\gamma}$) and dimuon mass
 467 distribution of the reconstructed $\Upsilon(nS)$.

468 Figures 4.17 to 4.29 present the same variables, but for the Higgs decaying in $\Upsilon(1S, 2S, 3S) +$
 469 γ channel.

³SC stands for Super Cluster of the reconstructed photon. It is the set of cell in the Electromagnetic Calorimeter used for the photon observation.

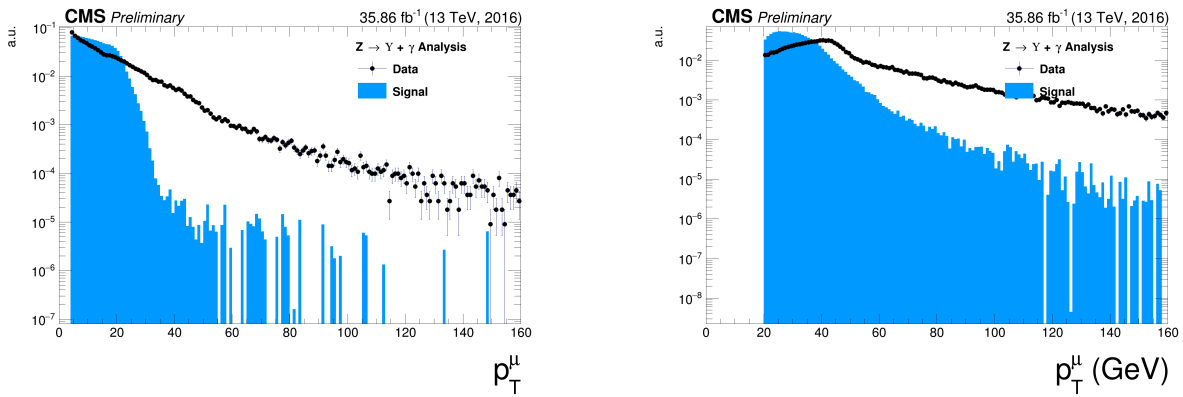


Figure 4.4: The p_T muon distributions from data and signal events for Z decaying in $\Upsilon(1S, 2S, 3S) + \gamma$ after Group I of selection cuts, where on left are presenting the trailing muons and on right are the leading muons. The plots are normalized to the unit of area.

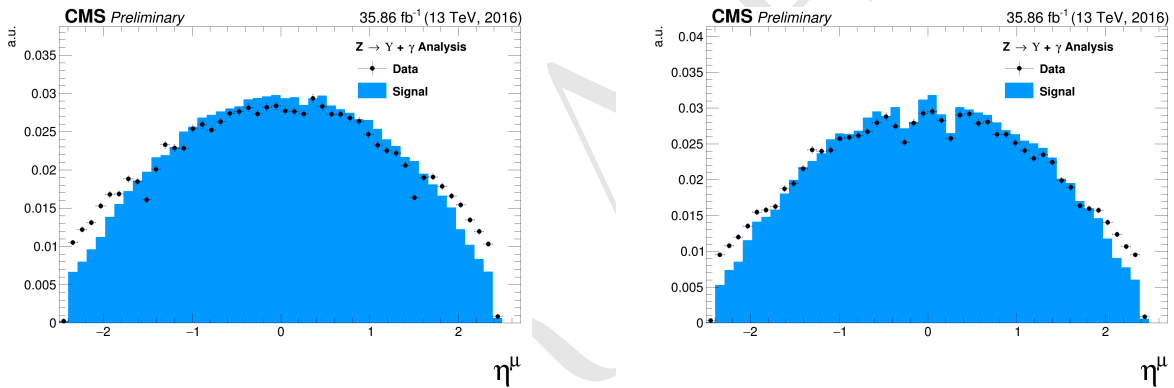


Figure 4.5: The η muon distributions from data and signal events of Z decaying in $\Upsilon(1S, 2S, 3S) + \gamma$ after Group I of selection cuts, where on left are presenting the trailing muons and on right are the leading muons. The plots are normalized to the unit of area.

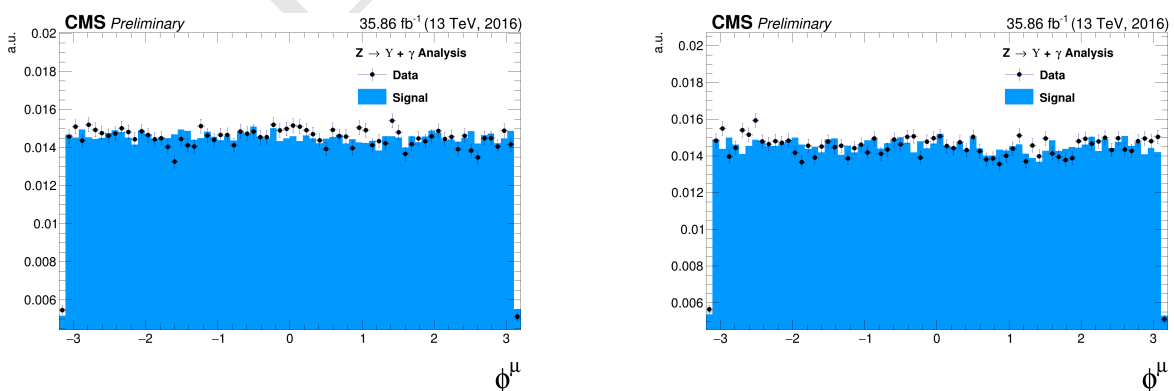


Figure 4.6: The ϕ muon distributions from data and signal events of Z decaying in $\Upsilon(1S, 2S, 3S) + \gamma$ after Group I of selection cuts, where on left are presenting the trailing muons and on right are the leading muons. The plots are normalized to the unit of area.

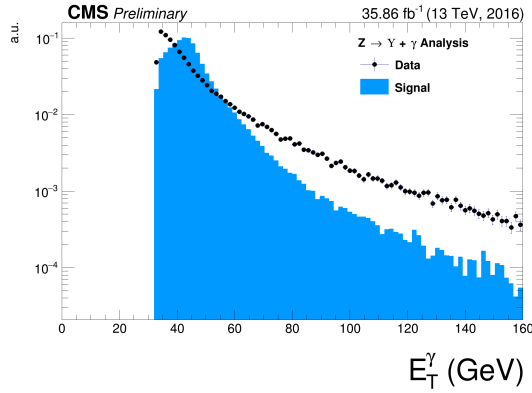


Figure 4.7: The p_T photon distributions from data and signal events for Z decaying in $\Upsilon(1S, 2S, 3S) + \gamma$ Group I of selection cuts. The plot is normalized to the unit of area.

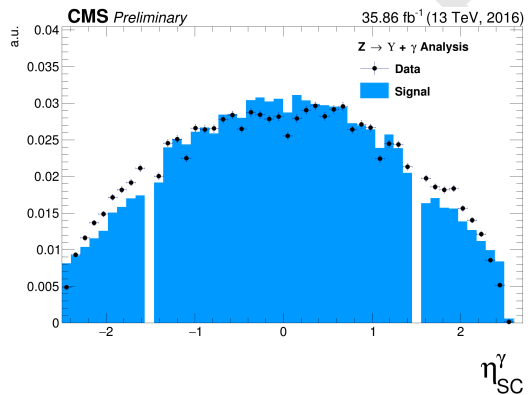


Figure 4.8: The η photon distributions from data and signal events of Z decaying in $\Upsilon(1S, 2S, 3S) + \gamma$ after Group I of selection cuts. The plot is normalized to the unit of area.

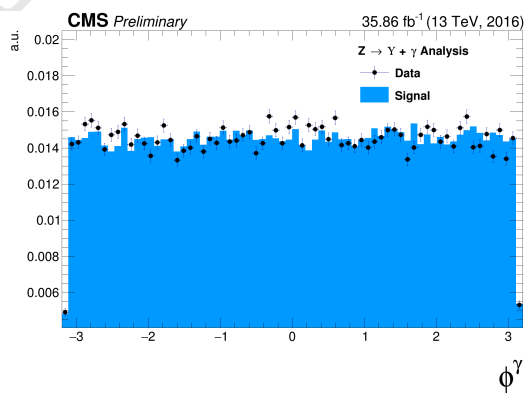


Figure 4.9: The ϕ photon distributions from data and signal events of Z decaying in $\Upsilon(1S, 2S, 3S) + \gamma$ after Group I of selection cuts. The plot is normalized to the unit of area.

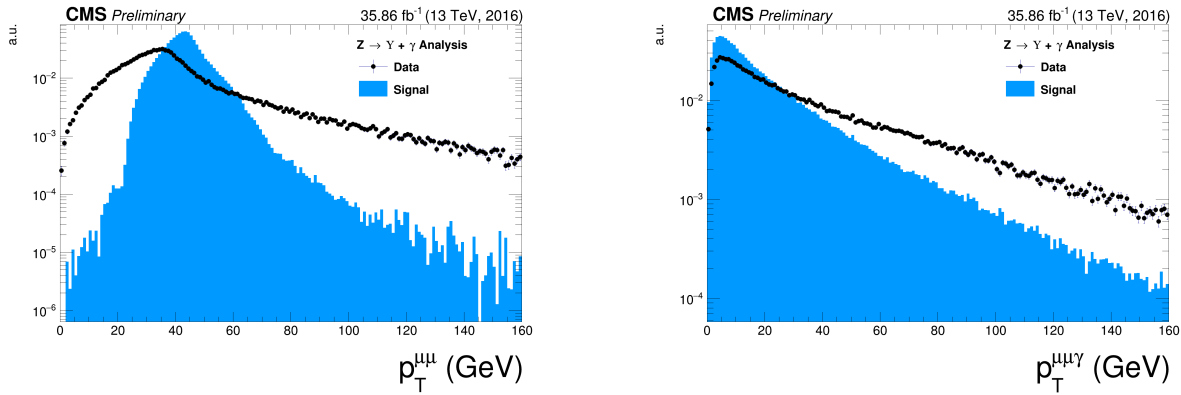


Figure 4.10: The p_T distributions for the reconstructed $\Upsilon(1S, 2S, 3S)$ in the left and for Z in the right from data and signal events for Z decaying in $\Upsilon(1S, 2S, 3S) + \gamma$ after Group I of selection cuts. The plots are normalized to the unit of area.

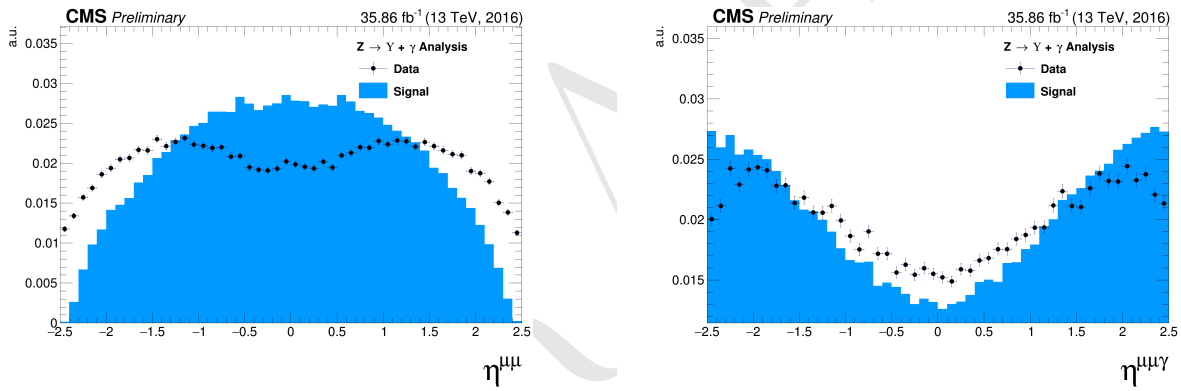


Figure 4.11: The η distributions for $\Upsilon(1S, 2S, 3S)$ in the left and for Z in the right from data and signal events for Z decaying in $\Upsilon(1S, 2S, 3S) + \gamma$ after Group I of selection cuts. The plots are normalized to the unit of area.

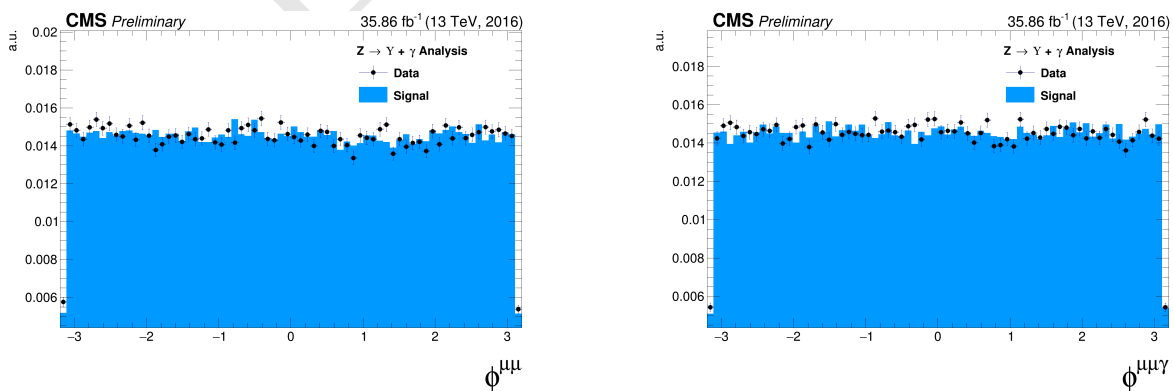


Figure 4.12: The ϕ distributions for $\Upsilon(1S, 2S, 3S)$ in the left and for Z in the right from data and signal events for Z decaying in $\Upsilon(1S, 2S, 3S) + \gamma$ after Group I of selection cuts. The plots are normalized to the unit of area.

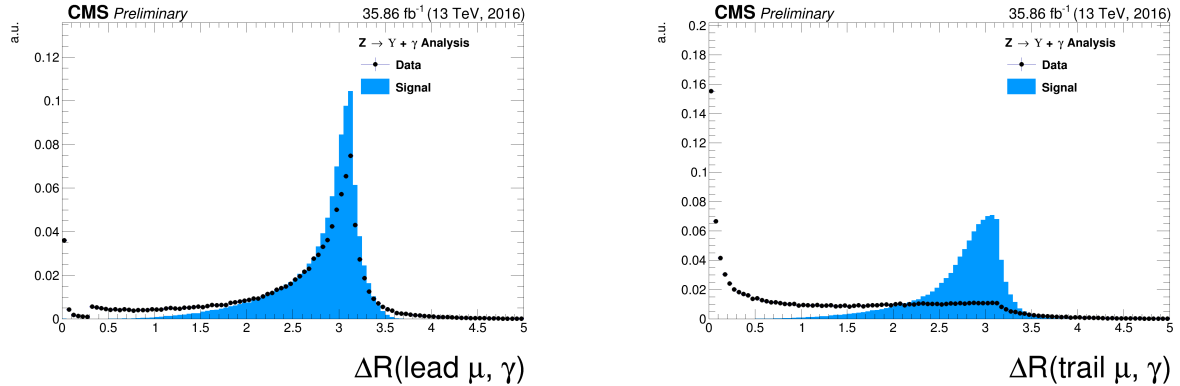


Figure 4.13: The ΔR distributions between the photon and the leading muon (left) and the trailing muon (right) for for Z decaying in $\Upsilon(1S, 2S, 3S) + \gamma$ from data and signal events after Group I of selection cuts. The plots are normalized to the unit of area.

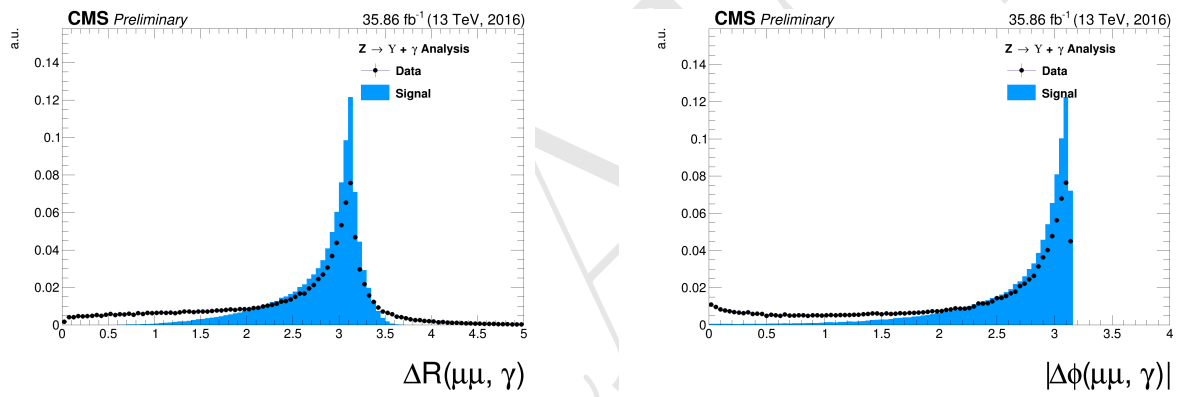


Figure 4.14: Left: The ΔR distributions between reconstructed dimuon ($\mu\mu$) system and the photon. Right: absolute value of the $\Delta\phi$ between the leading muon and the photon for for Z decaying in $\Upsilon(1S, 2S, 3S) + \gamma$ from data and signal events after Group I of selection cuts. The plots are normalized to the unit of area.

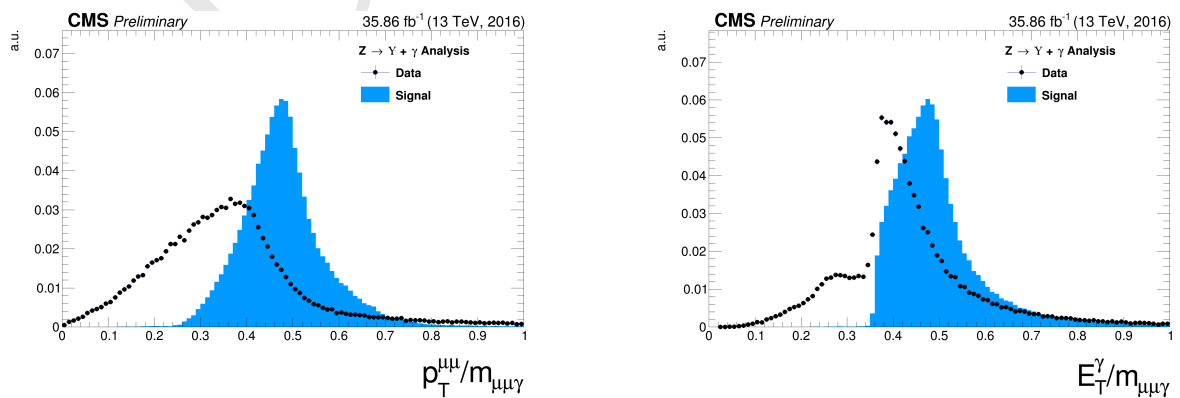


Figure 4.15: The ratio for the transverse momentum of the reconstructed Upsilon and the reconstructed Z mass ($p_T^{\mu\mu}/M_{\mu\mu\gamma}$ - left) and the ratio for the transverse energy of the reconstructed Photon and the reconstructed Z mass ($E_T^\gamma/M_{\mu\mu\gamma}$ - right) distribution for Z decaying in $\Upsilon(1S, 2S, 3S) + \gamma$ from data and signal events after Group I of selection cuts. The plots are normalized to the unit of area.

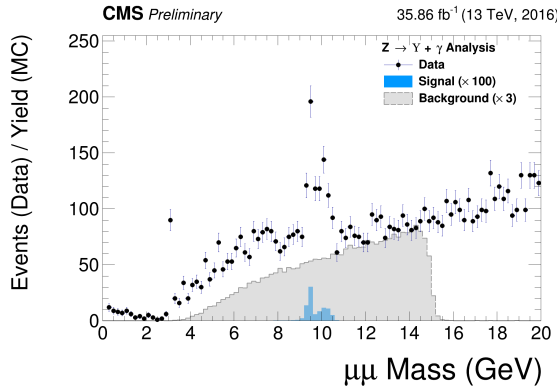


Figure 4.16: The dimuon mass distribution of the reconstructed $\Upsilon(1S, 2S, 3S)$ from data and signal events for Z decaying after Group I of selection cuts. The plot is normalized to the number of events. "Signal" stands for the $Z \rightarrow \Upsilon(1S, 2S, 3S) + \gamma$ sample (scaled by a factor of $\times 100$) and "Background" corresponds to the peaking background ($Z \rightarrow \mu\mu\gamma_{FSR}$) sample (scaled by a factor of $\times 3$).

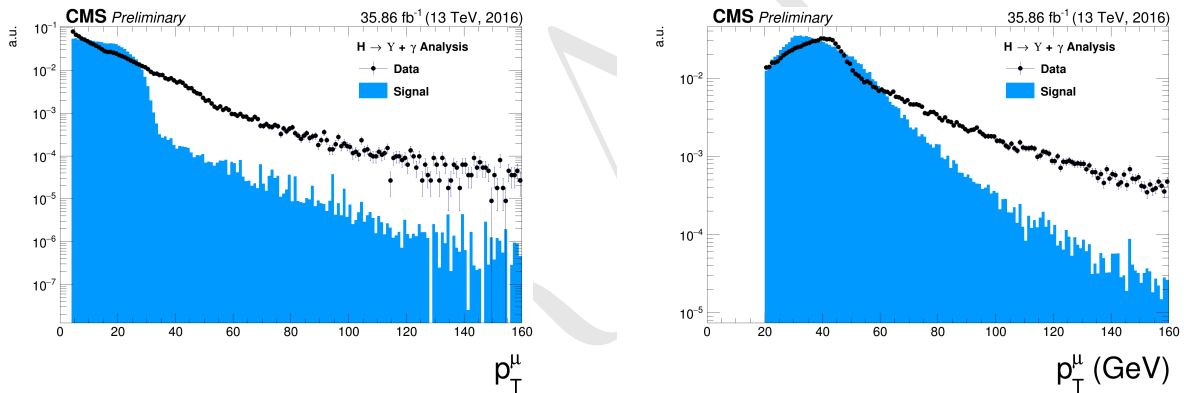


Figure 4.17: The p_T muon distributions from data and signal events for Higgs decaying in $\Upsilon(1S, 2S, 3S) + \gamma$ after Group I of selection cuts, where on left are presenting the trailing muons and on right are the leading muons. The plots are normalized to the unit of area.

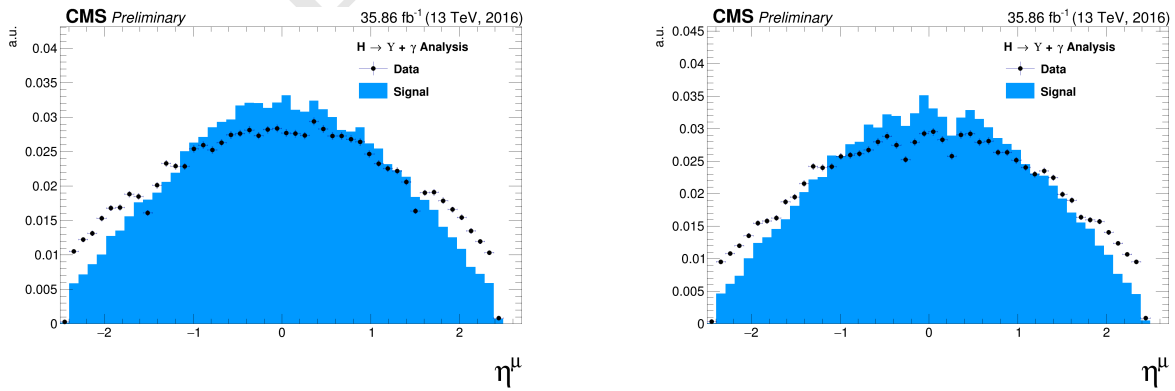


Figure 4.18: The η muon distributions from data and signal events of Higgs decaying in $\Upsilon(1S, 2S, 3S) + \gamma$ after Group I of selection cuts, where on left are presenting the trailing muons and on right are the leading muons. The plots are normalized to the unit of area.

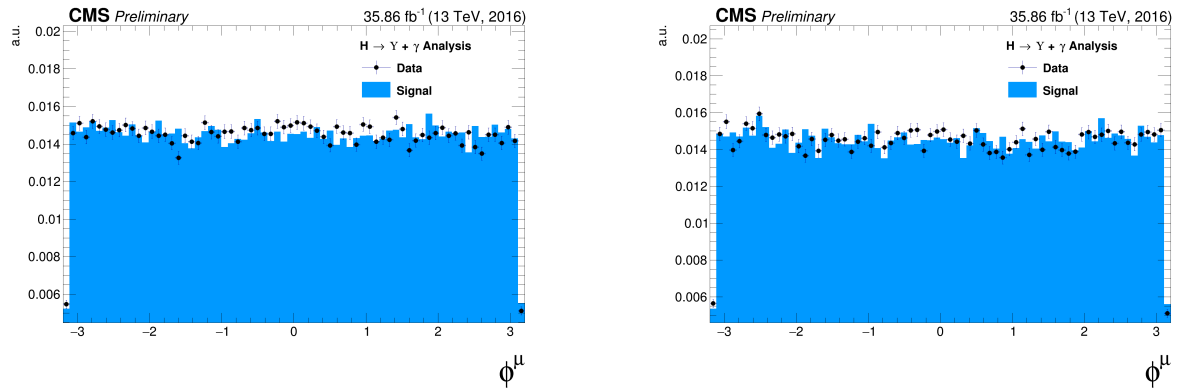


Figure 4.19: The ϕ muon distributions from data and signal events of Higgs decaying in $\Upsilon(1S, 2S, 3S) + \gamma$ after Group I of selection cuts, where on left are presenting the trailing muons and on right are the leading muons. The plots are normalized to the unit of area.

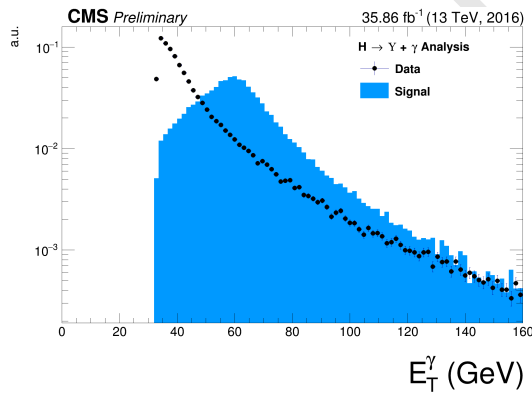


Figure 4.20: The p_T photon distributions from data and signal events for Higgs decaying in $\Upsilon(1S, 2S, 3S) + \gamma$ Group I of selection cuts. The plot is normalized to the unit of area.

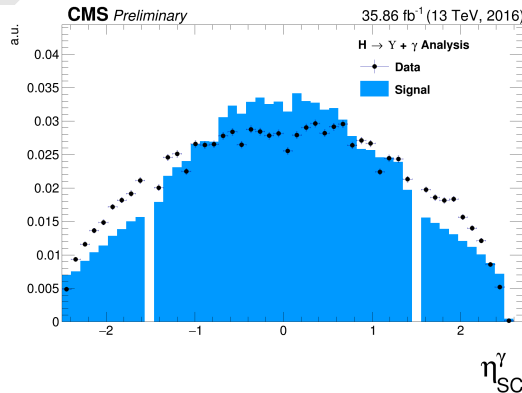


Figure 4.21: The η photon distributions from data and signal events of Higgs decaying in $\Upsilon(1S, 2S, 3S) + \gamma$ after Group I of selection cuts. The plot is normalized to the unit of area.

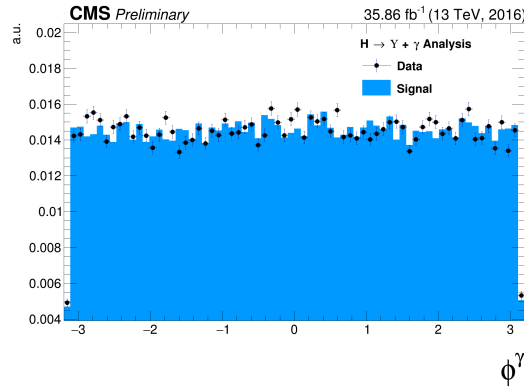


Figure 4.22: The ϕ photon distributions from data and signal events of Higgs decaying in $\Upsilon(1S, 2S, 3S) + \gamma$ after Group I of selection cuts. The plot is normalized to the unit of area.

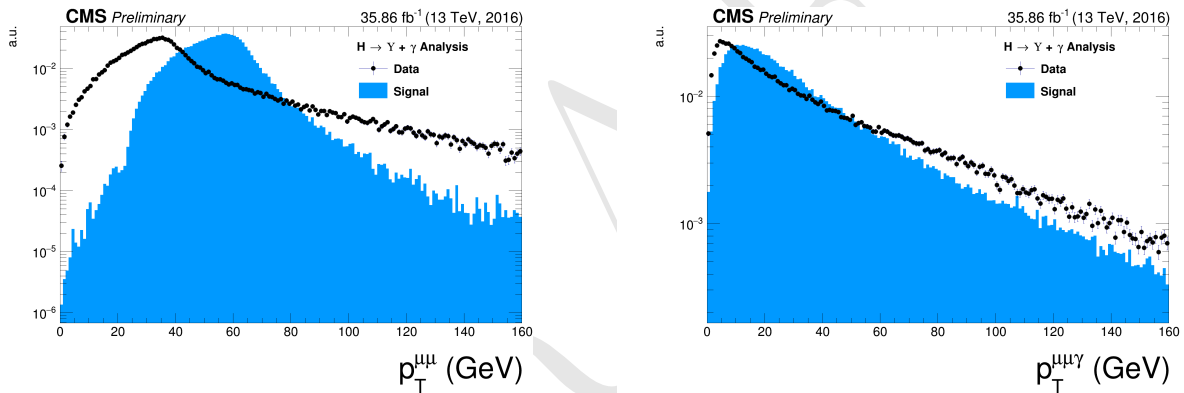


Figure 4.23: The p_T distributions for $\Upsilon(1S, 2S, 3S)$ in the left and for Higgs in the right from data and signal events for Higgs decaying in $\Upsilon(1S, 2S, 3S) + \gamma$ after Group I of selection cuts. The plots are normalized to the unit of area.

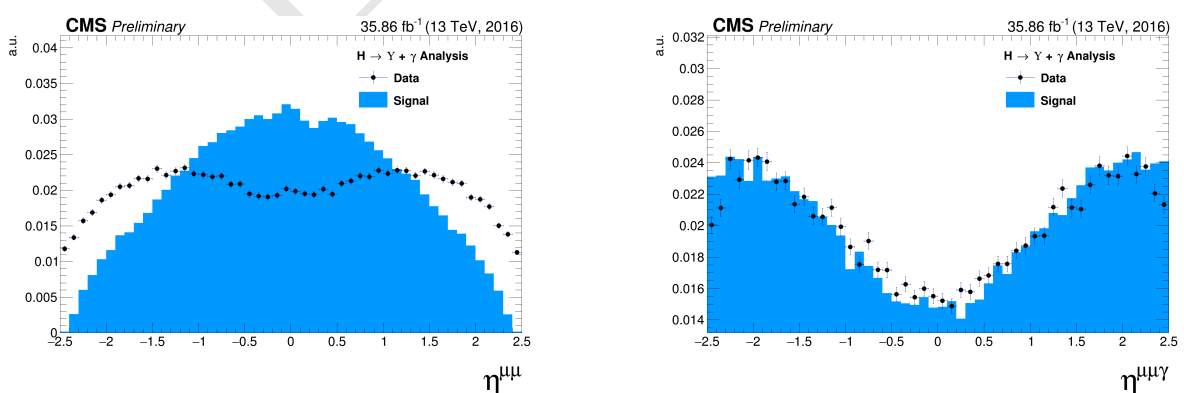


Figure 4.24: The η distributions for $\Upsilon(1S, 2S, 3S)$ in the left and for Higgs in the right from data and signal events for Higgs decaying in $\Upsilon(1S, 2S, 3S) + \gamma$ after Group I of selection cuts. The plots are normalized to the unit of area.

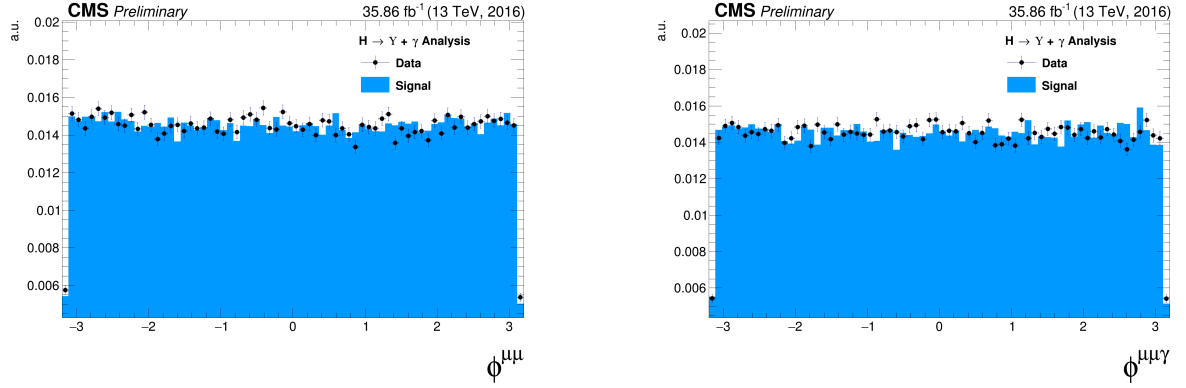


Figure 4.25: The ϕ distributions for $\Upsilon(1S, 2S, 3S)$ in the left and for Higgs in the right from data and signal events for Higgs decaying in $\Upsilon(1S, 2S, 3S) + \gamma$ after Group I of selection cuts. The plots are normalized to the unit of area.

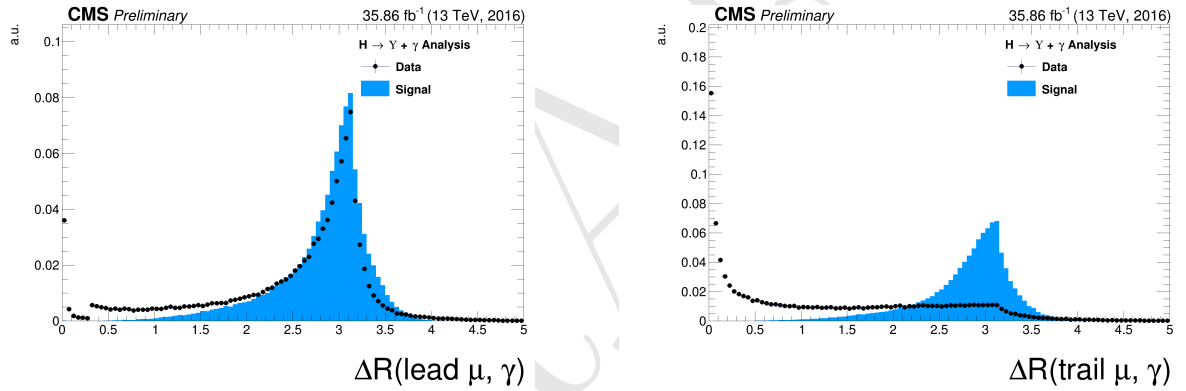


Figure 4.26: The ΔR distributions between the photon and the leading muon (left) and the trailing muon (right) for Higgs decaying in $\Upsilon(1S, 2S, 3S) + \gamma$ from data and signal events after Group I of selection cuts. The plots are normalized to the unit of area.

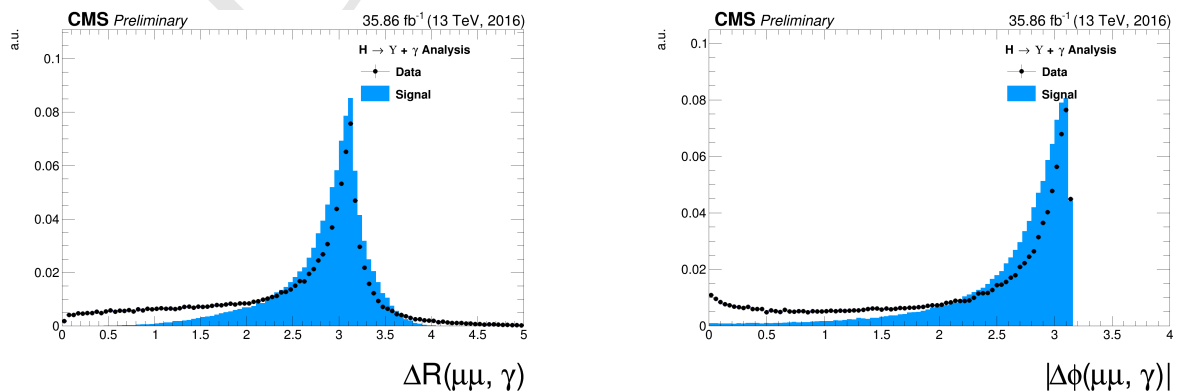


Figure 4.27: Left: The ΔR distributions between reconstructed dimuon ($\mu\mu$) system and the photon. Right: absolute value of the $\Delta\phi$ between the leading muon and the photon for Higgs decaying in $\Upsilon(1S, 2S, 3S) + \gamma$ from data and signal events after Group I of selection cuts. The plots are normalized to the unit of area.

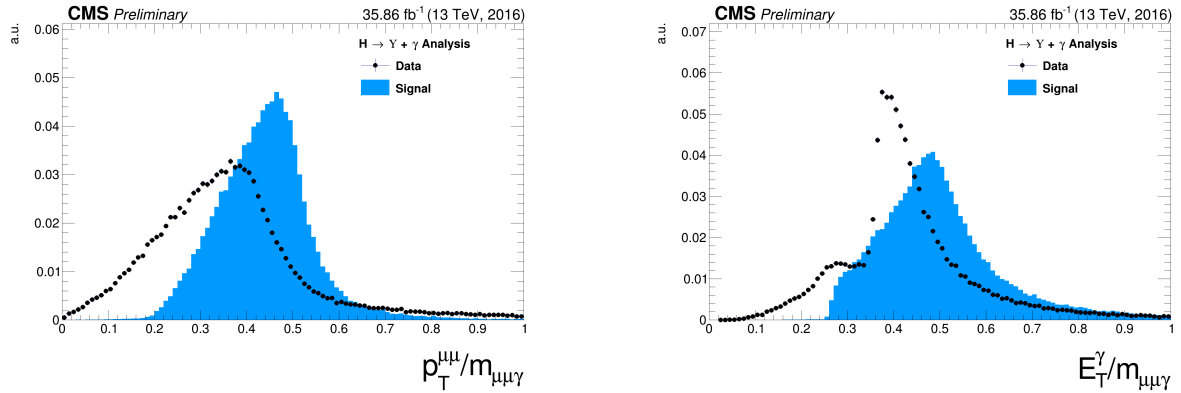


Figure 4.28: The ratio for the transverse momentum of the reconstructed Upsilon and the reconstructed Higgs mass ($p_T^{\mu\mu}/M_{\mu\mu\gamma}$ - left) and the ratio for the transverse energy of the reconstructed Photon and the reconstructed Higgs mass ($E_T^\gamma/M_{\mu\mu\gamma}$ - right) distribution for Higgs decaying in $\Upsilon(1S, 2S, 3S) + \gamma$ from data and signal events after Group I of selection cuts. The plots are normalized to the unit of area.

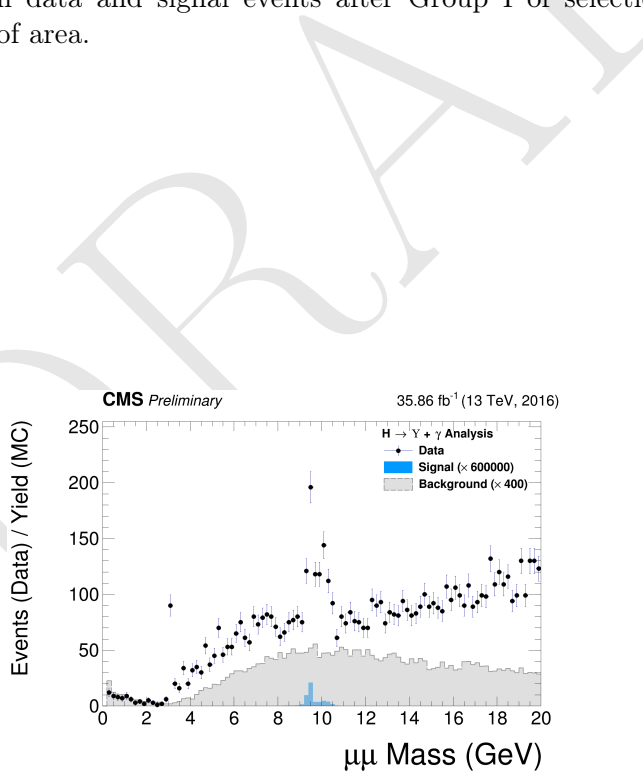


Figure 4.29: The dimuon mass distribution of the reconstructed $\Upsilon(1S, 2S, 3S)$ from data and signal events for Higgs decaying after Group I of selection cuts. This plot is normalized the expected number of events. The plot is normalized to the number of events. "Signal" stands for the $H \rightarrow \Upsilon(1S, 2S, 3S) + \gamma$ sample (scaled by a factor of $\times 600000$) and "Background" corresponds to the peaking background (Higgs Dalitz Decay) sample (scaled by a factor of $\times 400$).

4.6 Kinematical selection (Group II)

After all Trigger and Object Identification cuts, described in before (**Group I**), a set of kinematical cuts are applied in order to improve the signal to background relation. They are

- $\Delta R(\text{leading } \mu, \gamma) > 1;$
- $\Delta R(\text{trailing } \mu, \gamma) > 1;$
- $\Delta R(\mu\mu, \gamma) > 2;$
- $|\Delta\phi(\text{leading } \mu, \gamma)| > 1.5;$
- $8.4 \text{ GeV} < M_{\mu\mu} < 11.1 \text{ GeV};$
- $E_T^\gamma/M_{\mu\mu\gamma} > 35/91.2 \text{ for the Z decay or } 35/125 \text{ for the Higgs decay};$
- $p_T^{\mu\mu}/M_{\mu\mu\gamma} > 35/91.2 \text{ for the Z decay or } 35/125 \text{ for the Higgs decay}.$

The choice of these thresholds were based on the visual inspection of the distributions (besides the invariant mass distribution of the dimuon system $M_{\mu\mu}$, which needs to be defined around the $v(1S, 2S, 3S)$ mass) and to keep this analysis in phase with other similar analysis within CMS.

Below it is shown the same set of plot shown before, but this time, taking into account the full selection (**Group I+II**).

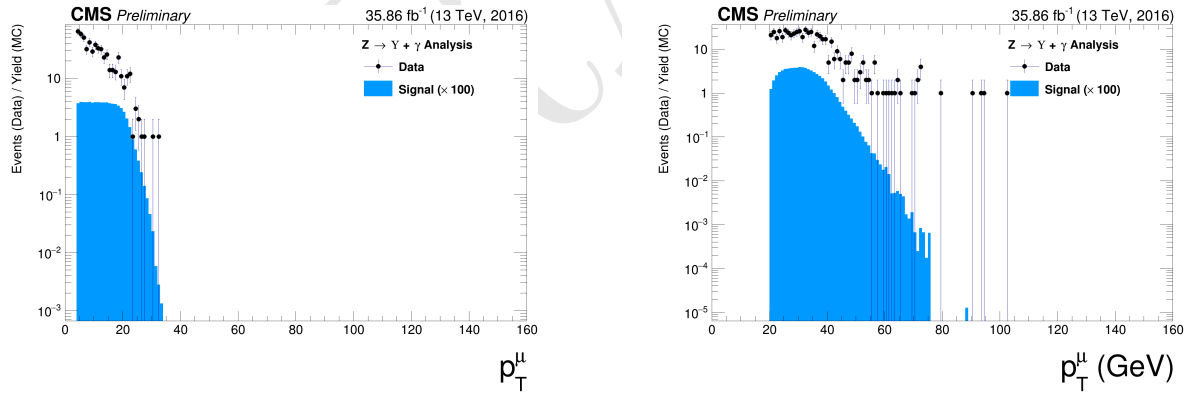


Figure 4.30: The p_T muon distributions from data and signal events for Z decaying in $\Upsilon(1S, 2S, 3S) + \gamma$ after Group I of selection cuts, where on left are presenting the trailing muons and on right are the leading muons. The plots are normalized to the number of events. Signal sample is scaled by a factor of $\times 100$.

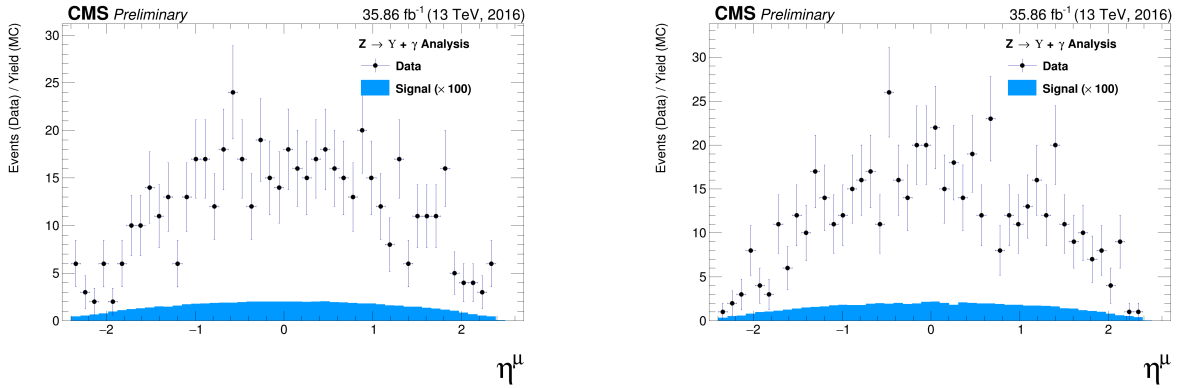


Figure 4.31: The η muon distributions from data and signal events of Z decaying in $\Upsilon(1S, 2S, 3S) + \gamma$ after Group I of selection cuts, where on left are presenting the trailing muons and on right are the leading muons. The plots are normalized to the number of events. Signal sample is scaled by a factor of $\times 100$.

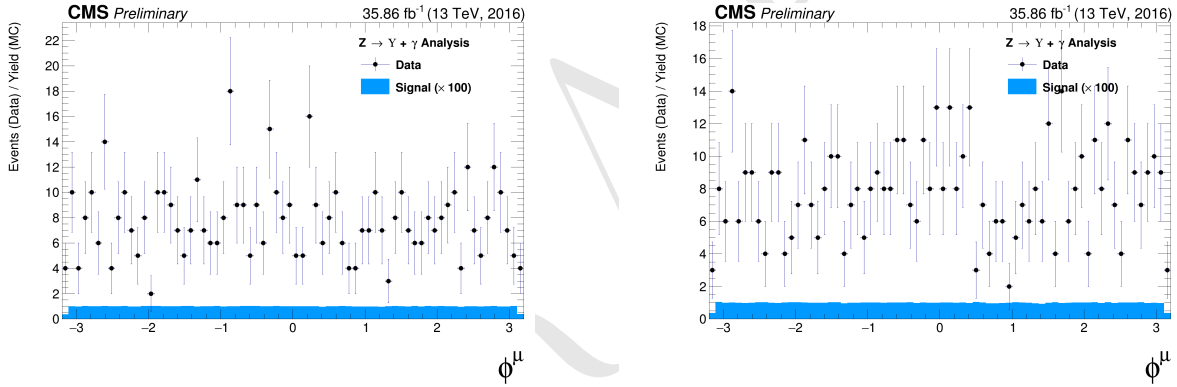


Figure 4.32: The ϕ muon distributions from data and signal events of Z decaying in $\Upsilon(1S, 2S, 3S) + \gamma$ after Group I of selection cuts, where on left are presenting the trailing muons and on right are the leading muons. The plots are normalized to the number of events. Signal sample is scaled by a factor of $\times 100$.

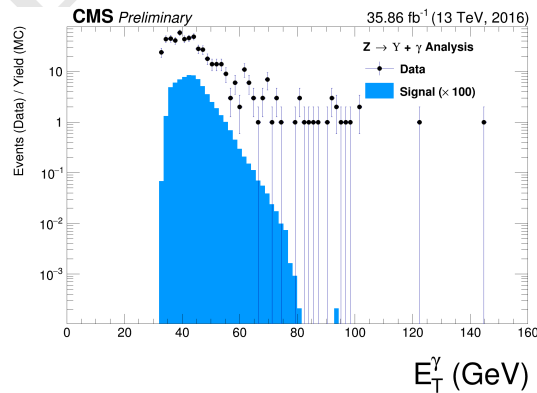


Figure 4.33: The p_T photon distributions from data and signal events for Z decaying in $\Upsilon(1S, 2S, 3S) + \gamma$ all (Group I+II) selection cuts. The plot is normalized to the number of events. Signal sample is scaled by a factor of $\times 100$.

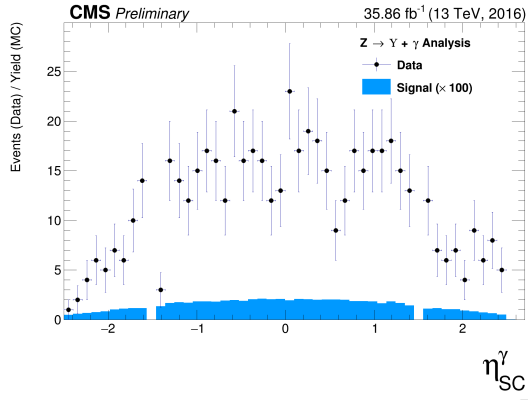


Figure 4.34: The η photon distributions from data and signal events of Z decaying in $\Upsilon(1S, 2S, 3S) + \gamma$ after all (Group I+II) selection cuts. The plot is normalized to the number of events. Signal sample is scaled by a factor of $\times 100$.

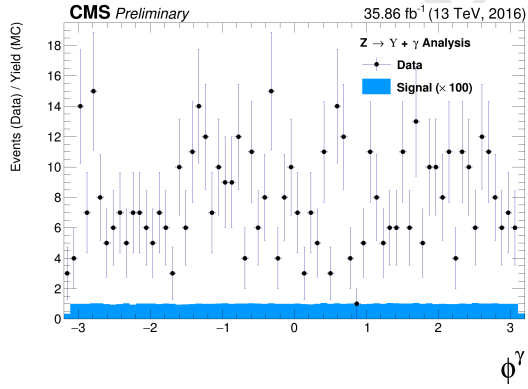


Figure 4.35: The ϕ photon distributions from data and signal events of Z decaying in $\Upsilon(1S, 2S, 3S) + \gamma$ after all (Group I+II) selection cuts. The plot is normalized to the number of events. Signal sample is scaled by a factor of $\times 100$.

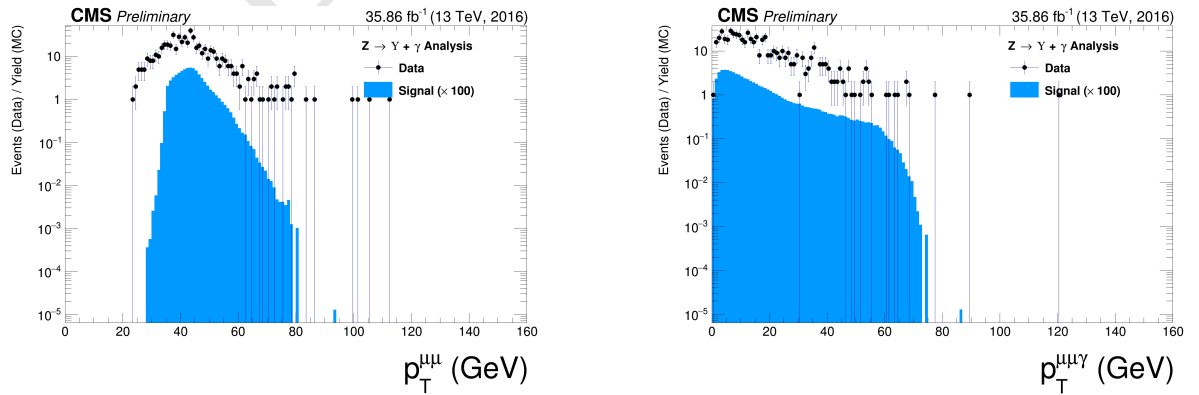


Figure 4.36: The p_T distributions for $\Upsilon(1S, 2S, 3S)$ in the left and for Z in the right from data and signal events for Z decaying in $\Upsilon(1S, 2S, 3S) + \gamma$ after all (Group I+II) selection cuts. The plots are normalized to the number of events. Signal sample is scaled by a factor of $\times 100$.

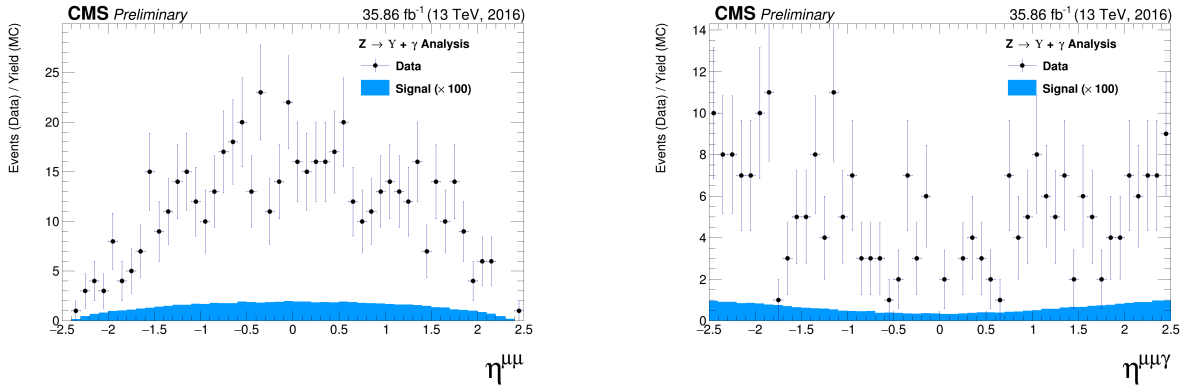


Figure 4.37: The η distributions for $\Upsilon(1S, 2S, 3S)$ in the left and for Z in the right from data and signal events for Z decaying in $\Upsilon(1S, 2S, 3S) + \gamma$ after all (Group I+II) selection cuts. The plots are normalized to the number of events. Signal sample is scaled by a factor of $\times 100$.

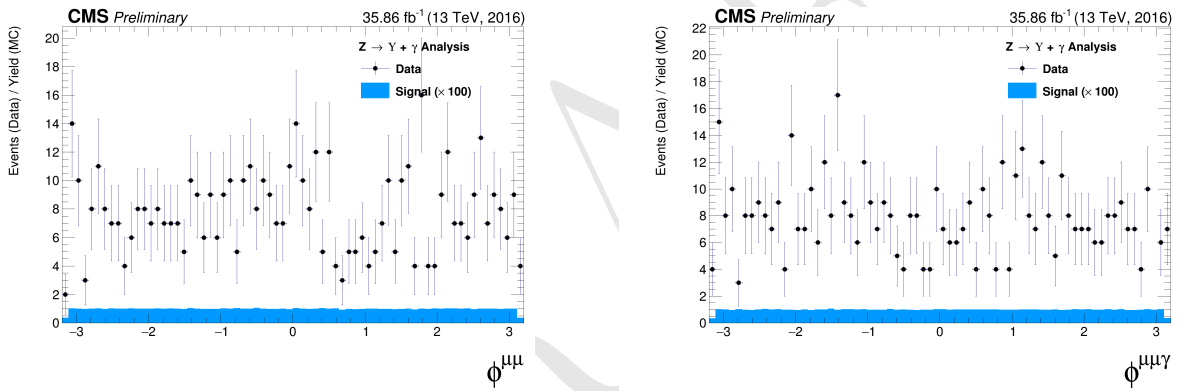


Figure 4.38: The ϕ distributions for $\Upsilon(1S, 2S, 3S)$ in the left and for Z in the right from data and signal events for Z decaying in $\Upsilon(1S, 2S, 3S) + \gamma$ after all (Group I+II) selection cuts. The plots are normalized to the number of events. Signal sample is scaled by a factor of $\times 100$.

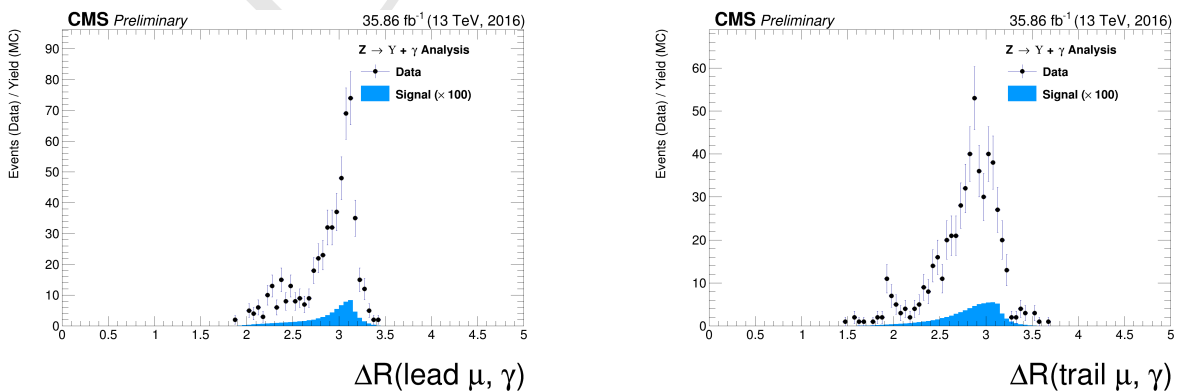


Figure 4.39: The ΔR distributions between the photon and the leading muon (left) and the trailing muon (right) for $\Upsilon(1S, 2S, 3S)$ from data and signal events for Z decaying after all (Group I+II) selection cuts. The plots are normalized to the number of events. Signal sample is scaled by a factor of $\times 100$.

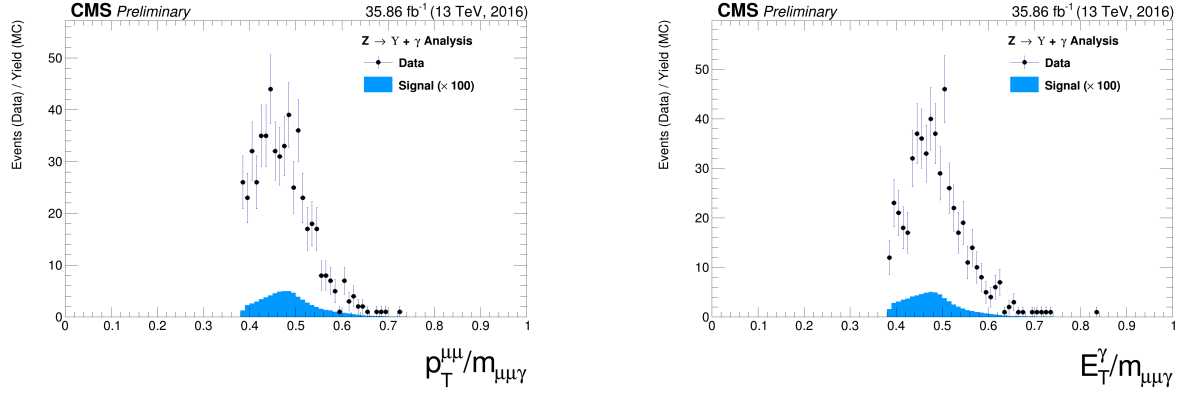


Figure 4.40: The ratio for the transverse momentum of the reconstructed Upsilon and the reconstructed Z mass ($p_T^{\mu\mu}/M_{\mu\mu\gamma}$ - left) and the ratio for the transverse energy of the reconstructed Photon and the reconstructed Z mass ($E_T^\gamma/M_{\mu\mu\gamma}$ - right) distribution for $\Upsilon(1S, 2S, 3S)$ from data and signal events for Z decaying after all (Group I+II) selection cuts. The plots are normalized to the number of events. Signal sample is scaled by a factor of $\times 100$.

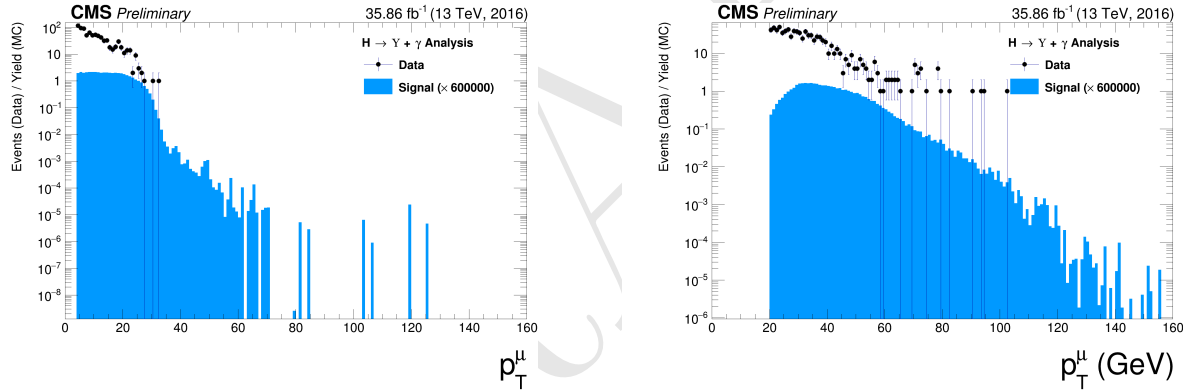


Figure 4.41: The p_T muon distributions from data and signal events for Higgs decaying in $\Upsilon(1S, 2S, 3S) + \gamma$ after Group I of selection cuts, where on left are presenting the trailing muons and on right are the leading muons. The plots are normalized to the number of events. Signal sample is scaled by a factor of $\times 600000$.

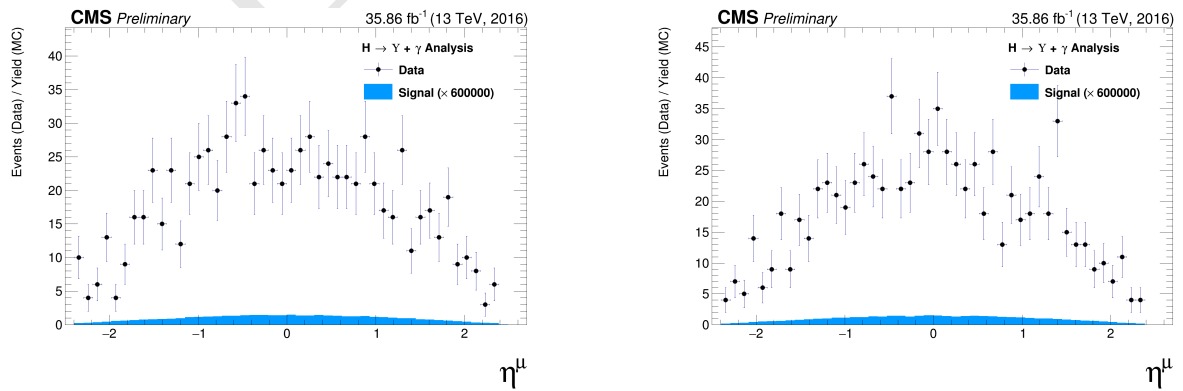


Figure 4.42: The η muon distributions from data and signal events of Higgs decaying in $\Upsilon(1S, 2S, 3S) + \gamma$ after Group I of selection cuts, where on left are presenting the trailing muons and on right are the leading muons. The plots are normalized to the number of events. Signal sample is scaled by a factor of $\times 600000$.

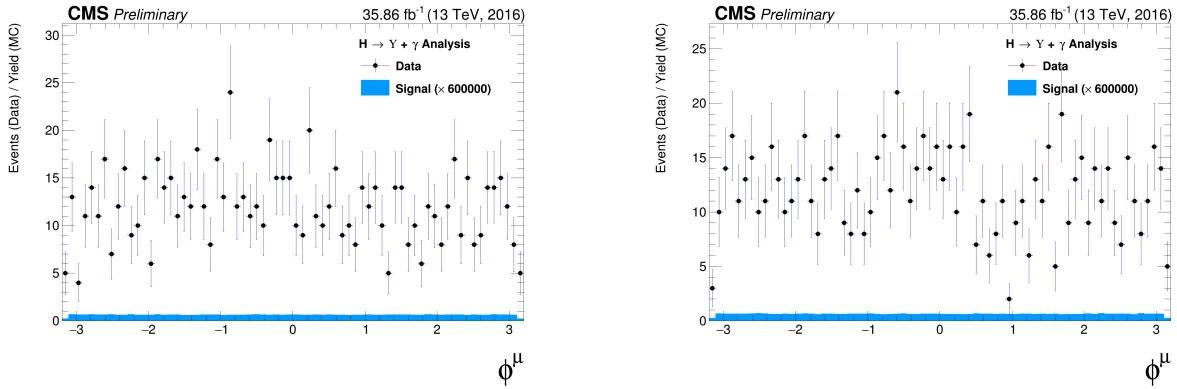


Figure 4.43: The ϕ muon distributions from data and signal events of Higgs decaying in $\Upsilon(1S, 2S, 3S) + \gamma$ after Group I of selection cuts, where on left are presenting the trailing muons and on right are the leading muons. The plots are normalized to the number of events. Signal sample is scaled by a factor of $\times 600000$.

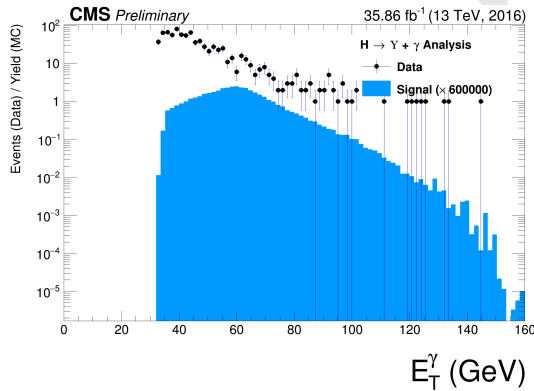


Figure 4.44: The p_T photon distributions from data and signal events for Higgs decaying in $\Upsilon(1S, 2S, 3S) + \gamma$ all (Group I+II) selection cuts. The plot is normalized to the number of events. Signal sample is scaled by a factor of $\times 600000$.

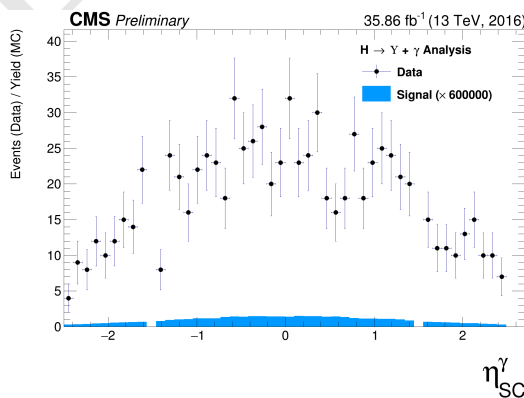


Figure 4.45: The η photon distributions from data and signal events of Higgs decaying in $\Upsilon(1S, 2S, 3S) + \gamma$ after all (Group I+II) selection cuts. The plot is normalized to the number of events. Signal sample is scaled by a factor of $\times 600000$.

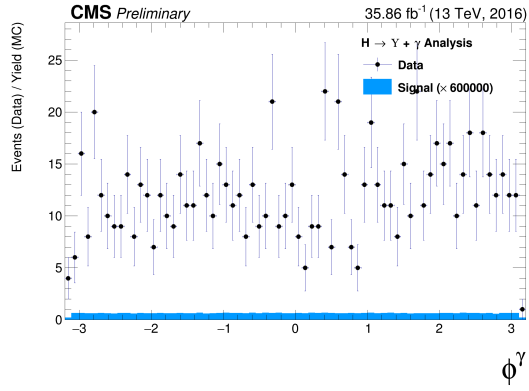


Figure 4.46: The ϕ photon distributions from data and signal events of Higgs decaying in $\Upsilon(1S, 2S, 3S) + \gamma$ after all (Group I+II) selection cuts. The plot is normalized to the number of events. Signal sample is scaled by a factor of c .

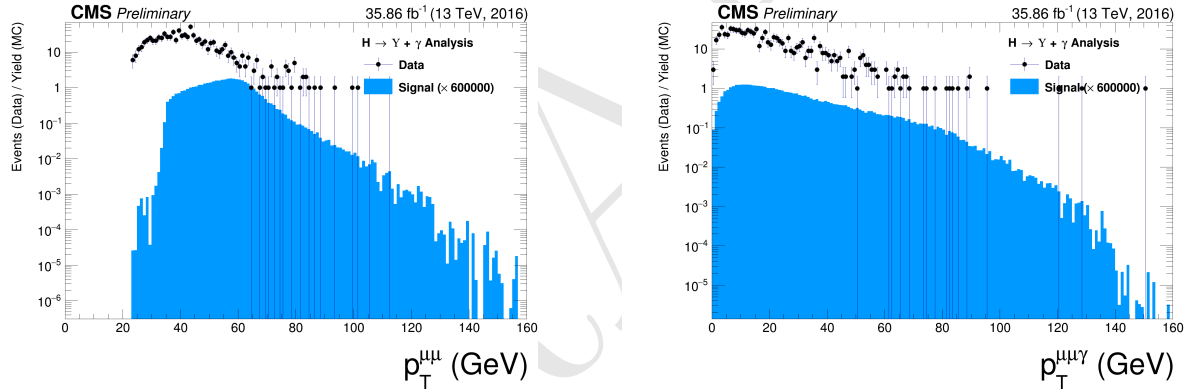


Figure 4.47: The p_T distributions for $\Upsilon(1S, 2S, 3S)$ in the left and for Higgs in the right from data and signal events for Higgs decaying in $\Upsilon(1S, 2S, 3S) + \gamma$ after all (Group I+II) selection cuts. The plots are normalized to the number of events. Signal sample is scaled by a factor of $\times 600000$.

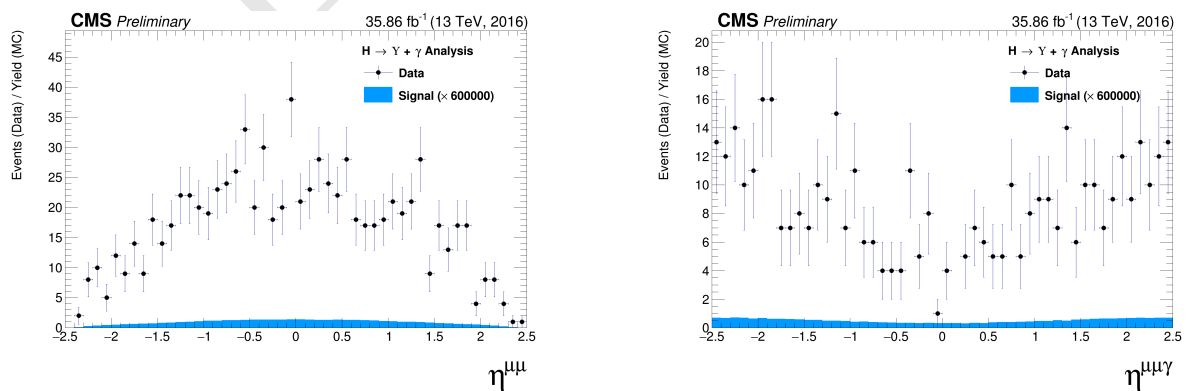


Figure 4.48: The η distributions for $\Upsilon(1S, 2S, 3S)$ in the left and for Higgs in the right from data and signal events for Higgs decaying in $\Upsilon(1S, 2S, 3S) + \gamma$ after all (Group I+II) selection cuts. The plots are normalized to the number of events. Signal sample is scaled by a factor of $\times 600000$.

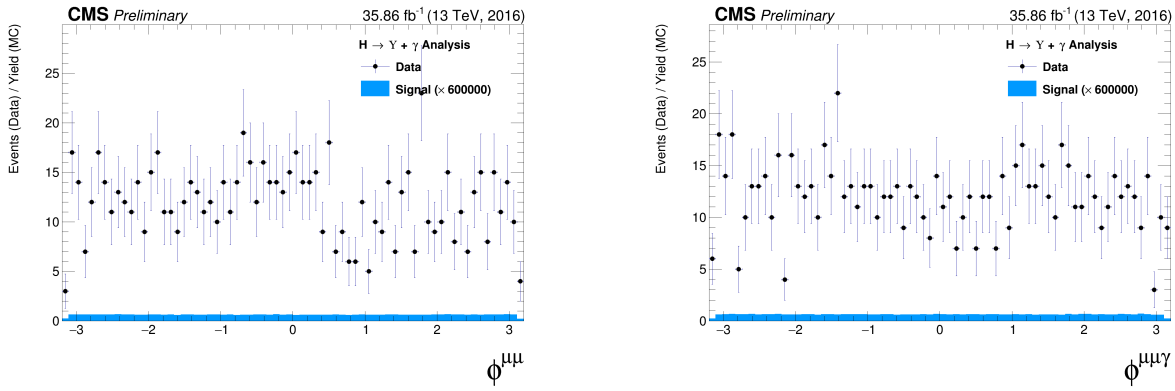


Figure 4.49: The ϕ distributions for $\Upsilon(1S, 2S, 3S)$ in the left and for Higgs in the right from data and signal events for Higgs decaying in $\Upsilon(1S, 2S, 3S) + \gamma$ after all (Group I+II) selection cuts. The plots are normalized to the number of events. Signal sample is scaled by a factor of $\times 600000$.

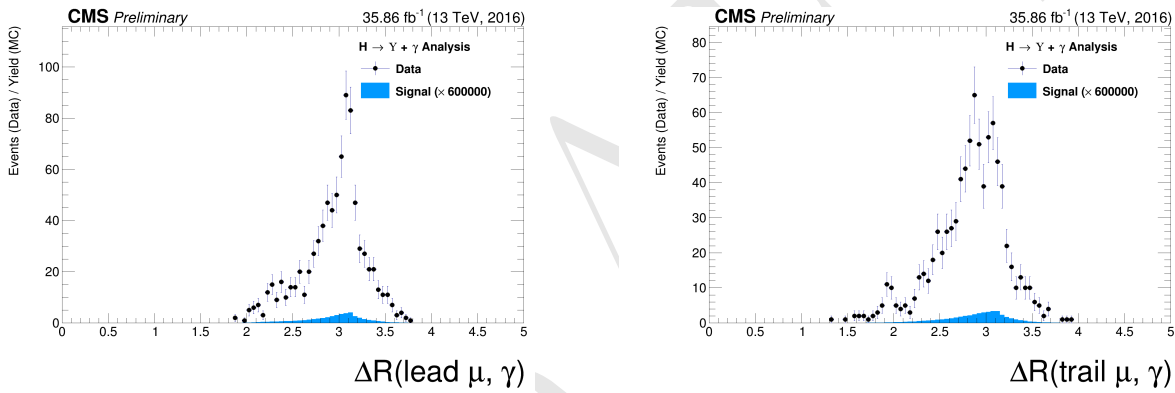


Figure 4.50: The ΔR distributions between the photon and the leading muon (left) and the trailing muon (right) for $\Upsilon(1S, 2S, 3S)$ from data and signal events for Higgs decaying after all (Group I+II) selection cuts. The plots are normalized to the number of events. Signal sample is scaled by a factor of $\times 600000$.

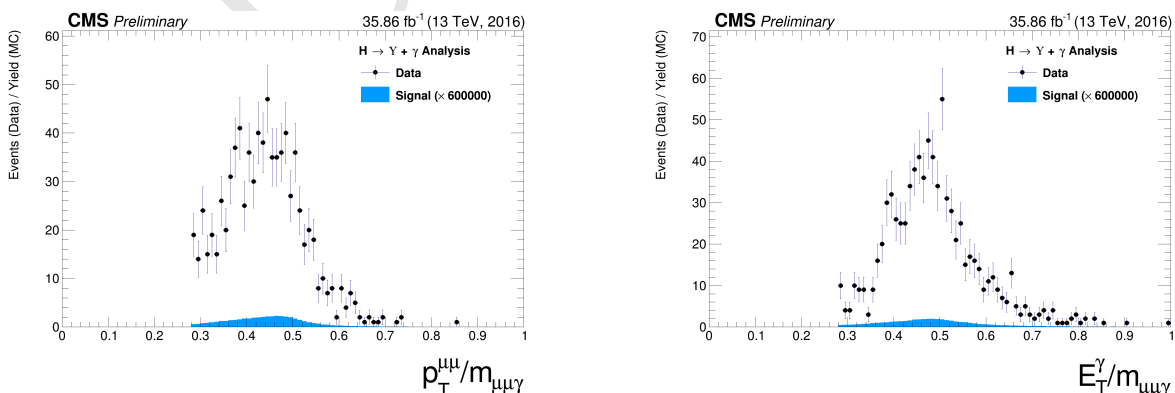


Figure 4.51: The ratio for the transverse momentum of the reconstructed Upsilon and the reconstructed Higgs mass ($p_T^{\mu\mu}/M_{\mu\mu\gamma}$ - left) and the ratio for the transverse energy of the reconstructed Photon and the reconstructed Higgs mass ($E_T^\gamma/M_{\mu\mu\gamma}$ - right) distribution for $\Upsilon(1S, 2S, 3S)$ from data and signal events for Higgs decaying after all (Group I+II) selection cuts. The plots are normalized to the number of events. Signal sample is scaled by a factor of $\times 600000$.

485 4.7 Event categorization and yields

486 In order to increase the sensibility of the analysis, a categorization procedure was applied. They
 487 are based on the η and R9 distribution of the reconstructed photon.

488 The photon R9 is a shower shape variable defined as the fraction of energy deposited in the
 489 5x5 square surrounding the Super Cluster seed of the reconstructed photon. A photon that convert
 490 before reaching the ECAL tend to have lower values of R9, in comparison with unconverted photons.
 491 Converted photons have wider energy resolution and are more likely to be misidentified.

492 Selected events with the photon reconstructed inside the barrel and with $R9 > 0.94$ are cat-
 493 egorized as "EB High R9"⁴, selected events with the photon reconstructed inside the barrel and
 494 with $R9 < 0.94$ are categorized as "EB Low R9" and selected events with the photon reconstructed
 495 inside the endcap, regardless of its R9 value, categorized as "EE". This categorization is done in
 496 view of increase the analysis sensitivity.

497 This categorization is implemented only for the Z decay. The Higgs does not present enough
 498 statistics to make it profitable, so only the inclusive one is used.

499 4.7.1 R9 reweighting

500 As spotted by the $H \rightarrow \gamma\gamma$ at $\sqrt{13}$ TeV analysis [54], there is a disagreement in the R9 distri-
 501 bution of photons in Data and MC. In order to mitigate this difference, a transformation factor is
 502 extracted and applied to the reconstructed photons before the categorization.

503 The same approach of the $H \rightarrow \gamma\gamma$ analysis is applied, in which the nominal photon selection of
 504 this analysis (see section 4.5.3) is used to select photons on Data and MC. Then the two distributions
 505 are remapped and the transformation factors are extracted.

506 Figure 4.52 show the R9 distribution before and after the reweighting, for the Barrel and the
 507 Endcap.

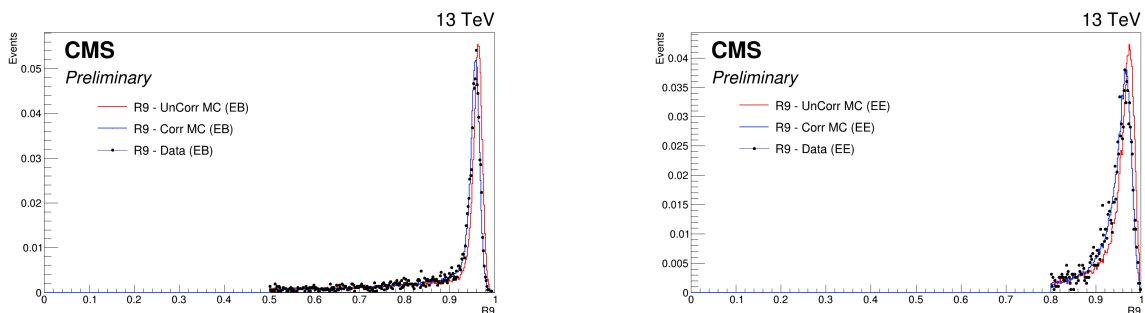


Figure 4.52: Data and MC of the R9 variable, before and after the reweighting. Barrel (left) and Endcap (right).

508 4.7.2 Event counting and yields

509 Tables 4.4 and 4.5 show the total number of events before and after the full selection. Two
 510 things are important to notice.

511 The signal selection efficiency is between 20% and 21% for all Υ states and categories.

⁴EB stands for Electromagnetic Barrel

	Data	Signal			$Z \rightarrow \mu\mu\gamma_{FSR}$
		$Z \rightarrow \Upsilon(1S) + \gamma$	$Z \rightarrow \Upsilon(2S) + \gamma$	$Z \rightarrow \Upsilon(3S) + \gamma$	
Total (before selection)	169.84 M	3.54	1.4	1.22	3.33×10^3
Inclusive	447	0.393	0.157	0.136	176
EB High R9	197	0.172	0.0682	0.0597	78
EB Low R9	146	0.129	0.0519	0.0448	58.5
EE	104	0.0916	0.0365	0.032	39.8

Table 4.4: Number of events for the Z decay, before and after the full selection, per categorization scenarios.

	Data	Signal			$H \rightarrow \gamma\gamma^*$
		$H \rightarrow \Upsilon(1S) + \gamma$	$H \rightarrow \Upsilon(2S) + \gamma$	$H \rightarrow \Upsilon(3S) + \gamma$	
Total (before selection)	169.84 M	0.000257	5.43×10^{-5}	3.93×10^{-5}	136
Inclusive	231	5.23×10^{-5}	1.2×10^{-5}	8.96×10^{-6}	1.22

Table 4.5: Number of events for the H decay, before and after the full selection.

When one compares the fraction of selected peaking background, with respect to the selected data events for the Higgs decay ($1.22/231$), the fraction obtained ($\sim 0.3\%$) is irrelevant. On the other hand, the same fraction for the Z decay ($176/447$) is far from irrelevant ($\sim 39\%$)⁵. The same relation is not found in the $H/Z \rightarrow J/\psi + \gamma$ analysis [23], where both decays (Higgs and Z) show neglectable estimations of peaking background contribution to data. The very same behavior was found by ATLAS [20]. It can be explained by the relatively larger cross-section of the Z peaking background ($Z \rightarrow \mu\mu\gamma_{FSR}$), with respect to the Higgs peaking background (Higgs Dalitz Decay). For the J/ψ channel, it is not an issue since its cross-section is way larger than the peaking background. The figures 4.16 and 4.29 help to clarify these affirmations, for the Z and Higgs decay, respectively. One can easily see how clear the J/ψ peak is in both decays and how minor the Higgs Dalitz Decay contributions is to the Υ peak, with respect to the $Z \rightarrow \mu\mu\gamma_{FSR}$ contribution. It is important to keep in mind the different scaling of the peaking background distributions, x3 for the Z and $\times 100$ for the Higgs. The peaking background to the data due to $Z \rightarrow \Upsilon(1S, 2S, 3S) + \gamma$ channel is the main motivation to use a 2-dimensional modeling fitting of the signal and background events, in order to add one more layer of differentiation between many backgrounds contributions which will be detailed in the next section.

⁵It is worth to keep in mind that this is a estimation based on MC

528 4.8 Background modeling

529 The background modeling proposed for this analysis is a two dimensional unbinned maximum
 530 likelihood fit on the $\mu\mu$ and the $\mu\mu\gamma$ invariant mass distributions. It is considered and modeled, as
 531 briefly discussed in 4.1.2, three kinds of backgrounds:

- 532 • **Full Combinatorial:** any combination of two muon and one photon that pass all the object
 533 reconstruction and event selection criteria.
- 534 • **Υ Combinatorial:** a $\Upsilon(1S, 2S, 3S)$, that decays to a dimuon system, combined with a
 535 misidentified photon (misreconstructed, Pile-up photon, etc.), that pass all the object re-
 536 construction, identification and event selection criteria.
- 537 • **Peaking background:** a Z (or Higgs) that decays straight to a $\mu\mu\gamma$, that pass all the object
 538 reconstruction and event selection criteria, without passing through any intermediate state.
 539 The main contributions considered for this background are $Z \rightarrow \mu\mu\gamma_{FSR}$ (a Z decaying to a
 540 dimuon system with one of the muons irradiating a photon) or a Higgs Dalitz Decay.

541 All of them will be modeled from data, with some inputs from the MC (simulated) samples, as
 542 explained below. For both invariant mass spectra ($\mu\mu$ and $\mu\mu\gamma$) the full combinatorial background is
 543 expected to behave like a non-peaking distribution. The same behavior is expected for the $\mu\mu\gamma$ mass
 544 distribution of the Υ Combinatorial background and for the $\mu\mu$ mass distribution of the peaking
 545 background.

546 On the other hand, the $\mu\mu$ distribution of the Υ Combinatorial background and the $\mu\mu\gamma$ mass
 547 distribution for the peaking background are expected to behave like a peaking distribution, centered
 548 around the $\Upsilon(1S, 2S, 3S)$ invariant mass (9.46 GeV, 10.02 GeV and 10.35 GeV) [2] and the Z
 549 boson invariant mass (91.2 GeV) [2], respectively . Table 4.6 summarizes the background modeling
 550 proposed for this analysis.

	$m_{\mu\mu}$	$m_{\mu\mu\gamma}$
Peaking background	Bernstein 1 st order	Crystal Ball (Higgs decay) Double Crystal Ball (Z decay)
Υ Combinatorial	3 Gaussians (one for each Υ state)	
Full Combinatorial	Chebychev 1 st order	Polynomial

Table 4.6: Modeling for each background source and mass component.

551 For the $Z \rightarrow \Upsilon(1S, 2S, 3S) + \gamma$ analysis, the peaking background model parameters are extracted
 552 by performing a simultaneous 2-dimensional fit over the invariant masses, $m_{\mu\mu}$ and $m_{\mu\mu\gamma}$, of the
 553 simulated $Z \rightarrow \mu\mu\gamma_{FSR}$ MC sample of events that passes the selection described in Section 4.4, as in
 554 figure 4.53. Once the parameters are extracted, they are fixed and the *pdf* (Probability Distributions
 555 Function) of the 2-Dimensional modeling is stored, leaving only the normalization of the *pdf* as a
 556 parameter free to float (this will be determined from data).

557 In order to describe the 2-dimensional invariant mass distribution of the Peaking Background,
 558 as stated in Table 4.6, the $m_{\mu\mu}$ component is described by a Bernstein polynomial of 1st order [55],

which is used here just a representation of a linear function. The $m_{\mu\mu\gamma}$ component is described by Double Crystal Ball function [56]. A Crystal Ball function is a *pdf* composed by a gaussian distribution and a power-law tail to the left, before certain threshold. The Crystal Ball function was named after the Crystal Ball Collaboration (first to use this *pdf*) and it is widely used in high-energy physics to describe mass distributions that incorporate FSR (final state radiation) effects, via the power-law tail. A Double Crystal Ball is a Crystal Ball function with the power-law tail on both sides.

A Crystal Ball function is define as:

$$CB(x; \alpha, n, \bar{x}, \sigma) = N \cdot \begin{cases} \exp(-\frac{(x-\bar{x})^2}{2\sigma^2}), & \text{for } \frac{x-\bar{x}}{\sigma} > -\alpha, \\ A \cdot (B - \frac{x-\bar{x}}{\sigma})^{-n}, & \text{for } \frac{x-\bar{x}}{\sigma} \leq -\alpha \end{cases} \quad (4.4)$$

where,

$$A = \left(\frac{n}{|\alpha|} \right)^n \cdot \exp \left(-\frac{|\alpha|^2}{2} \right),$$

$$B = \frac{n}{|\alpha|} - |\alpha|,$$

$$N = \frac{1}{\sigma(C+D)},$$

$$C = \frac{n}{|\alpha|} \cdot \frac{1}{n-1} \cdot \exp \left(-\frac{|\alpha|^2}{2} \right),$$

$$D = \sqrt{\frac{\pi}{2}} \left(1 + \operatorname{erf} \left(\frac{|\alpha|}{\sqrt{2}} \right) \right),$$

and erf is the error function.

For the three gaussian functions fits, which represent the three Υ states (1S, 2S and 3S) from the Υ Combinatorial background in the $m_{\mu\mu}$ component, we use a Υ control sample in order to extract the fit parameters, including the relative normalization between each Υ state. This sample is composed by dimuon candidates obtained from data, by selecting the events that passes the same trigger and dimuon selection of the nominal selection and with $p_T^{\mu\mu} > 35$ GeV (this cut is done in order to keep this selected dimuon candidates compatibles with the $p_T^{\mu\mu}/M_{\mu\mu\gamma}$ cut applied in the nominal selection). No selection or cuts in the photon are required.

This control sample is fitted with a Chebychev 1st order (linear polynomial) for the background support and 3 gaussian with the following constraints:

- the mean of each state should be the ones in the PDG [2], but allowed to shift by a float and common (the same for all states) value.
- the sigma should be based on the 1S fit of the MC. All other sigma should be the result of the 1S sigma times the state mass over the 1S mass ($\sigma_{2S,3S} = \frac{m_{2S,3S}}{m_{1S}} \sigma_{1S}$).

The idea behind this fit is that scale and resolution (mean and sigma, respectively, of the gaussians) over a sample without a photon selection should be the same as over a sample with photon selection, since these are detector only dependent effects. The fact that we exclude the photon from this control sample, improves the statistics and gives a better measurement of these variables.

The fit of the Υ control sample if shown in figure 4.54.

Once determined, the fit parameters are fixed, they are used to compose the 2-Dimensional *pdf*. The $m_{\mu\mu}$ component of the full combinatorial background is derived fully from the data fit

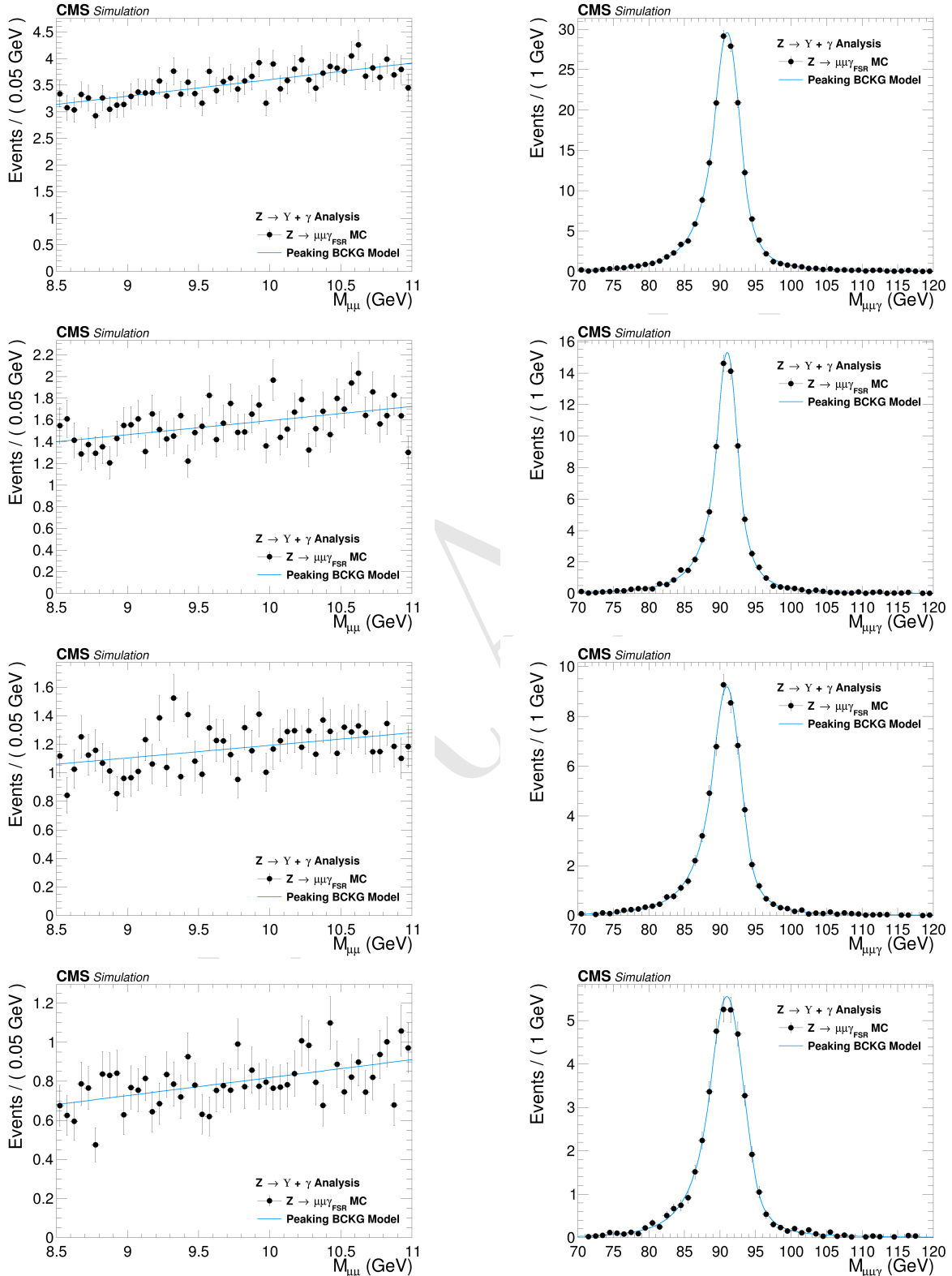


Figure 4.53: Peaking background for the $Z \rightarrow \Upsilon(1S, 2S, 3S) + \gamma$ analysis. $\mu\mu$ mass distribution (left) and $\mu\mu\gamma$ invariant mass distribution (right). From top to bottom categories: Inclusive, EB High R9, EB Low R9, EE.

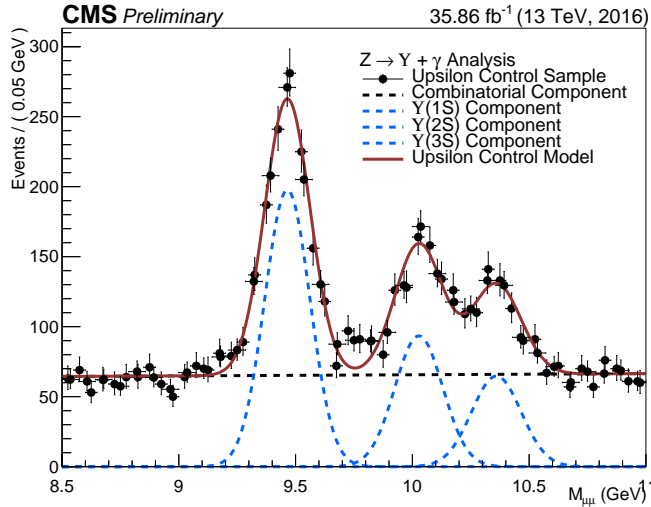


Figure 4.54: Υ control sample fit with Chebychev 1st order for the background support and 3 gaussian for the three $\Upsilon(1S, 2S, 3S)$ peaks.

(described below). In the same sense, the $m_{\mu\mu\gamma}$ component of the full combinatorial and the $\Upsilon(nS)$ Combinatorial backgrounds are also fully derived from the data, but following a more complex procedure: a composition with the *pdf* components described above, plus a statistical test, to avoid overfitting within a Discrete Profiling (or "Envelope Method"), as described in [57] and also implemented in [54].

The statistical test consists of, for each category, different orders of a set of polynomial *pdfs* families are tested: a sums of exponentials, sum of polynomials (in the Bernstein basis), a Laurent series and a sums of power-law functions.

- Sums of exponentials:

$$f_N(x) = \sum_{i=1}^N p_{2i} e^{p_{2i+1}x},$$

- Sums of polynomials (in the Bernstein basis):

$$f_N(x) = \sum_{i=0}^N p_i b_{(i,N)}, \text{ where } b_{(i,N)} := \binom{N}{i} x^i (1-x)^{N-i},$$

- Laurent series:

$$f_N(x) = \sum_{i=1}^N p_i x^{-4+\sum_{j=1}^i (-1)^j(j-1)},$$

- Sums of power-law functions:

$$f_N(x) = \sum_{i=1}^N p_{2i} x^{-p_{2i+1}},$$

where for all k , the p_k are a set of floating parameters in the fit.

Twice difference in the negative log-likelihood (NLL) between the N^{th} and the $(N+1)^{th}$ order of the same polynomial ($\Delta NLL = 2 \times (NLL_N - NLL_{N+1})$) is expected to follow a χ^2 distribution

606 with M degrees of freedom, where M is the increase in degrees of freedom when going from N^{th} to
 607 $(N+1)^{th}$. This can be shown with the help of the Wilks' theorem [58].

608 Starting from the lowest order possible, the best choice of order, for each family, is determined
 609 when a increase in the order of the polynomial, does not brings a significant improvement in the
 610 quality of the fit. Since a model with more fit parameters (higher order polynomials) will always
 611 perform, if not the same, better than a simpler one, an optimal choice of the polynomial order, will
 612 be the one right before the model becomes too flexible for the data.

613 Consider a p -value defined as:

$$\begin{aligned} p\text{-value} &= \int_{\Delta NLL}^{\infty} \chi_M^2(\Delta) d\Delta \\ &= P(\chi_M^2 > \Delta NLL), \end{aligned} \quad (4.5)$$

614 In the same spirit as the Wilks' theorem, this is the p -value for a likelihood ratio test between a
 615 null hypotheses and an alternative model, where the null hypotheses is the N^{th} order and $(N+1)^{th}$
 616 order is the alternative one.

$$\begin{aligned} \Delta NLL &= 2 \times (NLL_N - NLL_{N+1}) \\ &= -2 \times \log\left(\frac{\mathcal{L}_N}{\mathcal{L}_{N+1}}\right), \end{aligned} \quad (4.6)$$

617 where \mathcal{L}_N is the likelihood for the N^{th} polynomial order.

618 The alternative will present a statistically significant improvement, with respect to the null
 619 hypotheses, if the p -value is smaller than 0.05, since the probability of obtaining, by chance, con-
 620 sidering the null hypotheses is true, a even higher ΔNLL is less than 5%. This will give support
 621 to chose $(N+1)^{th}$ over N^{th} .

622 If the p -value is greater than 0.05 a higher order is not supported, since the probability of
 623 obtaining a ΔNLL greater than the one observed is statistically significant (more than 5%). A
 624 higher ΔNLL means that another data sample, collected and analyzed with strictly the same
 625 conditions, would have a probability of more than 5% of giving a better fit improvement than the
 626 one observed, again assuming that the null hypotheses is true. This is an indication of overfitting,
 627 since the improvements are likely to come from just statistical fluctuations. When testing the
 628 $(N+1)^{th}$ order and this condition is reached, the optimal order should be the N^{th} .

629 At first, before any fit to data, the 2-Dimensional model is composed by the five components,
 630 as described in Table 4.6 (in which the $m_{\mu\mu\gamma}$ modeling for the Full Combinatorial Background and
 631 the Υ combinatorial are shared), then, the statistical test described before is ran for each family.
 632 It is important to stress that before the statistical test all the other fitting parameters have been
 633 fixed. This leaves only the normalizations of the model components and the polynomial coefficients
 634 free to float.

635 Once the optimal order for each pdf family is obtained, the composed pdf with each choice from
 636 statistical test is save in the same model, providing a discrete variable that indexes the different
 637 polynomial pdf families. This method is called Discrete Profiling (or "Envelope Method") and it

allows the analysis algorithm to treat the choice of the *pdf* as a systematics and incorporate its effect in the extracted upper limits. This model, with different choices of polynomial families is called envelope.

The implementation, used in the analysis, of the F-Test and the Discrete Profiling is based on the same algorithm used by the $H \rightarrow \gamma\gamma$ Run II analysis. An extensive documentation on these methods can be found in $H \rightarrow \gamma\gamma$ analysis note and physics analysis summary [59, 60] and in the specific reference of the Discrete Profiling [57]. The figures 4.55 and 4.56 show the projection for the $\mu\mu$ and $\mu\mu\gamma$ distribution after the F-Test.

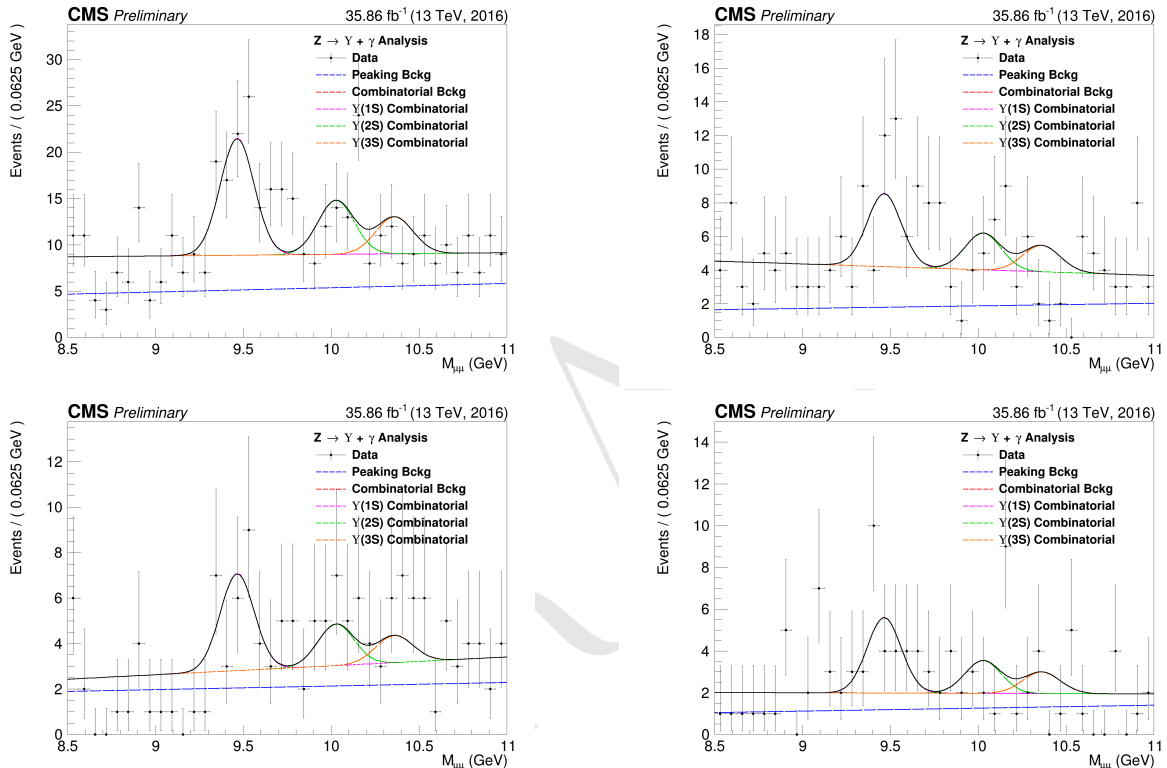


Figure 4.55: $Z \rightarrow \Upsilon(1S, 2S, 3S) + \gamma$ Background Modeling: $\mu\mu$ distribution. Inclusive (top left); EB High R9 (top right), EB Low R9 (bottom left), EE (bottom right). The pdfs projections are plotted with respect to the overall best choice of the statistica test.

For the $H \rightarrow \Upsilon(1S, 2S, 3S) + \gamma$ analysis, the same procedure is implemented, except for the peaking background modeling. Since the MC prediction for the contribution of the background is too small, according to the comparison between the final selected events for data and the Higgs Dalitz Decay sample, in order to avoid fitting over statistical fluctuations of the data sample, the Peaking Background, for the Higgs channel, is fully modeled from the MC sample, including its normalization, as shown in figure 4.57, hence it is not included the the statistical test, neither in the final background modeling envelope.

The results of the background modeling for the Full Combinatorial and Υ Combinatorial, can be found at Figures 4.58 and 4.59, for the $\mu\mu$ and $\mu\mu\gamma$ distribution, respectively. It is worth to remember that, for the Higgs channel, we are not implementing any categorization.

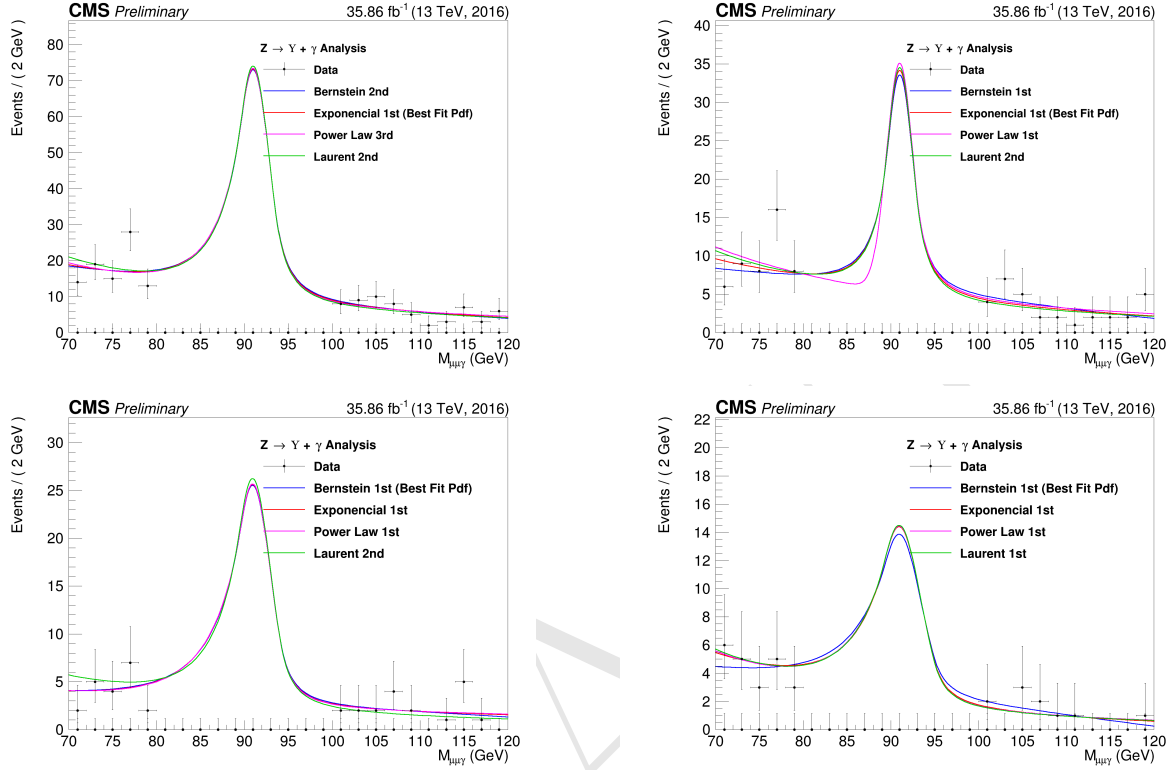


Figure 4.56: $Z \rightarrow \Upsilon(1S, 2S, 3S) + \gamma$ Background Modeling: $\mu\mu\gamma$ distribution. Inclusive (top left); EB High R9 (top right), EB Low R9 (bottom left), EE (bottom right). The plotted *pdfs* corresponds to the best choice by the statistical test for each family. The signal region, from 80 GeV to 100 GeV was blinded.

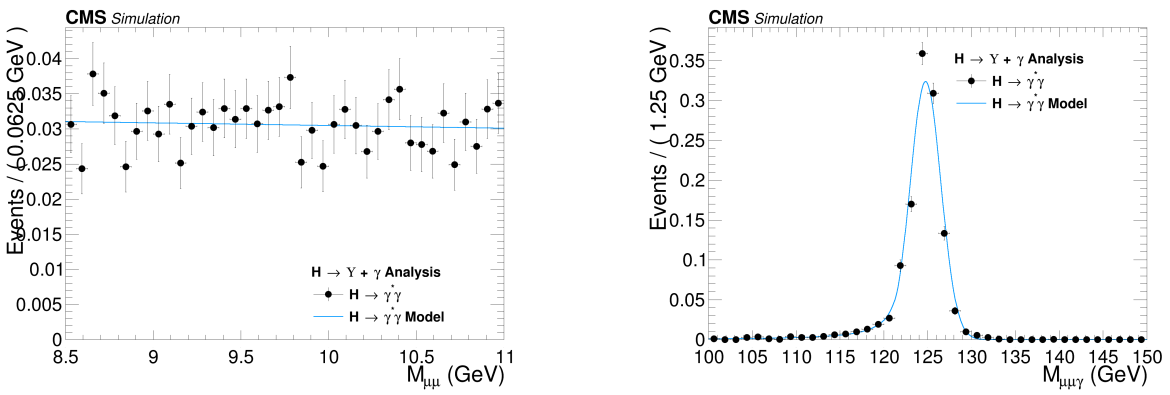


Figure 4.57: Peaking Background for the $H \rightarrow \Upsilon(1S, 2S, 3S) + \gamma$ analysis. $m_{\mu\mu}$ invariant mass distribution (left) and $m_{\mu\mu\gamma}$ invariant mass distribution (right).

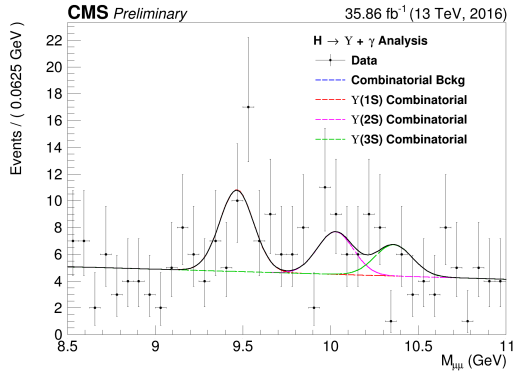


Figure 4.58: $H \rightarrow \Upsilon(1S, 2S, 3S) + \gamma$ Background Modeling: $m_{\mu\mu}$ distribution. The *pdfs* projections are plotted with respect to the overall best choice of the statistical test.

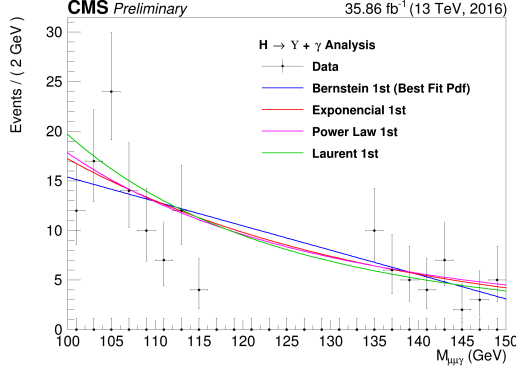


Figure 4.59: $H \rightarrow \Upsilon(1S, 2S, 3S) + \gamma$ Background Modeling: $\mu\mu\gamma$ distribution. The plotted *pdfs* corresponds to the best choice by the statistical test for each family. The signal region, from 115 GeV to 135 GeV was blinded.

656 4.9 Signal modeling

657 Along the same lines as the background modeling (Section 4.8), the signal modeling is imple-
 658 mented as a two dimensional unbinned maximum likelihood fit on the $m_{\mu\mu}$ and the $m_{\mu\mu\gamma}$ invariant
 659 masses distributions, but this time, only using the signal simulated MC samples 4.1.2. Since, for
 660 the two spectra, it is expected a peak-like distribution, one centered in the Z (or Higgs) boson mass
 661 and the other centered in the Υ mass, two also peak-like analytics *pdfs* were chosen to compose the
 662 signal model. The modeling is summarized in table 4.7.

	$m_{\mu\mu}$	$m_{\mu\mu\gamma}$
$Z \rightarrow \Upsilon(1S, 2S, 3S) + \gamma$	Double Crystal Ball	Double Crystal Ball
$H \rightarrow \Upsilon(1S, 2S, 3S) + \gamma$	Double Crystal Ball	Crystal Ball + Gaussian with the same mean

Table 4.7: Modeling for each signal source and mass component.

663 The projections of the modeling for the Z boson decay channel analysis can be found at figures
 664 4.60, 4.61, 4.62 and 4.63, for Inclusive, EB High R9, EB Low R9 and EE, respectively. The projection
 665 on the modeling for the Higgs boson signal can be found at Figure 4.64. A deeper discussion on the
 666 systematics uncertainties associated to them, will be presented in the next section.

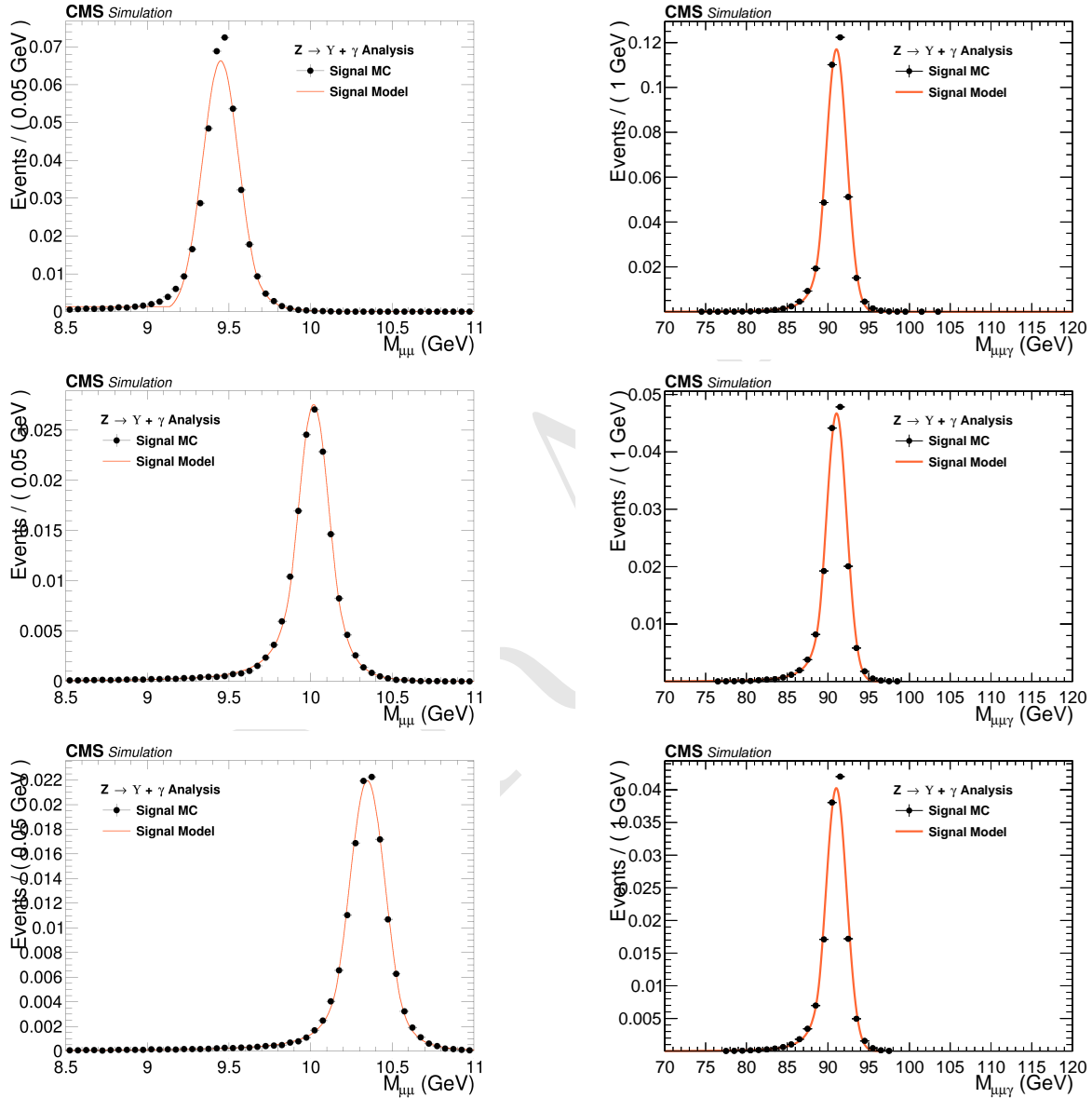


Figure 4.60: Signal Modeling for the $Z \rightarrow \Upsilon(1S, 2S, 3S) + \gamma$ analysis for Inclusive category. $m_{\mu\mu}$ mass distribution (left) and $m_{\mu\mu\gamma}$ mass distribution (right). From top to bottom: $\Upsilon(1S)$, $\Upsilon(2S)$, $\Upsilon(3S)$.

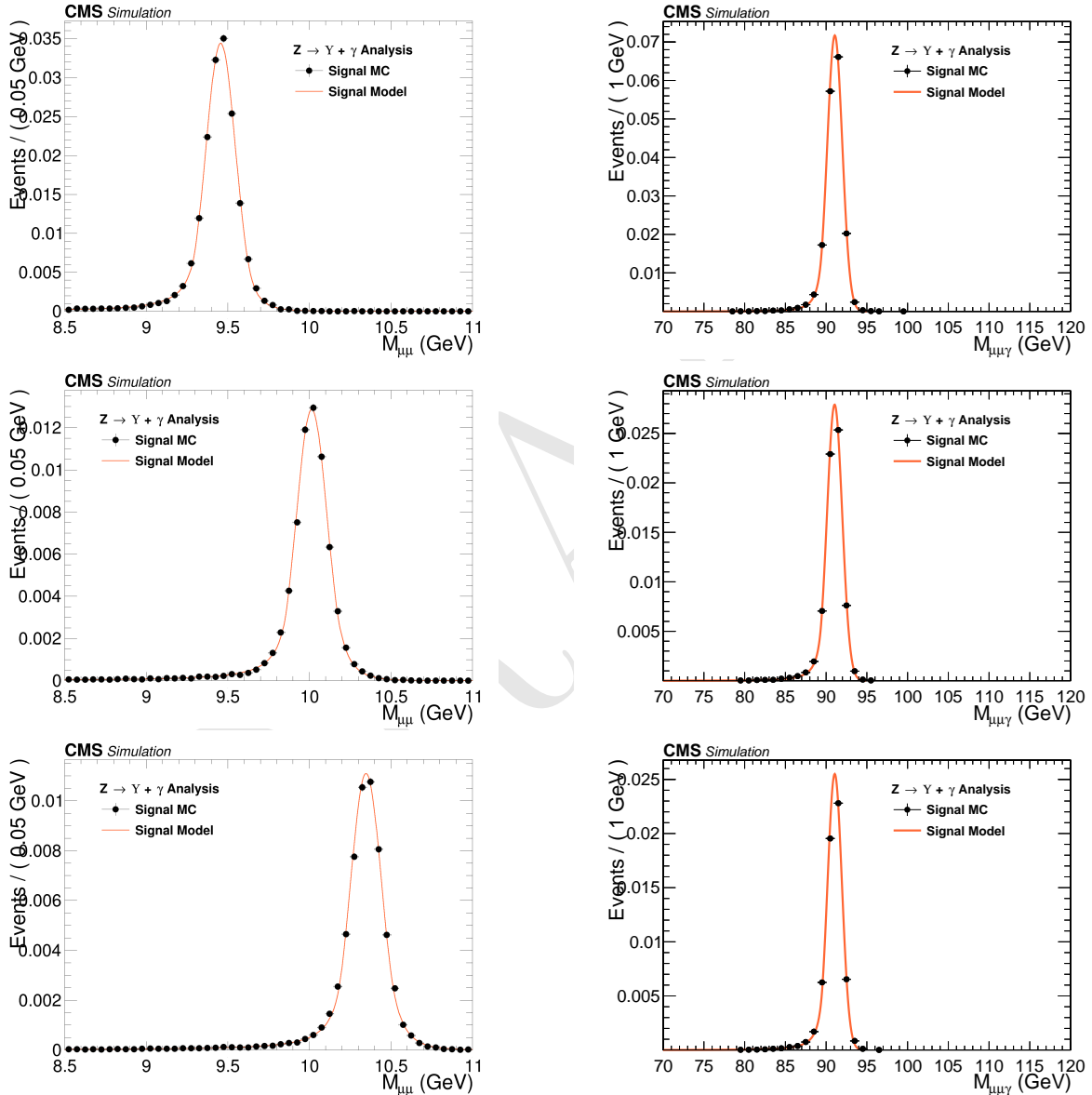


Figure 4.61: Signal Modeling for the $Z \rightarrow \Upsilon(1S, 2S, 3S) + \gamma$ analysis for EB High R9 category. $m_{\mu\mu}$ mass distribution (left) and $m_{\mu\mu\gamma}$ mass distribution (right). From top to bottom: $\Upsilon(1S)$, $\Upsilon(2S)$, $\Upsilon(3S)$.

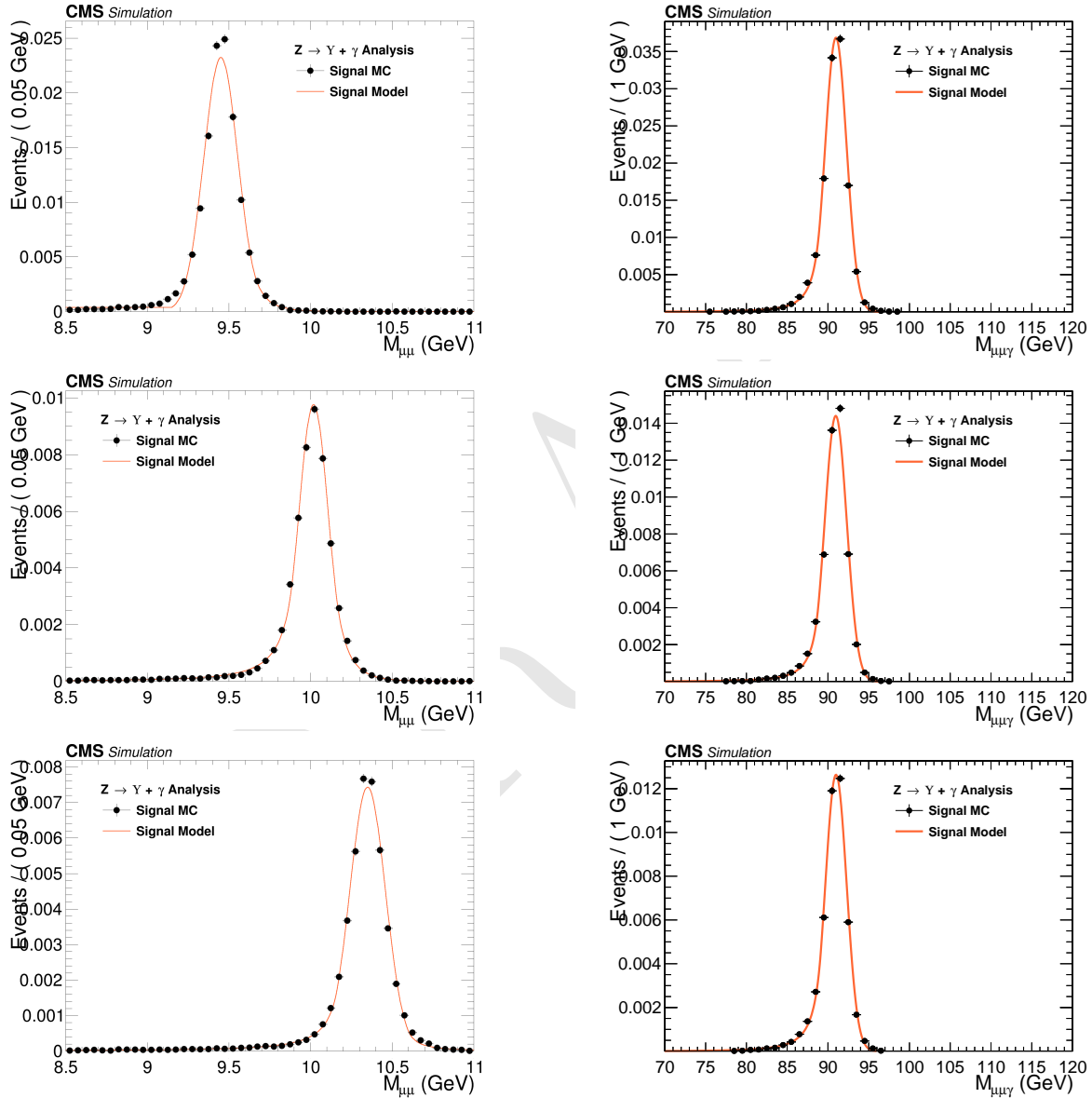


Figure 4.62: Signal Modeling for the $Z \rightarrow \Upsilon(1S, 2S, 3S) + \gamma$ analysis for EB Low R9 category. $m_{\mu\mu}$ mass distribution (left) and $m_{\mu\mu\gamma}$ mass distribution (right). From top to bottom: $\Upsilon(1S)$, $\Upsilon(2S)$, $\Upsilon(3S)$.

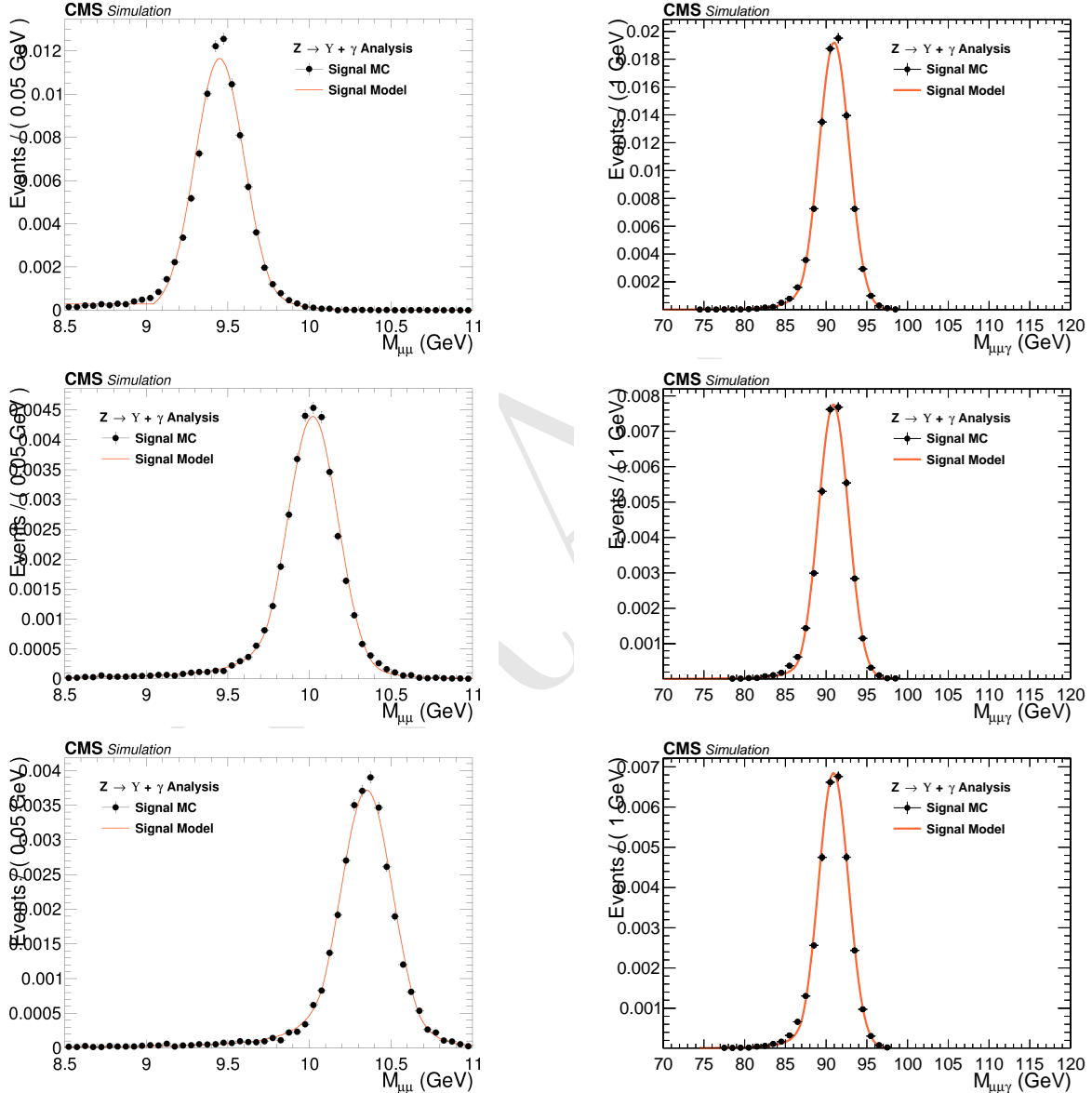


Figure 4.63: Signal Modeling for the $Z \rightarrow \Upsilon(1S, 2S, 3S) + \gamma$ analysis for EE category. $m_{\mu\mu}$ mass distribution (left) and $m_{\mu\mu\gamma}$ mass distribution (right). From top to bottom: $\Upsilon(1S)$, $\Upsilon(2S)$, $\Upsilon(3S)$.

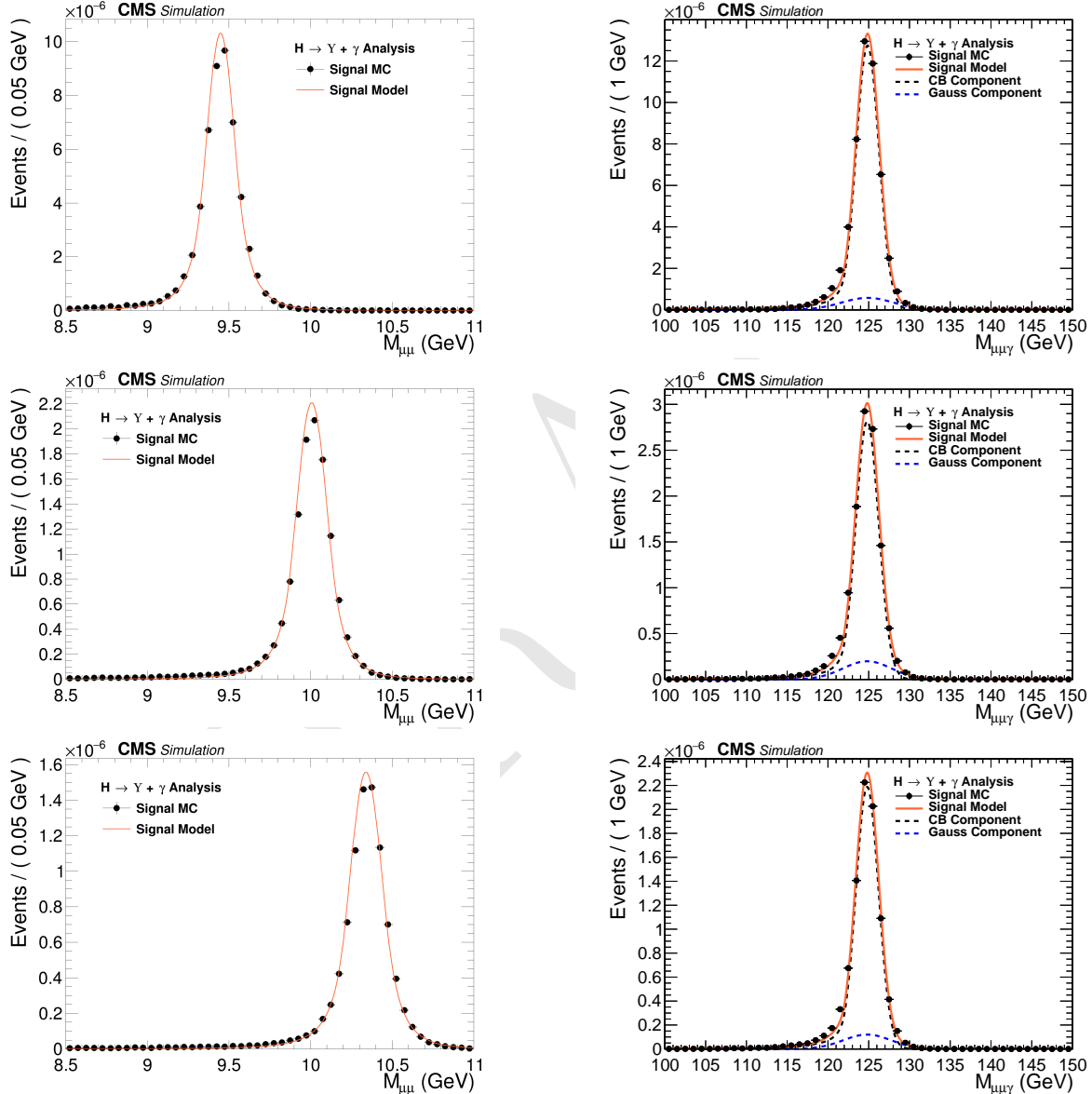


Figure 4.64: Signal Modeling for the $H \rightarrow \Upsilon(1S, 2S, 3S) + \gamma$. $m_{\mu\mu}$ mass distribution (left) and $m_{\mu\mu\gamma}$ mass distribution (right). From top to bottom: $\Upsilon(1S)$, $\Upsilon(2S)$, $\Upsilon(3S)$.

667 4.10 Systematic uncertainties

668 The sources of systematic uncertainties considered are those affect the predicted yields, as shown
 669 in Section 4.7.2, such as, luminosity measurement [32], the pile-up description in the simulations,
 670 the corrections applied to the simulated events in order to compensate for the differences in per-
 671 formance of the some selection criteria as the trigger, object reconstruction and identification, the
 672 Υ polarization and the theoretical uncertainties, such as the effects of the *parton density functions*
 673 (PDF) to the signal cross section [41, 61, 62], the variations of the renormalization and factorization
 674 scales [63–67], and the prediction of the decay branching ratios.

675 The other kind uncertainties affect the shape of the signal model. Those are related with possible
 676 imprecisions of the momentum scale and resolution and they are measured as how they affect the
 677 the mean and sigma of the signal model. For the background modeling, since it is derived from
 678 data, the choice of the *pdf* (Probability distribution function) is the only systematic uncertainties
 679 considered. It is treated by the Discrete Profiling method, as described in section 4.8. The two
 680 kinds of systematics uncertainties are described in details below.

681 4.10.1 Uncertainties on the predicted signal yields

- 682 • **Theoretical uncertainties:** the theoretical sources of uncertainties includes: PDF uncer-
 683 tainties, α_s uncertainty, QCD scale uncertainty and uncertainty on the $H \rightarrow \gamma\gamma$ branching
 684 fraction (used to derive the Higgs Dalitz Decays cross-section). The values for these theoretical
 685 uncertainties are taken from the Higgs Combination Group [44] and also from [68].
- 686 • **Luminosity:** an uncertainty value of 2.5% is used on the integrated luminosity of the data
 687 samples, as recommended by CMS [32].
- 688 • **Pile-up:** the total inelastic cross section of 69.2 mb for minimum bias is varied by $\pm 4.6\%$
 689 and the analysis is ran with the extreme values. The systematic uncertainty quoted is the
 690 maximum difference in the yields with respect to nominal value, as recommended by CMS
ADICIONAR REFERÊNCIA .
- 692 • **Trigger efficiency:** the analysis is ran applying $\pm 1\sigma$ on the Trigger Efficiency Scale factors
 693 (ref. section 4.5.1). The systematic uncertainty quoted is the maximum difference in the
 694 yields with respect to nominal value.
- 695 • **Photon Identification:** the analysis is ran applying $\pm 1\sigma$ on the scale factors (ref. section
 696 4.5.3) for the Photon MVA ID and the Electron Veto. The systematic uncertainty quoted is
 697 the maximum difference in the yields with respect to nominal value.
- 698 • **Muon Identification/Isolation:** the analysis is ran applying $\pm 1\sigma$ on the scale factors (ref. section
 699 4.5.2). The systematic uncertainty quoted is the maximum difference in the yields
 700 with respect to nominal value.
- 701 • **Υ Polarization:** the analysis is ran applying with the extremes scenarios of the Υ polariza-
 702 tion (Transverse and Longitudinal Polarization), applying different reweightings to the signal
 703 samples (ref. section 4.2). The systematic uncertainty quoted is the maximum difference in

704 the yields with respect to nominal (Unpolarized) yield. This procedure is applied only for the
 705 Z decay. For the Higgs decay, the only polarization considered is the transverse polarization.

706 The effect of all systematic uncertainties in the signal and peaking background yields are summa-
 707 rized on table 4.8, for the Z decay and table 4.9, for the Higgs decay. Clearly, the main contribution
 708 to the systematics uncertainties on the yields is Polarization of the $\Upsilon(nS)$ (only for the Z decay),
 709 around 15%.

710 4.10.2 Uncertainties that affect the signal fits

711 Smearing and scaling corrections are applied on simulated events since the resolution of Monte
 712 Carlo is better than that on data and the detector might not catch all the possible differences in
 713 the detector performance, with respecto the real data observation. They need to be estimated and
 714 included on the systematics. The corrections are:

- 715 • **Muon Momentum Scale and Resolution:** extracted by running the analysis with different
 716 setups of the official CMS Muon scaling and smearing package **ADICIONAR REFERÊN-
 717 CIA - MUON PERFORMANCE**. The deviations, with respect to the default correction
 718 are summed in quadrature. Once the nominal parameters (mean or sigma) are obtained, the
 719 default corretions are shifted by $\pm 1\sigma$ and the fits are re-done, with the parameters of interest
 720 free to float and all others fixed. The systematic uncertainty quoted is the maximum difference
 721 of the parameter with respect to nominal value.
- 722 • **Photon Energy Scale and Resolution:** extracted by running the analysis with different
 723 sets of corrections, provided by the CMS **ADICIONAR REFERÊNCIA - EGAMMA
 724 PERFORMANCE**. Once the nominal mean is obtained, the sets are changed and the fits
 725 are re-done, with the mean free to float and all others parameters fixed. The corrections are
 726 shifted by $\pm 1\sigma$ on each source of systematics (following standard CMS recommendations).
 727 The quoted as systematic uncertainty is the quadrature sum of the maximum deviation within
 728 each set.

729 The effective systematic uncertainty associated with the scale and resolution are the quadrature
 730 sum of the muon and photon contributions. The effect of all systematic uncertainties in the Signal
 731 fits are summarized on table 4.10, for the Z and Higgs decay.

Source	Uncertainty			
	Signal		Peaking Background	
	$Z \rightarrow \Upsilon(1S)\gamma$	$Z \rightarrow \Upsilon(2S)\gamma$	$Z \rightarrow \Upsilon(3S)\gamma$	$Z \rightarrow \mu\mu\gamma_{FSR}$
Integrated luminosity				
All Categories	2.5%			
SM Z boson σ (scale)				
All Categories	3.5%		5.0%	
SM Z boson σ (PDF + α_s)				
All Categories	1.73%		5.0%	
Pileup Reweighting				
Cat0	0.65%	0.68%	0.71%	0.62%
Cat1	1.01%	1.1%	1.04%	1.06%
Cat2	0.17%	0.08%	0.13%	0.11%
Cat3	1.07%	0.98%	1.26%	0.78%
Trigger				
Cat0	4.45%	4.46%	4.49%	4.71%
Cat1	3.5%	3.5%	3.52%	3.71%
Cat2	3.55%	3.54%	3.58%	3.72%
Cat3	7.52%	7.58%	7.56%	8.13%
Muon Identification				
Cat0	4.82%	4.81%	4.8%	4.52%
Cat1	4.45%	4.45%	4.44%	4.2%
Cat2	4.65%	4.62%	4.63%	4.32%
Cat3	5.75%	5.75%	5.74%	5.44%
Photon Identification				
Cat0	1.1%	1.1%	1.09%	1.09%
Cat1	1.1%	1.09%	1.09%	1.11%
Cat2	1.1%	1.1%	1.09%	1.08%
Cat3	1.1%	1.1%	1.1%	1.09%
Electron Veto				
Cat0	1.02%	1.02%	1.02%	1.03%
Cat1	1.2%	1.2%	1.2%	1.2%
Cat2	1.2%	1.2%	1.2%	1.2%
Cat3	0.45%	0.45%	0.45%	0.45%
Polarization				
Cat0	15.36%	14.78%	14.84%	-
Cat1	15.6%	14.88%	14.87%	-
Cat2	15.01%	14.31%	14.4%	-
Cat3	15.39%	15.27%	15.39%	-

Table 4.8: A summary table of systematic uncertainties in the Z boson decaying in $\Upsilon(1S, 2S, 3S) + \gamma$, affecting the final yields of the MC samples.

Source	Uncertainty			
	Signal			Peaking Background
	$H \rightarrow \Upsilon(1S)\gamma$	$H \rightarrow \Upsilon(2S)\gamma$	$H \rightarrow \Upsilon(3S)\gamma$	$H \rightarrow \gamma\gamma^*$
Integrated luminosity			2.5%	
SM Higgs σ (scale)			+4.6% / -6.7%	
SM Higgs σ (PDF + α_s)			3.2%	
SM BR $H \rightarrow \gamma\gamma^*$		-		6.0%
Pileup Reweighting	0.61%	0.68%	0.56%	0.9%
Trigger	5.61%	5.47%	5.5%	6.12%
Muon Identification	4.39%	4.36%	4.34%	4.33%
Photon Identification	1.21%	1.22%	1.22%	1.2%
Electron Veto	1.04%	1.04%	1.04%	1.04%

Table 4.9: A summary table of systematic uncertainties in the Higgs boson decaying in $\Upsilon(1S, 2S, 3S) + \gamma$, affecting the final yields of the MC samples.

		$Z \rightarrow \Upsilon(nS) + \gamma$				$H \rightarrow \Upsilon(nS) + \gamma$
		Cat0	Cat1	Cat2	Cat3	Cat0
Mean - Scale						
$\Upsilon(1S)$	Muon Unc.	0.06%	0.05%	0.06%	0.11%	0.11%
	Photon Unc.	0.21%	0.13%	0.19%	0.26%	0.28%
	Total Unc.	0.22%	0.14%	0.2%	0.28%	0.3%
	Sigma - Resolution					
	Muon Unc.	1.12%	0.84%	1.55%	1.14%	2.62%
	Photon Unc.	2.14%	2.48%	1.95%	2.79%	4.27%
	Total Unc.	2.42%	2.61%	2.49%	3.01%	5.01%
$\Upsilon(2S)$	Mean - Scale					
	Muon Unc.	0.07%	0.05%	0.06%	0.13%	0.1%
	Photon Unc.	0.25%	0.11%	0.2%	0.19%	0.26%
	Total Unc.	0.26%	0.12%	0.21%	0.23%	0.28%
	Sigma - Resolution					
	Muon Unc.	1.21%	1.54%	2.65%	1.66%	1.02%
$\Upsilon(3S)$	Photon Unc.	1.85%	2.67%	3.56%	3.6%	6.6%
	Total Unc.	2.21%	3.08%	4.44%	3.97%	6.68%
	Mean - Scale					
	Muon Unc.	0.06%	0.06%	0.06%	0.09%	0.09%
	Photon Unc.	0.22%	0.14%	0.25%	0.17%	0.23%
	Total Unc.	0.23%	0.15%	0.26%	0.19%	0.25%
$\Upsilon(3S)$	Sigma - Resolution					
	Muon Unc.	1.78%	2.38%	2.1%	2.25%	3.46%
	Photon Unc.	2.51%	4.14%	2.23%	4.08%	5.48%
	Total Unc.	3.08%	4.77%	3.07%	4.66%	6.48%

Table 4.10: A summary table of systematic uncertainties in the Z (H) decaying in $\Upsilon(1S, 2S, 3S) + \gamma$, affecting the signal fits.

4.11 Modeling Cross checks

In order to test the applicability of the statistical (signal and background) modeling proposed in this study, a cross-check procedure is performed by generating a set of pseudo-experiments (toys datasets) based on the signal plus background model, for each decay channel ($H/Z \rightarrow \Upsilon(1S, 2S, 3S,) + \gamma$) with some signal injected.

The procedure consists of resampling from the signal plus background a number of events, including some extra (injected signal). The amount of injected signal is controlled by the μ_{true} variable, where $\mu_{true} = X$ means inject X times the expected signal.

Once generated, the toy dataset is refitted to the signal plus background model and the signal strength (μ_{fit}) and its error σ_{fit} are extracted. This procedure is repeated 10000 times and only for the inclusive category. Figures 4.66, 4.65, 4.68 and 4.67 show examples of those fits for the Higgs and Z decay.

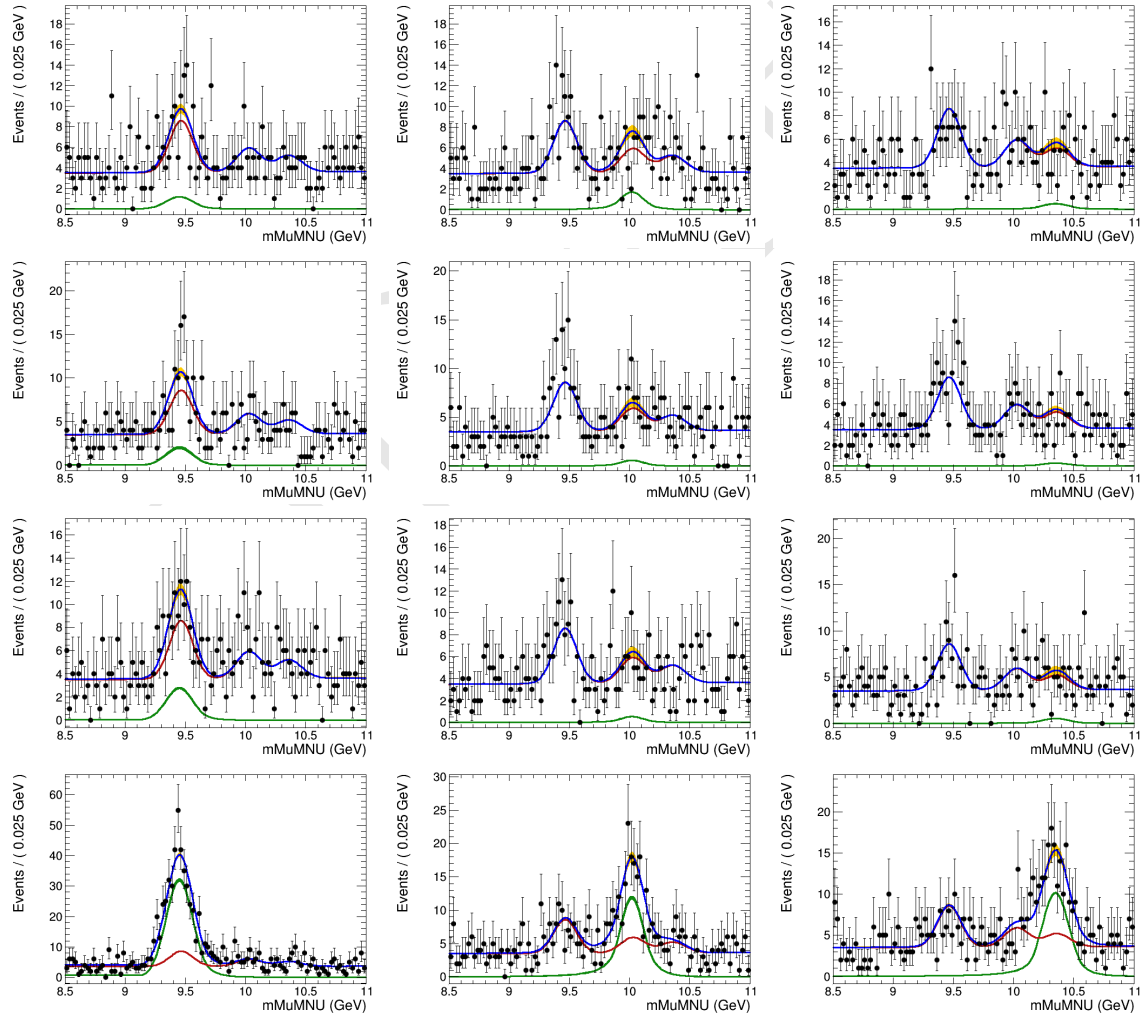


Figure 4.65: Examples of the toy datasets fit ($M_{\mu\mu}$), for the Z decay analysis, after the toy dataset refit, for 1S, 2S and 3S (left to right), with μ_{true} equals to 20, 50, 100, 1000 (top to bottom). The red lines corresponds to the background model (B), the green lines to signal model (S), the blue lines to the total (S+B) and the dots is the toy dataset.

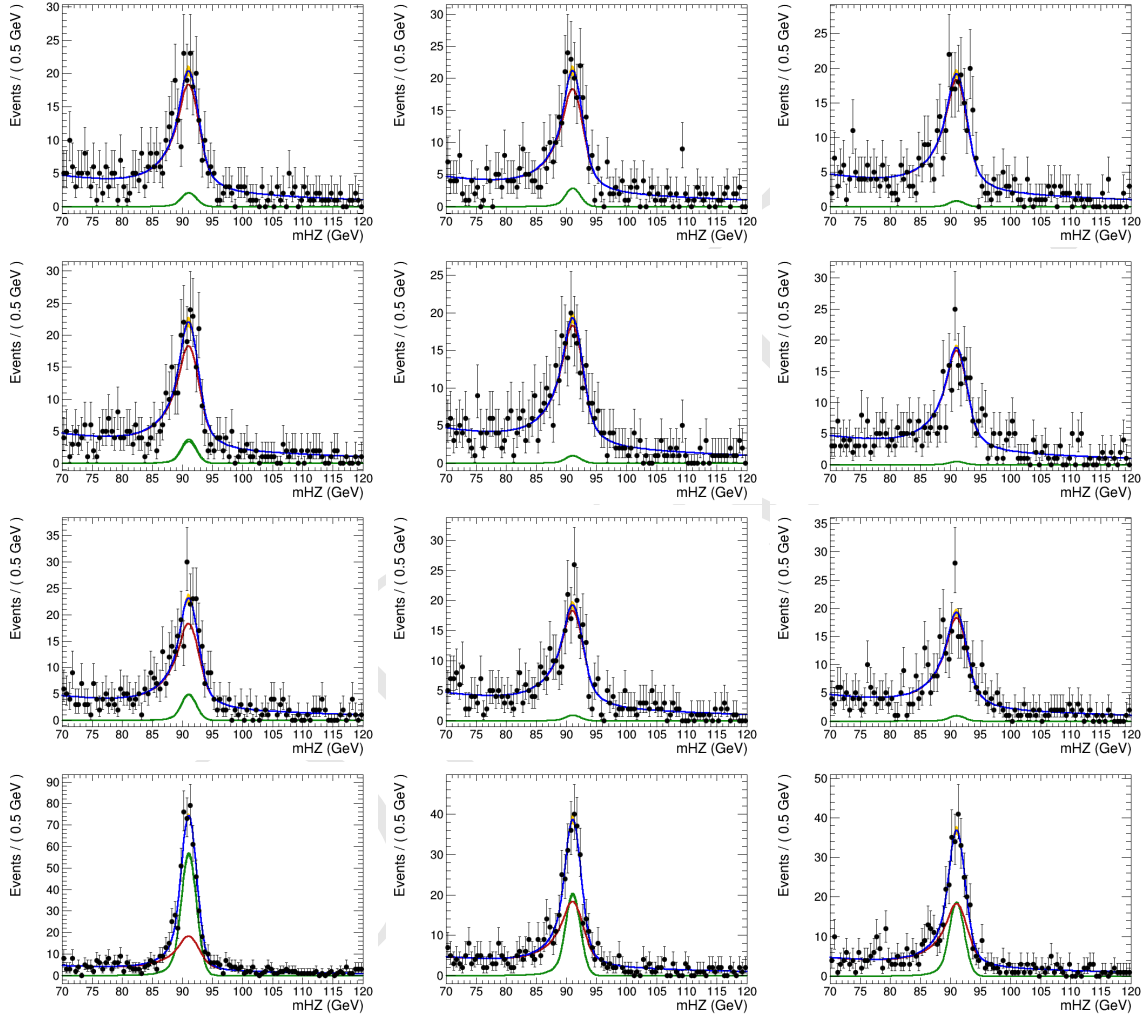


Figure 4.66: Examples of the toy datasets fit ($M_{\mu\mu\gamma}$), for the Z decay analysis, after the toy dataset refit, for 1S, 2S and 3S (left to right), with μ_{true} equals to 20, 50, 100, 1000 (top to bottom). The red lines corresponds to the background model (B), the green lines to signal model (S), the blue lines to the total (S+B) and the dots is the toy dataset.

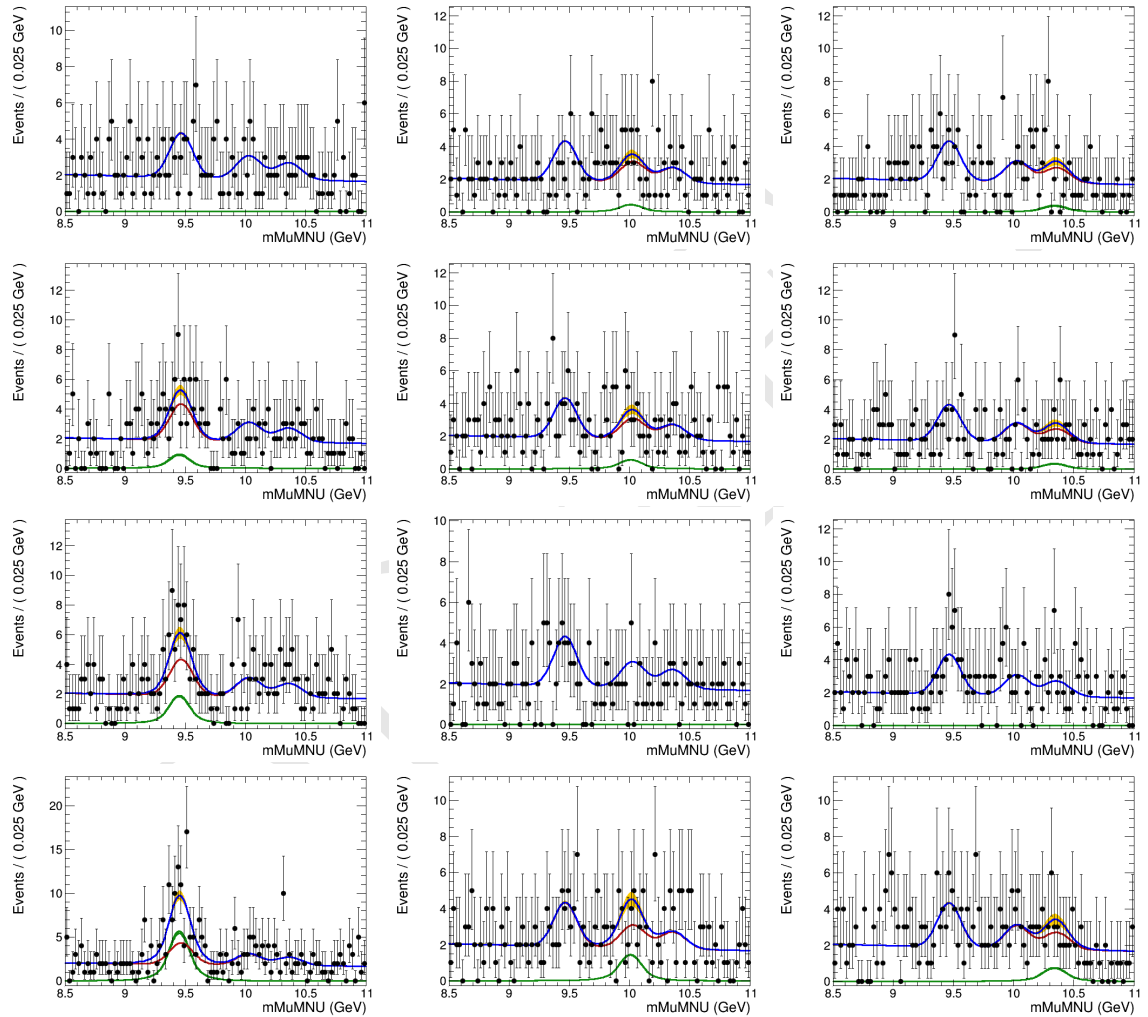


Figure 4.67: Examples of the toy datasets fit ($M_{\mu\mu}$), for the Higgs decay analysis, after the toy dataset refit, for 1S, 2S and 3S (left to right), with μ_{true} equals to 100000, 200000, 300000, 1000000 (top to bottom). The red lines corresponds to the background model (B), the green lines to signal model (S), the blue lines to the total (S+B) and the dots is the toy dataset.

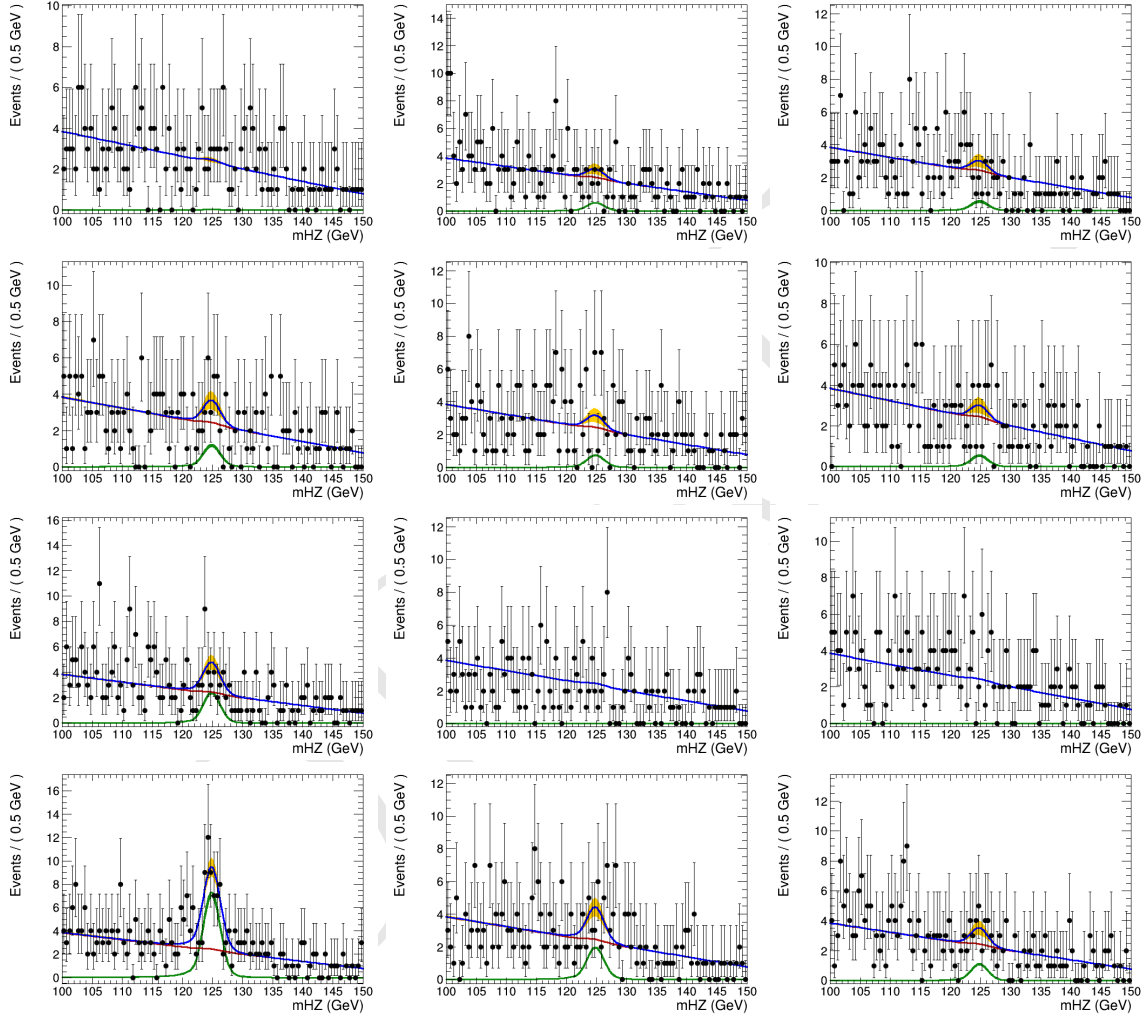


Figure 4.68: Examples of the toy datasets fit ($M_{\mu\mu\gamma}$), for the Higgs decay analysis, after the toy dataset refit, for 1S, 2S and 3S (left to right), with μ_{true} equals to 100000, 200000, 300000, 1000000 (top to bottom). The red lines corresponds to the background model (B), the green lines to signal model (S), the blue lines to the total (S+B) and the dots is the toy dataset.

744 It is expected that the pulls distribution for the fitted signal strength ($\frac{\mu_{fit} - \mu_{true}}{\sigma_{fit}}$) should follow
 745 a Gaussian distribution centered in 0 and with σ around 1. Figures 4.69 and 4.70 present those
 746 pulls distributions for the Z and Higgs decays, respectively.

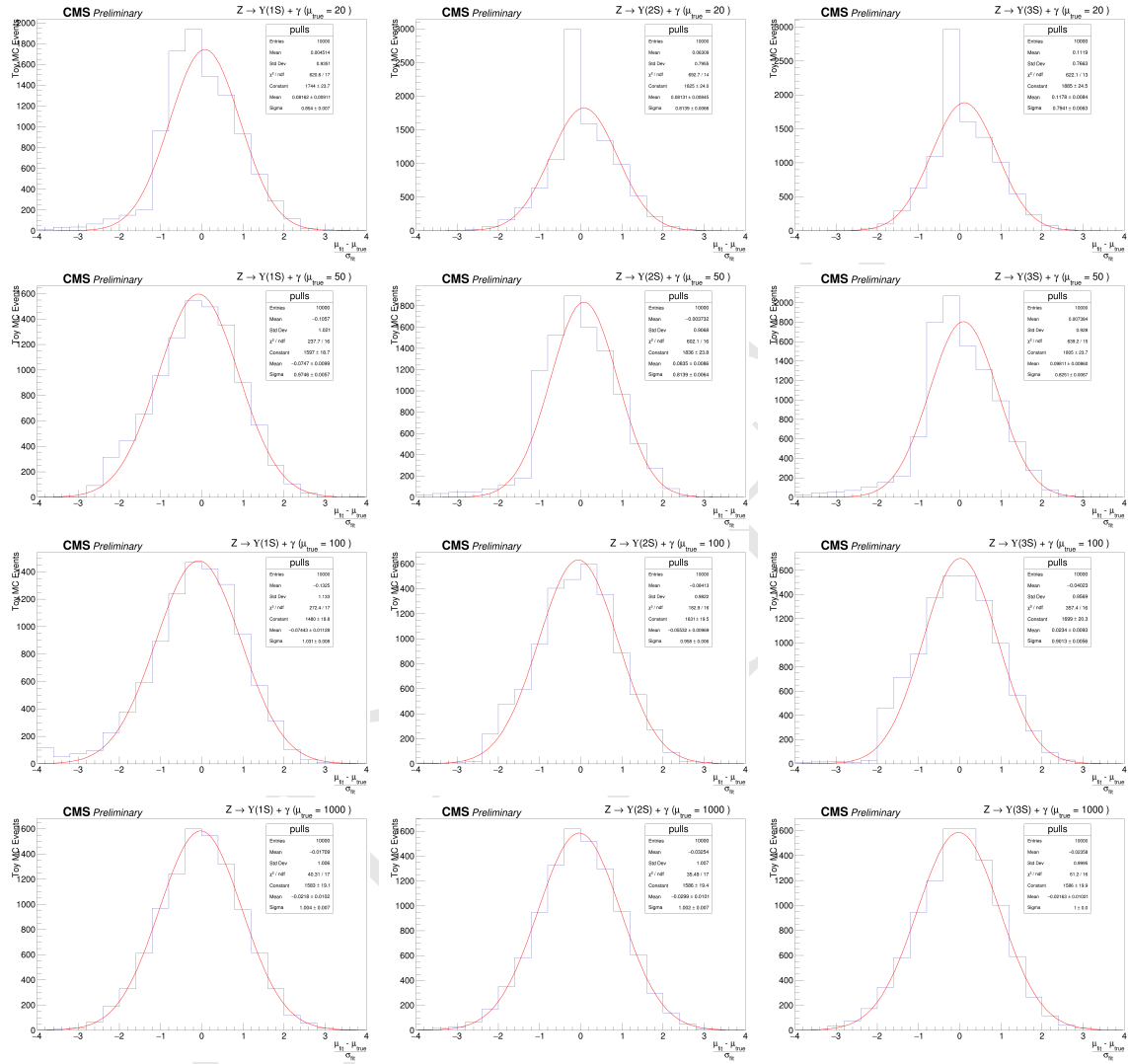


Figure 4.69: Distribution of pulls ($\frac{\mu_{fit} - \mu_{true}}{\sigma_{fit}}$), for the Z decay analysis, after the toy dataset refit, for 1S, 2S and 3S (left to right), with μ_{true} equals to 20, 50, 100, 1000 (top to bottom).

747 As a general conclusion on this cross check, as long as the toy MC generation is able to inject
 748 enough signal to be fit, the final modeling of this analysis is able to recover a Gaussian pulls
 749 distribution. This, of course, depends on the Y state to be considered. For the Z decay, between
 750 $\mu_{true} = 50$ and $\mu_{true} = 100$ (around a hundred of events passing full selection), while for the Higgs
 751 decay, it is needed only a few events after full selection, even though it means hundreds of thousands
 752 times the expected signal, since the very small cross sections for the decay, as shown in Table 4.1.

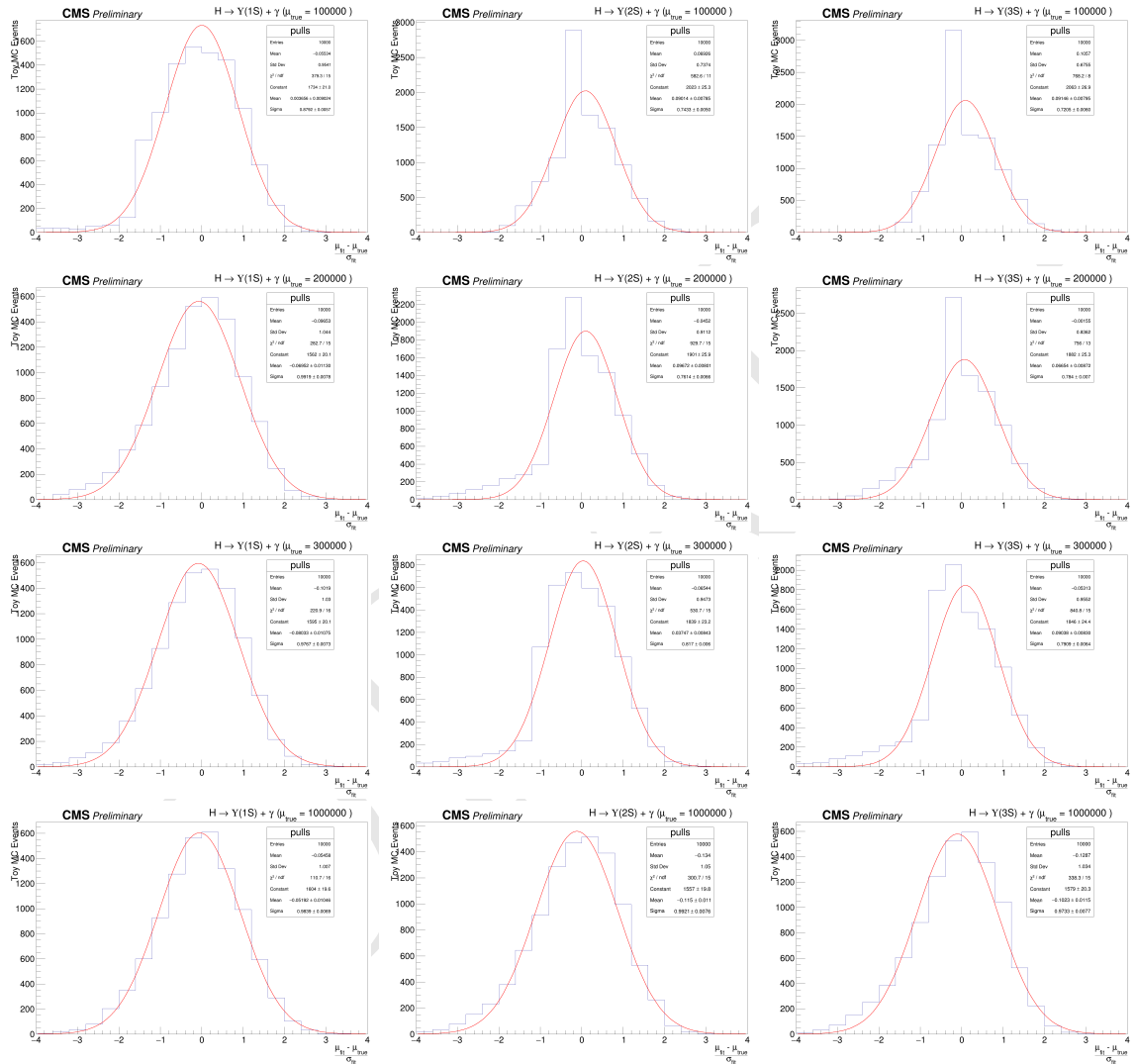


Figure 4.70: Distribution of pulls ($\frac{\mu_{fit} - \mu_{true}}{\sigma_{fit}}$), for the Higgs decay analysis, after the toy dataset refit, for 1S, 2S and 3S (left to right), with μ_{true} equals to 100000, 200000, 300000, 1000000 (top to bottom).

753 5 Results and conclusion

754 A two-dimensional (2D) unbinned maximum-likelihood fit to the $m_{\mu^+\mu^-\gamma}$ and $m_{\mu^+\mu^-}$ distri-
 755 butions was used to compare the data with background and signal predictions. Search has been
 756 performed for a SM Higgs and Z boson decaying into a $\Upsilon(1S, 2S, 3S)\gamma$, with $\Upsilon(1S, 2S, 3S)$ subse-
 757 quently decaying into $\mu^+\mu^-$ using data obtained from 35.9 fb^{-1} of pp collisions at $\sqrt{s} = 13 \text{ TeV}$.

758 Since no excess has been observed above the background, the CL_s formalism is applied, in order
 759 to establish an upper limit in the branching fractions for each channel.

760 5.1 The CL_s formalism for upper limits setting at CMS

761 The CL_s formalism [69] consist in a modified frequentist approach to obtain an upper limit for
 762 a certain parameter of a model, with respect to the data. It is based on the profile-likelihood-ratio
 763 test statistic [70] and asymptotic approximations [71]. It is a standard upper limit setting procedure
 764 for the LHC experiments [72].

765 When searching for non-observed phenomena, it is often usual to derive the results as a function
 766 of the signal strength modifier μ , which is a free parameter of the full model (signal + background).
 767 It can be define such as, the expectation value for the number of events in a bin ¹ is:

$$E[n] = \mu s + b, \quad (5.1)$$

768 where, s and b are the expected number of signal e background events, respectively.

769 The Neyman–Pearson lemma [70] states the the optimal

770 **Terminar a descrição do CL_s formalism.**

771 5.2 Branching fraction upper limits

772 The result are summarized on table 5.1.

773 The observed(expected) exclusion limit at 95% confidence level on the $\mathcal{B}(Z \rightarrow \Upsilon(1S, 2S, 3S)\gamma) =$
 774 $2.9, 2.7, 1.4$ ($1.6^{+0.8}_{-0.5}, 2.0^{+1.0}_{-0.6}, 1.8^{+1.0}_{-0.6}$) $\times 10^{-6}$, and on the $\mathcal{B}(H \rightarrow \Upsilon(1S, 2S, 3S)\gamma) = 6.9, 7.4, 5.8$
 775 ($7.3^{+4.0}_{-2.4}, 8.1^{+4.6}_{-2.8}, 6.8^{+3.9}_{-2.3}$) $\times 10^{-4}$.

776 As stated before, this analysis was done, for the Z decay, taking into account a mutually exclusive
 777 categorization of events, based on the reconstructed photon properties (η_{SC} and R9 value), as
 778 described in section 4.7.

779 At table 5.2 we present the results obtained when there is no categorization of events (Inclusive
 780 category).

¹A set of common analysis criteria.

95% C.L. Upper Limit			
	$\mathcal{B}(Z \rightarrow \Upsilon\gamma) [\times 10^{-6}]$		
	$\Upsilon(1S)$	$\Upsilon(2S)$	$\Upsilon(3S)$
Expected	$1.6^{+0.8}_{-0.5}$	$2.0^{+1.0}_{-0.6}$	$1.8^{+1.0}_{-0.6}$
Observed	2.9	2.7	1.4
SM Prediction [$\times 10^{-8}$]	4.8	2.4	1.9
	$\mathcal{B}(H \rightarrow \Upsilon\gamma) [\times 10^{-4}]$		
	$\Upsilon(1S)$	$\Upsilon(2S)$	$\Upsilon(3S)$
Expected	$7.3^{+4.0}_{-2.4}$	$8.1^{+4.6}_{-2.8}$	$6.8^{+3.9}_{-2.3}$
Observed	6.9	7.4	5.8
SM Prediction [$\times 10^{-9}$]	5.2	1.4	0.9

Table 5.1: Summary table for the limits on branching ratio of $Z \rightarrow \Upsilon(1S, 2S, 3S)\gamma$ and $H \rightarrow \Upsilon(1S, 2S, 3S)\gamma$ decays.

95% C.L. Upper Limit - $\mathcal{B}(Z \rightarrow \Upsilon\gamma) [\times 10^{-6}]$			
	without categorization		
	$\Upsilon(1S)$	$\Upsilon(2S)$	$\Upsilon(3S)$
Expected	$1.7^{+0.9}_{-0.5}$	$2.1^{+1.1}_{-0.7}$	$1.9^{+1.0}_{-0.6}$
Observed	2.6	2.3	1.2
	with categorization		
	$\Upsilon(1S)$	$\Upsilon(2S)$	$\Upsilon(3S)$
Expected	$1.6^{+0.8}_{-0.5}$	$2.0^{+1.0}_{-0.6}$	$1.8^{+1.0}_{-0.6}$
Observed	2.9	2.7	1.4

Table 5.2: Summary table for the limits on branching ratio of $Z \rightarrow \Upsilon(1S, 2S, 3S)\gamma$, for the two possible categorization scenarios.

781 It is worth to remember that the categorization takes places only for the Z decay. For the Higgs
 782 decay, no categorization is imposed.

783 By taking, or not, into account any categorization, the numbers presented in both tables (5.1
 784 and 5.2), are compatible within themselves and with the results published by the ATLAS collabora-
 785 ration [73].

786 6 CMS Resistive Plate Chambers - RPC

787 In the course of this PhD study, there were a lot of opportunities to work for the RPC project, in
788 the context of the CMS Collaboration. The main activities consists of shifts for the RPC operation
789 and data certification, upgrade and maintenance of the online software, R&D activities for the RPC
790 upgrade and detector maintenance during the LHC Long Shutdown 2 (2019 to 2020).

791 In this chapter, it is presented a summary of the Resistive Plate Chamber technology and the
792 contributions to the RPC project at CMS.

793 6.1 Resistive Plate Chambers

794 The seminal paper on the Resistive Plate Chamber (RPC) technology was presented by R.
795 Santonico and R. Cardarelli, in which they described a "dc operated particle detector (...) whose
796 constituent elements are two parallel electrode Bakelite plates between" [74]. The key idea behind
797 the RPC, with respect to other similar gaseous detectors, is the use of two resistive plates as anode
798 an cathode, which makes possible to have a small localized region of dead time, achieving very good
799 time resolution.

800 The working principle for RPCs relies on the idea that a ionizing particle crossing the detector,
801 tend to interact with the gas gap between the two plates and form a ionizing cascade process, in
802 which the produced charged particle are driven by the strong uniform electrical field produced
803 by the two plates.

804 The gas mixture is a key component of a RPC. Even though the first RPCs were produced
805 with a mixture of argon and butane, nowadays RPCs use a mixture of gases that would enhance an
806 ionization caused by the incident particle and quench secondary (background) effects.

807 Another feature of the RPCs is its construction simplicity and low cost. This allow the use RPC
808 to cover larger at a reasonable cost.

809 A extensive review of the RPC technology and its application can be found in [75].

810 **DESCREVER A TECNOLOGIA DAS RPCS**

811 **DESCREVER OS PRINCÍPOS DE OPERACAO - TDR**

812 6.2 CMS Resistive Plate Chambers

813 At CMS, the Resistive Plate Chamber are installed in both the barrel and endcap region, forming
814 a redundant system with the DT (barrel) and CSC (endcap). As described in the CMS Muon
815 Technical Design Report (Muon-TDR) [76], the RPC are composed of 423 endcap chambers and
816 XXXXXX **QUAL O NUMERO DE BARREL CHAMBERS????** barrel chambers.

817 Each chamber consists of two gas gaps (double gap), 2 mm tick each, made of Bakelite (phenolic
 818 resin) with bulk resistivity of $10^{10} - 10^{11} \Omega m$. The choice of the bulk resistivity of the electrode has
 819 high impact on the rate capability of the detector.

820 Each gap has its external surface is coated with a thin layer of graphite paint, which acts as
 821 conductive material, distributing the applied high-voltage (HV). On top of the graphite a PET
 822 film is used for isolation. A sheet of copper strips is sandwiched between the gaps. Everything is
 823 wrapped in aluminum case.

824 The double gap configuration increases the efficiency of the chamber, since the signal is picked
 825 up from the OR combination of the two gaps. A chamber with only one gap working, loses around
 826 15% of efficiency, even though, this can be recovered by increasing the HV applied during operation
 827 mode (working point - WP).

828 A characteristic that differentiate the CMS RPC from previous RPC application in HEP is
 829 the operation mode. A RPC at CMS, operates in avalanche mode, while previous experiments used
 830 the streamer mode. Both modes are related to the applied HV, in commitment with the strength of
 831 the generated signal, and are capable of generate a well localized signal, which can be picked up by
 832 the readout electronics, but the avalanche mode offer a higher rate capability around 1 kHz/cm^2 ,
 833 while the streamer mode goes up to 100 Hz/cm^2 . The high rate capability is a key factor in order
 834 to cope with requirements of the LHC luminosity, specially in the high background regions.

835 Besides the rate capability, the key factors that driven the CMS RPC design were: high effi-
 836 ciency ($> 95\%$), low cluster size (> 2) for better spatial resolution (this reflects in the momentum
 837 resolution) and good timing in order to do the readout of the signal within the 25 ns of a LHC
 838 bunch cross (BX) and provide it to the CMS trigger system. These requirements have implications
 839 in the choice of material, dimensions, electronics and gas mixture.

840 In the barrel, along the radial direction, there are 4 muon layers (called stations), MB1 to MB4.
 841 MB1 and MB2 is composed of a DT chamber sandwiched between two RPC chambers (RB1 and
 842 RB2) with rectangular shape. The stations MB3 and MB4 have only one RPC (RB3 and RB4) are
 843 composed by two RPC chambers (named - and + chambers with the increase of ϕ) attached to one
 844 DT chamber, except in sector 9 and 11, where there is only one RPC. RE4, sector 10 is a special
 845 case, since it is composed of four chambers (-, -, + and ++). These stations are replicated along
 846 the z direction in five different wheels of the CMS (W-2, W-1, W0, W+1 and W+2) and in twelve
 847 azimuthally distributed sectors (S1 to S12). Figure 6.1 show the different barrel stations and wheel.

848 **DAR AS DIMENSOES - BARREL**

849 In the endcap, the RPC chambers have a trapezoidal shape and are distributed in four disks (or
 850 stations) each side (RE ± 4 , RE ± 3 , RE ± 2 , RE ± 1), each one with 72 chambers. CMS split up its
 851 disks in 3 rings, along the radial direction, and 36 sector in the azimuthal angle. RPCs are present
 852 in the two outer rings (R2 and R3), in all 36 sectors. The RE ± 4 are special cases, since these
 853 chambers were installed only in 2014, a design choice was made the mechanically attached R2 and
 854 R3 chambers, each sector, in what is called, a super-module. Figure 6.2 show the different endcap
 855 disks.

856 **DAR AS DIMENSOES - ENDCAP**

857 The length of the strips is chosen, for both barrel and endcap, in such a way to control the area
 858 of each strip, in order to reduce the fake muons, due to random coincidence. This has to do with

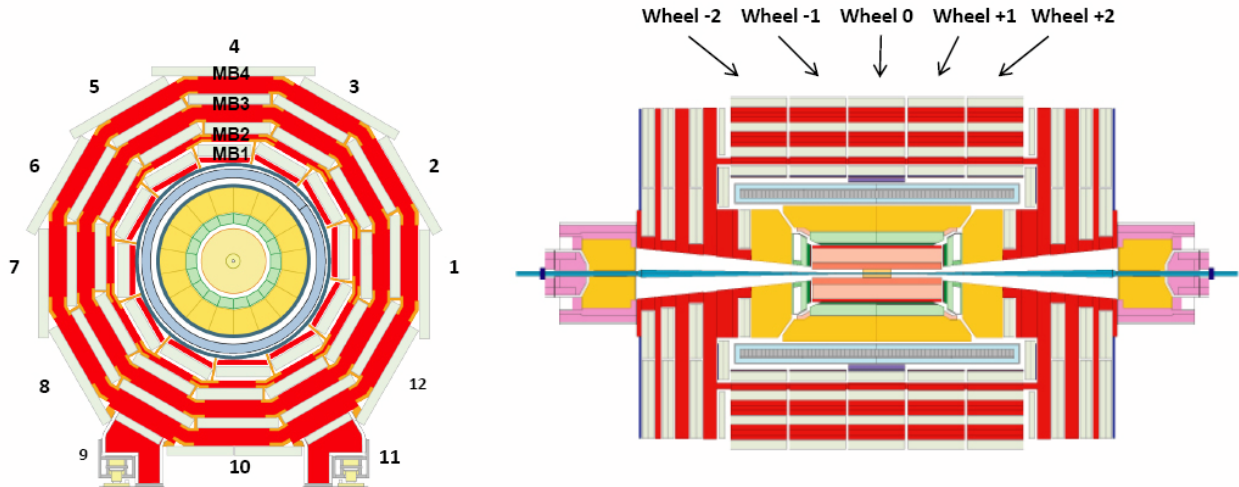


Figure 6.1: R- ϕ (left) and R-Z (right) projections of the barrel Muon System.

859 the time-of-flight and signal propagation along the strip. In the barrel, each chamber readout is
 860 divided in two regions (rolls), called forward and backward (along increasing $|\eta|$) ¹. In the endcap,
 861 the strips are divided in 3 regions, called partitions A, B and C (from inside the detector to outside).

862 The gas mixture used in the CMS RPCs is composed by C₂H₂F₄ (Freon R-134a, tetrafluoroethane), C₄H₁₀ (isobutane), SF₆ (sulphur hexafluoride) (95.2 : 4.5 : 0.3 ratio) and with controlled
 863 humidity of 40% at 20-22 °C. The Freon is used to enhance the ionization and charge multiplication
 864 that characterizes the avalanche, while the isobutane is introduced for quenching proposes, in order
 865 to reduce the secondary ionizations that could lead to formation of streamers and the SF₆ is used
 866 to reduce the electron background. The choice of Freon over other gases, i.e. argon-based and
 867 helium-based, was motivated by previous studies [77, 78].

869 Since its R&D, the RPC have shown good performance over aging. This is even historical over
 870 previous RPC experiments **ADICIONAR REFERÊNCIAS 5.14, 5.15 E 5.16 DO MUON**
 871 **TDR**. Even the most recent studies of aging, taking into account future LHC conditions (High-
 872 Luminosity LHC - HL-LHC) plus a safety margin of 3 times the expected background (600 Hz/cm^2)
 873 have shown good aging hardness [79].

874 6.2.1 Electronics and Readout

875 **FEBs**

876 **LINK SYSTEM**

877 6.2.2 Performance

878 **PERFORMANCE NO RUN2**

879 Below it is described the main contributions given to the CMS RPC project.

¹Some chamber are divided in three rolls, forward, middle and backward, for trigger propose.

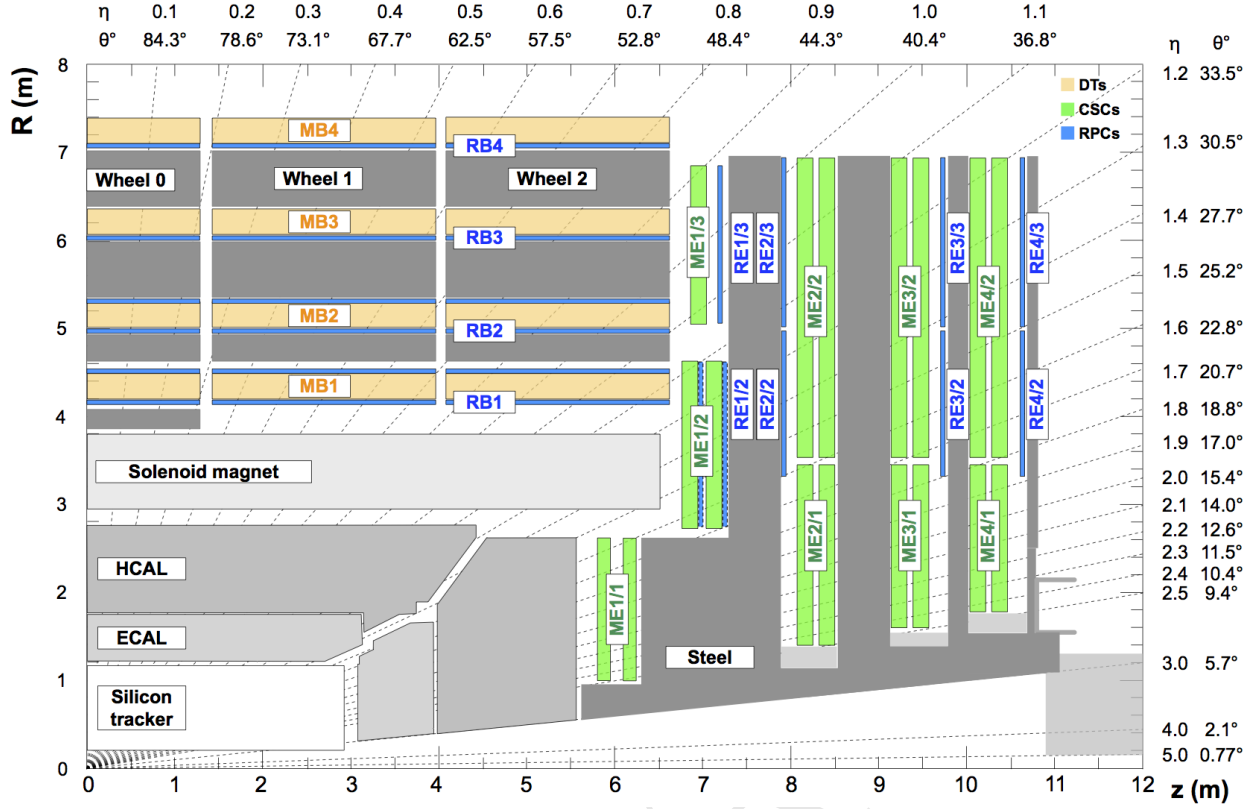


Figure 6.2: R-Z projections of the endcap Muon System (positive Z side). This is the same configuration for the 36 ϕ sectors.

6.3 RPC Operation - Shifts and Data Certification

The first activities done for the CMS RPC project were shifts for data certification of data taken. This certification is done by specialized people for different CMS subsystems and physics objects groups².

This certification is done in order to ensure the quality of the date recorded based on the well functionality of each system during the data taking and the reconstruction of the physics objects in the expected matter. A certain collection of data (run) is said certificate when all subsystems and object experts agrees on this.

Figure 6.3 shows, as an example of the luminosity delivered by the LHC, recorded one by CMS and the certified (validated), from the 22nd of April, 2016 to the 27th of October, 2016. Only certified data is available for physics analysis.

Shifts are a continuous weekly activity (specially during the data taking period), performed in a weekly basis, in order to ensure the availability of certified data, as soon as possible.

²Groups of reconstruction and performance experts for different high-level reconstructed objects from CMS, i.e. muons, taus, jets/MET, electrons/photons

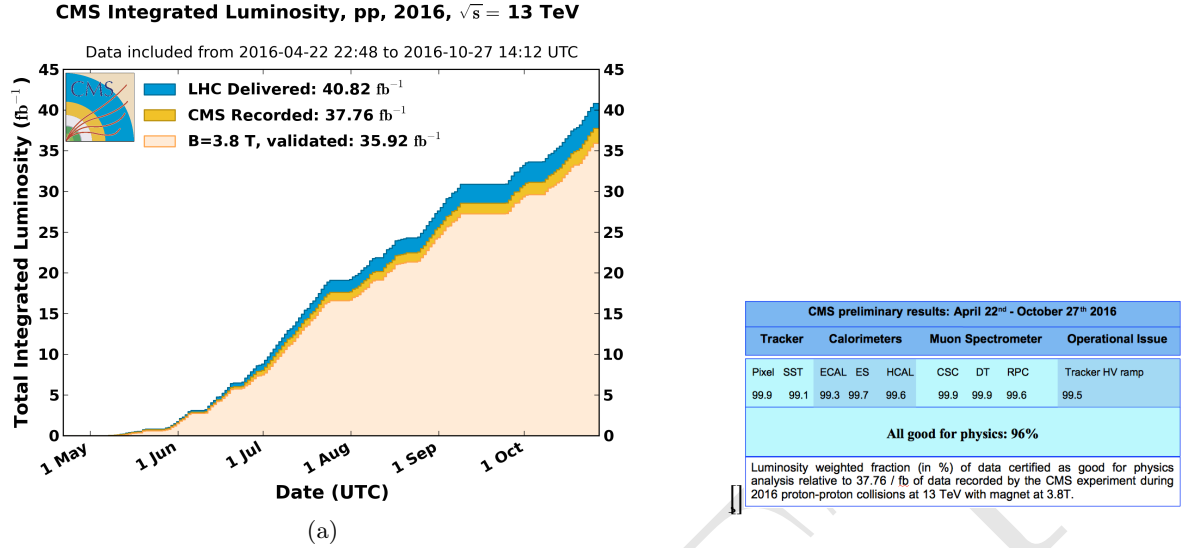


Figure 6.3: (a) Luminosity delivered by the LHC, recorded one by CMS and the certified (validated), from the 22nd of April, 2016 to the 27th of October, 2016. (b) Efficiency of the certification process for each subsystem, from the 22nd of April, 2016 to the 27th of October, 2016. Total CMS efficiency is above 90%. [80]

893 6.4 RPC Online Software

894 On what concerns the Online Software (OS) of the CMS RPC system, the main contribution
 895 given was the upgrade of the Trigger Supervisor libraries.

896 The Trigger Supervisor is a web-based software, which run over the xDAQ backend and provides,
 897 through a mudules organized in a tree system, called cells, a standard interface for the operation and
 898 monitoring of different system at CMS. In principle only systems which contribute directly to the
 899 L1 trigger should have a Trigger Supervisor implementation. This was the case for the RPC during
 900 the Run1. Since Run2, RPC contributes to the trigger indirectly, by providing data to the muon
 901 processors (CPPF, OMTF and TwinMux). The Trigger Supervisor implementation is a legacy from
 902 that period.

903 Each subsystem is responsible for its own implementation of the Trigger Supervisor, based on the
 904 functionalities that it wants to have (requirements). The xDAQ [81] is a middleware, developed by
 905 CERN and widely used at CMS, as a tool for control and monitoring of data acquisition system in
 906 a distributed environment. It is capable of provideing a software layer for direct access of hardware
 907 functionalities and monitoring.

908 The upgrade made (figure 6.4), consists in upgrade the higher level of the RPC online software.
 909 In summary, up to 2017, the online software, was using Scientific Linux 6 as operational system,
 910 which executed xDAQ 12, in turn, servers as backend for Trigger Supervisor 2. A upgrade of
 911 the operational system to Centos 7, demanded the upgrade to xDAQ 14. On top of that, Trigger
 912 Supervisor 2 would not work and had to be updated to Trigger Supervisor 5 in order to be functional
 913 in 2018.

914 Between versions 2 and 5 of Trigger Supervisor, part of the source-code had to be reworked,
 915 keep the majority of the code structures. Most of the changes were made in the front-end of the
 916 system. The standard JavaScript library Dojo [82], used in version2, was deprecated in favor of

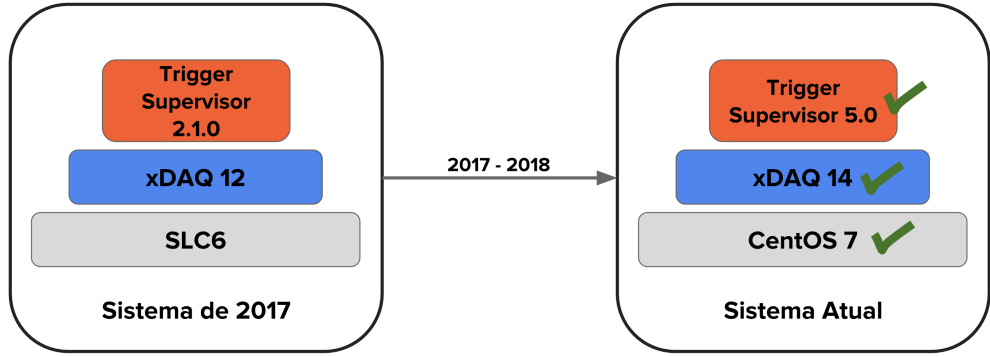


Figure 6.4: Upgrade of the RPC online software.

917 Google's Polymer[83]. The main reason for this change was to isolate C++ code from HTML, which
 918 was impossible with Dojo. This implied to rewrite all the screen of the RPC Trigger Supervisor
 919 implementation, as in figure 6.5.

920 The upgrade was done in time to ensure the control and operation of the RPC for 2018 data
 921 taking.

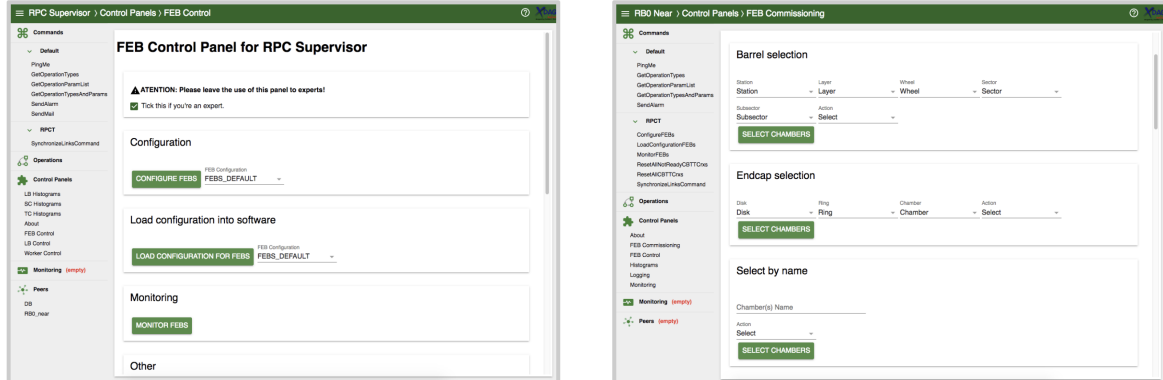


Figure 6.5: Example of the updated screens, using Trigger Supervisor 5.

922 6.5 iRPC R&D

923 For the next 4 year of CMS activities it is foreseen the upgrade of the the Muon Systems [76].
 924 These upgrades are planed in order to extend the pseudorapidity coverage (η) and to guarantee the
 925 operation conditions of the present system in the HL-LHC (High Luminosity LHC) era. The RPC
 926 (Resistive Plate Chambers) [76] subsystem, it will have maintenance of the present chambers and
 927 installation of new chambers in the region of $|\eta| < 1,8$ para $|\eta| < 2,4$ [84]. These new chambers
 928 (iRPC) will be added in the most internal part of the muon spectrometer, RE3/1 e RE4/1, as in
 929 Figure 6.6.

930 Even thought this region is covered by the CSC detectors CSC (Cathode Strip Chambers), there
 931 are some loss of efficiency due the the system geometry. The installation of additional chambers will
 932 mitigate this problem and potentially increase the global efficiency of the muon system. The new

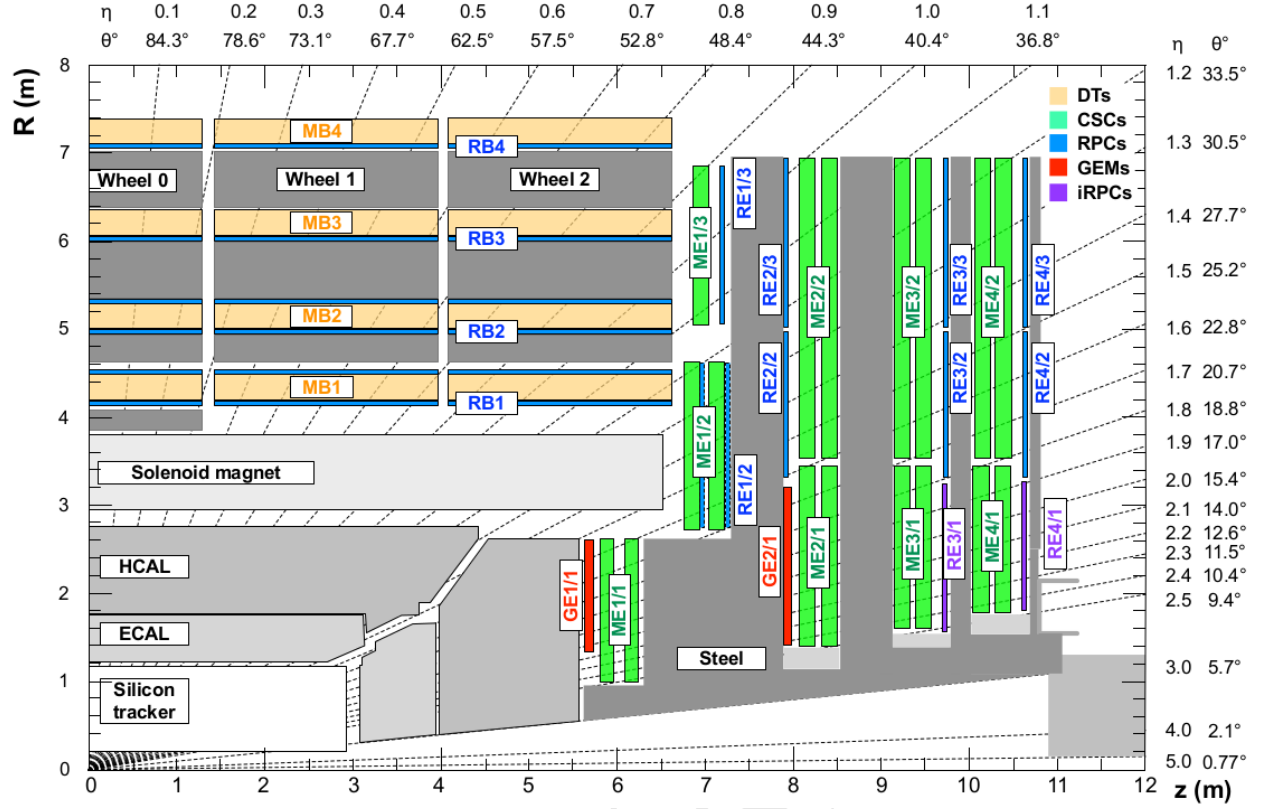


Figure 6.6: η projection of the Muon System subdetectors. In purple, is labeled the iRPCs to be installed during the CMS upgrade.

chamber, called iRPC (*improved RPC*), will be different them the present one. For a luminosity of $5 \times 10^{34} \text{ cm}^{-2} \text{s}^{-1}$ the neutrons, photons, electrons and positrons background in the high $|\eta|$ region is expected to be around 700 Hz/cm^2 (for the chambers in RE3-4/1). Applying a safety factor of 3, the new chambers should support up to 2 Hz/cm^2 of gamma radiation and still keep more than 95% of efficiency. Studies indicate, so far, that the use of High Pressure Laminates (HPL) for the double gap chambers is the most suitable choice. In order to reduce the aging and increase the rate capability, the electrodes and the gap size should be reduced in comparison with the present system.

One of the challenges for the R&D of the iRPC chambers is measuring their performance in a high radiation environment, as the one for HL-LHC. For this, the CMS RPC project uses the Gamma Irradiation Facility (GIF++) [85], at CERN. The GIF++ is located at the H4 beam line in EHN1 providing high energy charged particle beams (mainly muon beam with momentum up to 100 GeV/c), combined with a 14 TBq 137-Cesium source. In the GIFF++ it is possible to achieve the HL-LHC total dose in a much reasonable amount of time. With the shutdown of LHC, the muon beam source is also off and will stay like this for 3 years. This means that the only muon sources for studies in GIF++ are cosmic muons.

In order to create a trigger system for iRPC R&D, the usual procedure is to use scintillators, on the top and on the bottom of the chamber. This is effective, but in a high gamma radiation environment, scintillators can be very sensitive which could lead to an undesirable amount of fake

triggers which can degrade the measurements. Also, if one wants to covers a large area with scintillators, this can be expensive and they will not provide any means of tracking to measuring not only the global, but also the local chamber performance.

To provide a solution, the CMS RPC got in agreement with the LHCb [86] Muon Project to use their Multiwire Proportional Chambers (MWPC) [87], which were removed from LHCb, to be replaced by new chambers, and use them as trigger and/or tracking system at GIF++. This chambers, by design, have relatively low gamma sensitivity, already have some 1-dimensional resolution ($O(\text{cm})$) and, the biggest advantage, with respect to any other gaseous particle detector option: LHCb has hundreds of vacant chambers. Any other detector would have to be build.

Not going in details of the MWPC technology nor the LHCb chamber construction [88], these chambers have a total active area of $968 \times 200 \text{ mm}^2$ divided 2 layers (top and bottom) of 24 wire pads ($40 \times 200 \text{ mm}^2$) composed of around 25 wires/channel, grouped by construction. Each chamber is equipped with 3 FEBs (Front-End Boards) with 16 pads each.

A channel is a logical combination of a top layer (pads) and a bottom layer readout. These readouts can be combined in AND or OR logics. One can have 8 channels per FEB, each channel being a logical combination of top and bottom pads. In this mode they are called AND2 and OR2. It is also possible to have the FEB configured in a 2 channels mode, each one corresponding to one sixth of the total readout pads. In this mode, all the pads can be combined in OR (called OR8) or they can be AND'ed in top and bottom pads and then group in OR (called OR4AND2). Figures 6.7 and 6.8 presents a logical diagram for each readout mode.

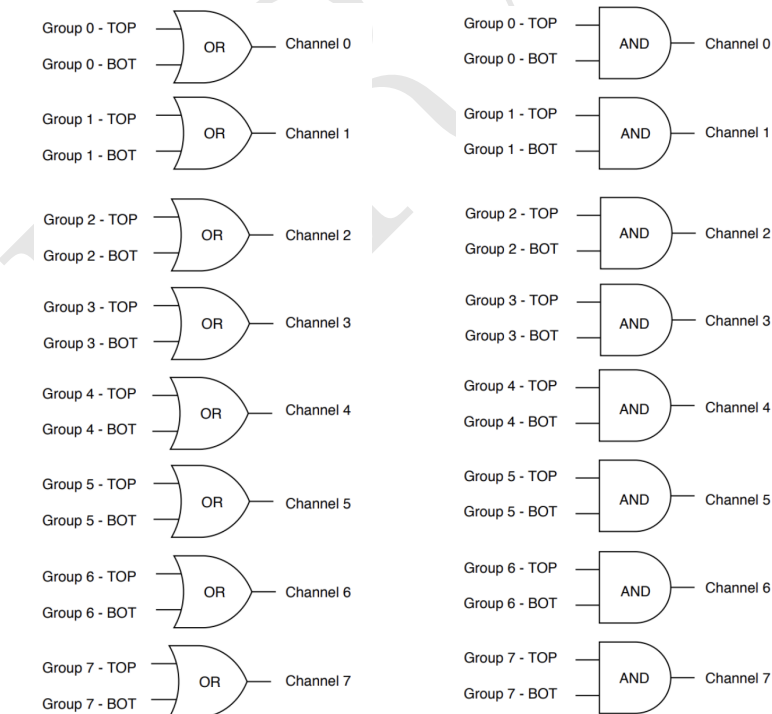


Figure 6.7: FEB configured 8 channels modes. Group should be understood as wire pad. Left: Logical diagram for OR2. Right: Logical diagram for AND2.

The nominal gas mixture for these chambers is Ar/CO₂/CF₄ (40:55:5). For a matter of simplicity, it was used an already available similar gas line in the same building, used by CMS CSC

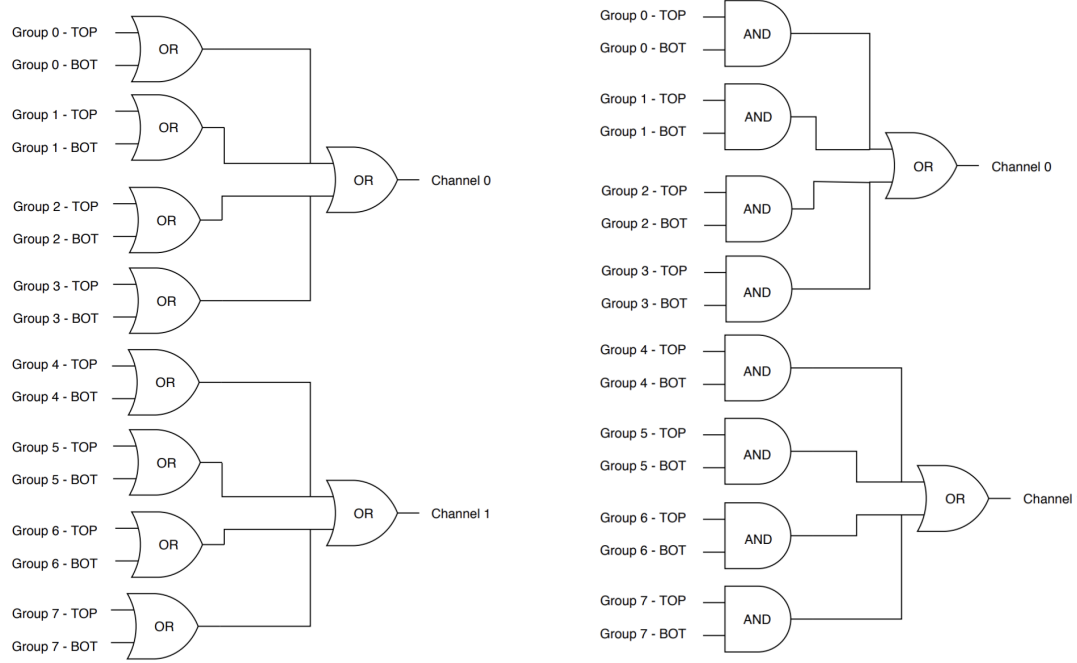


Figure 6.8: FEB configured 2 channels modes. Left: Logical diagram for OR8. Group should be understood as wire pad. Right: Logical diagram for OR4AND2.

974 (Cathode Strip Chamber) [76], which has a similar composition (40:50:10). Optimal conditions are
975 obtained with 2 to 4 liters/hour of gas flux and 2.65 kV of applied voltage.

976 Figure 6.9 shows the setup that was prepared for commissioning of this chambers. It was
977 mounted two chambers on top of another (chambers A and B) above an RPC R&D chamber and
978 two other chambers on the bottom (chambers C and D). These four MWPC will be used as telescope
979 for the RPC chamber. All the services were mounted in rack, as in Figure 6.9. This includes power
980 supply (low voltage and high voltage), distribution panel, VME crate and boards for FEB control,
981 computer for control (high voltage, and FEB control) and NIM crate and boards for LVDS to NIM
982 signal conversion, logics and counting.

983 Due to the short amount of time available for the commissioning, only two measurements mea-
984 surements were made with these chambers. They were meant to be a proof of concept for future
985 activities.

986 The first measurement was to measure the coincidence rate of two chambers as a function of
987 the distance between the two top planes (Figure 6.10). This measurements were done with nominal
988 working point, with one FEB configured in 2 channels mode with 7 pC threshold, in (160 mm x
989 160 mm) area per chamber. One can observe that, if we go for a telescope trigger in the order of
990 1 meter of separation between the chamber, the logical combination chosen has negligible effect in
991 the coincidence rate. Also, the fits can be used to estimate the rate in a configuration with chamber
992 on the roof and under the floor. This could be the case of a universal trigger, to be mounted in
993 GIF++ with these chamber.

994 The second measurement consist on evaluate the impact of γ background by placing a small
995 Cs-137 source on top of the chamber A (Figure 6.11). For this measurement, the distance between
996 top planes of each pair of chamber (A to B and C to D) is 65 mm, while the distance between the

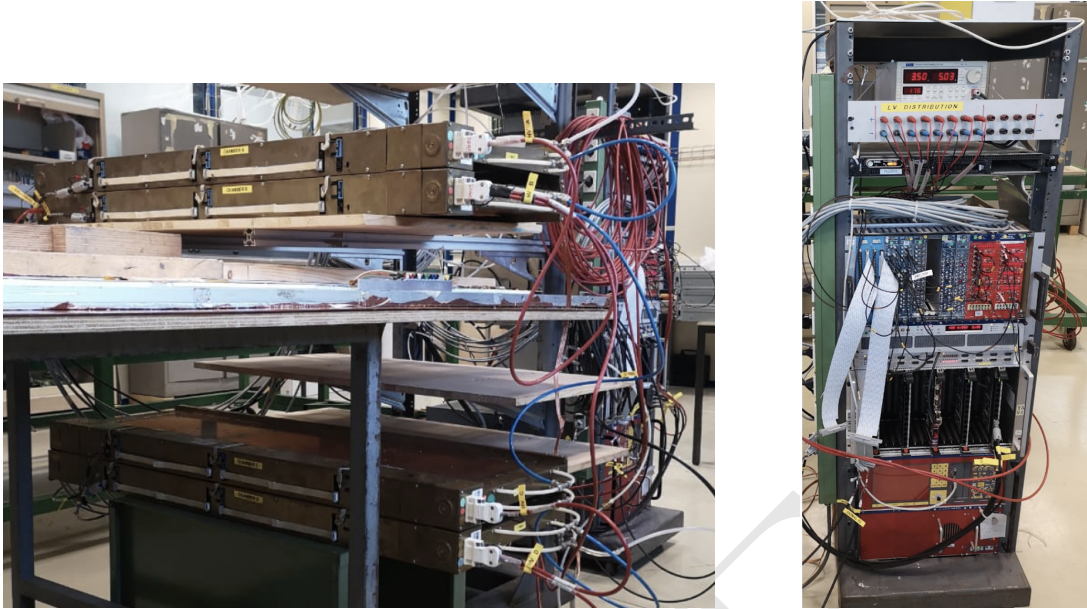


Figure 6.9: Left: Setup mounted for commissioning. Two MWPC chamber on the top (chambers A and B) and two (chambers C and D) on the bottom with a RPC R&D in the middle. Right: Rack with all the services for the operation of these chambers.

997 top planes of A and C is 570 mm. It is clear the the γ source has an impact on chamber A rate,
 998 but this is negligible when we take into account the coincidence between two chambers.

999 This two measurements were enough to validate this chambers as possible trigger pro RPC R&D
 1000 with cosmic muons in the laboratory and at GIF++. The next steps would be use this MWPC
 1001 chamber to implement a tracking system from triggering. This would demand some developments,
 1002 since, due to bandwidth restrictions, the signal from each FEB would have to go to a programmable
 1003 fast electronics, i.e. a FPGA, which would reconstruct muon tracks and provide the trigger to the
 1004 DAQ system. This can be done by placing the two pair of chambers (AB and CD) in orthogonal
 1005 configuration and read the signal in a CAEN V2495 board [89].

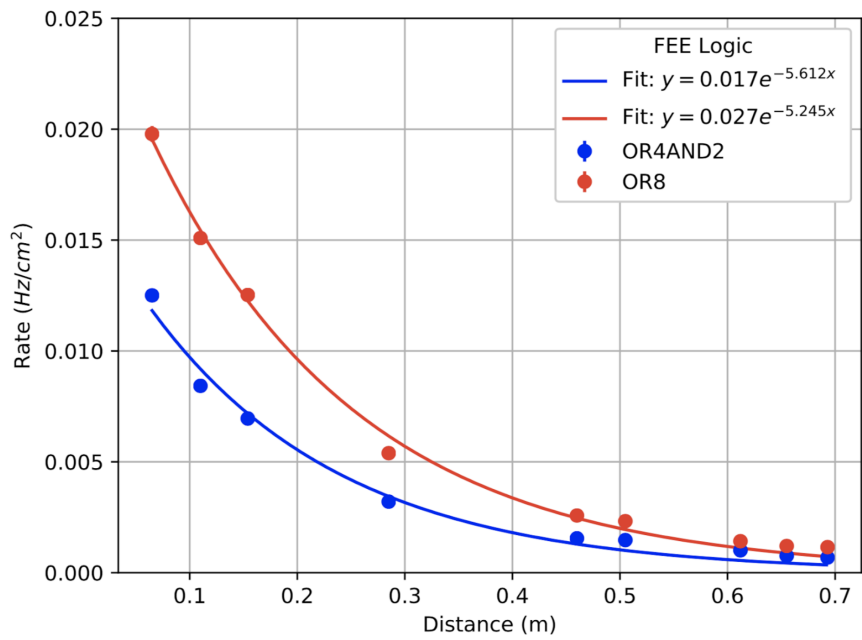


Figure 6.10: Coincidence rate of two chambers with respect to an arbitrary distance between the two top planes. Measured in 10 minutes, for 2 logical combinations (OR8 and OR4AND2). Applied high voltage: 2.65 kV. Threshold: 7 pC. Active area: readout of 160 mm x 160 mm per chamber.

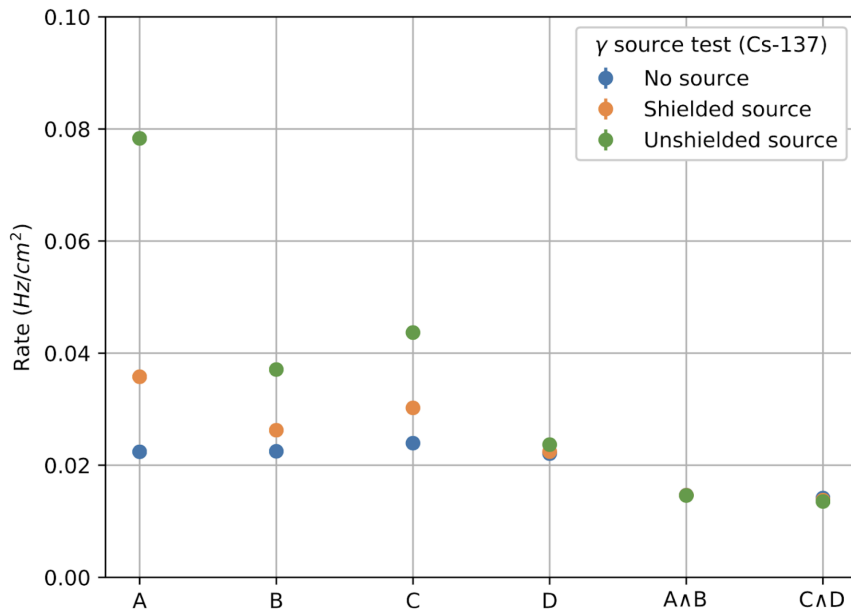


Figure 6.11: Individual rates (chambers A, B, C and D) and coincidence rates for two chambers (A AND B, C AND D), for without γ source (blue), a shielded γ source (orange) and an unshielded γ source (green). Source sitting on top of chamber A. Applied high voltage: 2.65 kV. Threshold: 7 pC. Active area: readout of 160 mm x 320 mm per chamber. Logical combination: AND2

1006 6.6 LS2 and the RPC Standard Maintenance

1007 In December 2018, the LS2 (Long Shutdown 2) was started. This a period in which the LHC
1008 and its detectors (CMS included) stop their operation for maintenance and upgrade. The LS2 will
1009 go up to 2021, when LHC and CMS restart the data taking with the Run3.

1010 During the LS2 it is being installed services for the new chambers (gas pipes, low voltage
1011 (LV), cables, signal and control optical fibers, high voltage (HV) cable and support equipment,
1012 and HV/LV power supplies), as well as continuity to the to the RPC R&D studies, besides the
1013 reparation of broken elements of the present system, i.e. chamber in the barrel region which present
1014 gas leak problems, maintenance of the LV and HV connectivity and power system, maintenance of
1015 the control system of problematic chambers (Front-Ends boards, cabling and Distribution Boards)
1016 and the dismount and reinstallation of four stations in the endcap (RE4) on both sides of CMS [90].

1017 What concerns the standard maintenance of the present RPC system, the main LS2 activities
1018 in which the student was involved, can be divided in three main tasks: (a) HV maintenance, (b)
1019 LV and control maintenance and (c) detector commissioning.

1020 6.6.1 HV maintenance

1021 A key factor of and RPC performance is the applied high voltage (HV). The CMS RPC achieve
1022 their optimal performance with, around, 9.5 kV applied in each gap. This voltage is in the range
1023 of the dielectric breakdown of many gases, which could lead to potential current leakages, if some
1024 part of the system is damaged, poorly operated or badly installed. If the currents are high enough
1025 this can make impossible the operation of the chamber. In cases like this, during the operation
1026 period (data taking), the problematic HV channel is identified and turned off (each chamber has
1027 two channels, one for each lawyer of gaps). Chambers in this situation are said to be operating in
1028 single gap mode (SG).

1029 The goal for the HV maintenance is to, now that the CMS is off and the chambers are accessible,
1030 identify which part of the HV supply system is causing the current leak and fix it the best way
1031 possible. Usually the problem is beyond the power supply, very often connectors or the gap itself
1032 are damaged.

1033 The CMS RPCs uses two kind of HV connectors, monopolar and tripolar connector. The
1034 monopolar are used to connect the chamber to the power supply. If mounted properly, rarely they
1035 present problems. The connection to the chamber is made by tripolar connectors, in which the
1036 ground and the HV for both gaps arrives to the chamber in a single connector, for simplicity and to
1037 save space in the patch panel. Unfortunately these connectors are relatively fragile, and they could
1038 be a potential source of leak, specially if they were poorly mounted, badly operated or with aging
1039 itself. Also, since this was a connector made exclusively for the CMS RPC system, some design
1040 choices had to be improved after the installation of other chamber. Those installed with old batches
1041 of tripolar connectors are sensitive ones. The reparation of this connectors consists in isolate the
1042 connector from the chamber and power it up to 15 kV (maximum voltage allowed by the system). If
1043 the tested connector is broken one will observe a very fast increase in the current of the HV channel.
1044 The only solution to this kind of problem is to replace the connector.

On the other hand, if the connector is powered isolated and pass the test, the problem beyond the connector (assuming that the power system have already been tested), i.e. inside the chamber. When a chamber is in SG mode it means that a full layer is off, but not necessarily all the gaps in that layer are bad (a RPC can have up to three per layer). In this situation, the procedure consists in cutting the cables that comes from the gaps to the chamber side connector one by one and identify which gap of the problematic layer is the broken by powering it. Once identified, this gap should isolated and the other ones reconnected. The broken gap is unrecoverable, since it is inside the chamber, but 5% to 10 % of efficiency can be retaken, without changing the applied HV and increasing the longevity of the chamber.

Another contribution to the HV maintenance was the proposal of a procedure to replace the problematic tripolar connector by a monopolar (also called jupiter) connector, which are known for being much more stable and reliable. The figure 6.12 (left) show the designed adapter for the chamber patch panel which would made this change possible. Figure 6.12 (right) shows a tryout of a chamber in which this procedure was tested. The proposal was presented to the RPC community and approved to be used from now on. Technical drawings and instructions were provided.

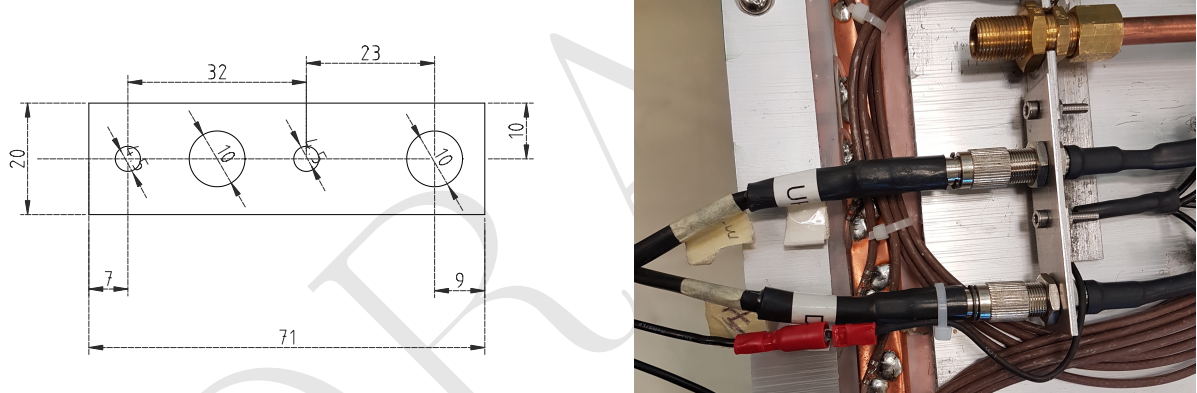


Figure 6.12: Left: Proposed adapter the chamber patch panel which make it possible to replace a tripolar by a jupiter HV connector. Right: Try out of the proposed HV connector replacement.

6.6.2 LV and control maintenance

The low voltage (LV) and control maintenance consists in make sure that the Front-End Boards (FEBs) are powered and configurable, which means that the LV power system is working from supply board to the cable, that the signal cables are in good state and properly connected to the chamber and to the link boards and that the on-detector electronics (FEBs and Distribution Boards - DBs) are working fine.

Usually, this system is very reliable. The weak point, in most of the cases, is the detector electronics. When a FEB [91] (as in Figure 6.13) is problematic it can present regions of very high noise or no signal at all (silent), which can not be recovered by the threshold control. In cases like this, when the FEB is accessible, it can be replaced in order to recover efficiency in the problematic chamber. This procedure is done by extracting the chamber from inside the detector (only for barrel chamber) and opening its cover to have access to the problematic component. Removed boards are send back to production labs for refurbishment.

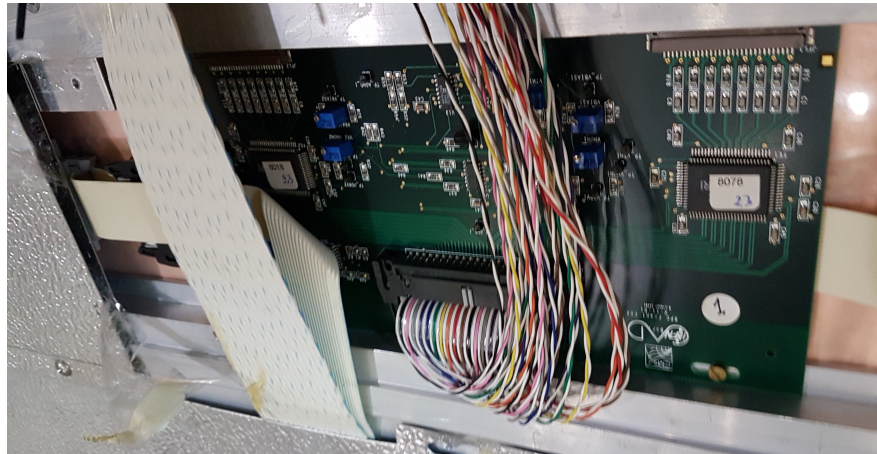


Figure 6.13: RPC Front-end board (FEB) used in the barrel chambers.

1073 The most usual problem is a chamber in which the threshold control was lost. For those chamber,
 1074 most probably, the problem is in the distribution board of the chamber, which is a piece of hardware
 1075 responsible for distribute the LV power to the FEBs (3 to 6 per chamber) and send the threshold
 1076 control signal to the FEBs via I2C line. If a chamber has no threshold control, it means that the
 1077 RPC operation has no control over the signal selection, which can potentially induce performance
 1078 issues.

1079 For the barrel this maintenance happens concomitantly with the gas leak reparations on the
 1080 barrel chamber, since both demands the chamber extraction, which is a complex procedure in terms
 1081 of operation and demands specialized equipment and manpower. For technical reasons, the gas leak
 1082 extractions have precedence over LV ones.

1083 6.6.3 Detector commissioning

1084 All the LS2 activities demands uncabling of the chamber to be repaired and possibly some
 1085 neighbor chambers. Also, it can involve the replacement of components of the chamber. To avoid
 1086 damage to the system a compromising procedure is needed after all this activities. Given the
 1087 responsibilities of the commissioning it was necessary to: (a) make sure that the the RPC system
 1088 keep tracks of all the interventions, (b) maintain all the algorithms used in the commissioning
 1089 procedure, (c) together with the RPC Coordination, define a pool of people and a schedule to the
 1090 commissioning of the system and (d) follow-up, with other CMS RPC experts, the availability of
 1091 materials and resources for the commissioning operations.

1092 Besides the organizational tasks, the commissioning demanded to establish procedures to ensure
 1093 the connectivity and functionality of HV and LV connections. For the HV, it is needed to make sure
 1094 that the chambers are properly connected, without miscabling³ and that the currents at stand-by
 1095 HV and working point HV are compatible with the ones in the end of last data-taking (end of
 1096 2018). This activity will start in November/2019, when the CMS RPC Standard Gas Mixture will
 1097 be available again.

³Mixed cable connections.

1098 For the LV point of view, the LV power cable and signal cables should also be properly connected,
 1099 and presenting a noise profile compatible with last data-taking. One key point for this task is to
 1100 make sure that there are no miscabling of signal cable. One RPC chamber can have from 6
 1101 to 18 signal cable, which are connected very close one to another. There is a good chance that a
 1102 chamber, after reparation, have its signal cables mixed. In order to diagnose situations like this, it
 1103 was validated a algorithm present in the RPC Online Software, but never used since LS1, which,
 1104 by changing the threshold of each component of the RPC system, from very high to very low values
 1105 (component by component), can spot miscabled chambers. Since the control line is independent of
 1106 the signal line, a misclabel will present a different noise from what is expected.

1107 Besides the validation of this algorithm, it was also implemented a web system (Figure 6.14),
 1108 developed in Flask [92] which automatize the execution of the algorithm, making transparent to the
 1109 shifter (or the one performing the commissioning) the procedure to get miscabling report.

FEB Connectivity Test - Analysis

Worker	Date (YY-MM-DD)	Time (HH:MM:SS)	Hash	
RBP2_Far	2019-06-20	23:43:19	387534dst	<button>Run Analyzer</button>
RBP1_Far	2019-06-20	20:12:20	458306dst	<button>Run Analyzer</button>
RBP1_Far	2019-06-20	20:04:46	336162dst	<button>Run Analyzer</button>
RBP1_Near	2019-06-20	19:02:00	377863dst	<button>Run Analyzer</button>
RBP1_Near	2019-06-19	18:59:00	858950dst	<button>Run Analyzer</button>
RBP1_Far	2019-06-19	18:58:26	994787dst	<button>Run Analyzer</button>
YEN3_Far	2019-05-07	10:28:23	176278dst	<button>Run Analyzer</button>
YEN3_Near	2019-05-07	10:28:08	347504dst	<button>Run Analyzer</button>
YEN1_Far	2018-12-07	15:03:24	575561	<button>Run Analyzer</button>
RBO_Far	2018-12-07	14:45:42	101463	<button>Run Analyzer</button>
RBP1_Far	2018-12-07	09:12:00	477689	<button>Run Analyzer</button>

Figure 6.14: RPC FEB Commissioning Analyzer.

1110 The LV commissioning is ongoing, since it happens, as much as possible, right after the chamber
 1111 reparation.

DRAFT

1112 Bibliography

- 1113 [1] Wikimedia Commons. *Standard Model*. 2020. URL: https://en.wikipedia.org/wiki/File:Standard_Model_of_Elementary_Particles.svg.
- 1114
- 1115 [2] C. Patrignani et al. “Review of Particle Physics”. In: *Chin. Phys. C* 40.10 (2016), p. 100001.
- 1116 DOI: 10.1088/1674-1137/40/10/100001.
- 1117 [3] A. Salam and J. C. Ward. “On a gauge theory of elementary interactions”. In: *Il Nuovo Cimento (1955-1965)* 19.1 (1961), pp. 165–170. DOI: 10.1007/BF02812723. URL: <https://doi.org/10.1007/BF02812723>.
- 1118
- 1119
- 1120 [4] G. Aad et al. “Observation of a new particle in the search for the Standard Model Higgs boson with the ATLAS detector at the LHC”. In: *Physics Letters B* 716.1 (2012), pp. 1–29. ISSN: 0370-2693. DOI: <https://doi.org/10.1016/j.physletb.2012.08.020>. URL: <http://www.sciencedirect.com/science/article/pii/S037026931200857X>.
- 1121
- 1122
- 1123
- 1124 [5] Serguei Chatrchyan et al. “Observation of a new boson at a mass of 125 GeV with the CMS experiment at the LHC”. In: *Phys. Lett. B* 716 (2012), pp. 30–61. DOI: 10.1016/j.physletb.2012.08.021. arXiv: 1207.7235 [hep-ex].
- 1125
- 1126
- 1127 [6] Geoffrey Bodwin et al. “Higgs boson decays to quarkonia and the $H\bar{c}c$ coupling”. In: *Phys. Rev. D* 88 (5 Sept. 2013), p. 053003. DOI: 10.1103/PhysRevD.88.053003. URL: <https://link.aps.org/doi/10.1103/PhysRevD.88.053003>.
- 1128
- 1129
- 1130 [7] Geoffrey T. Bodwin et al. “Relativistic corrections to Higgs boson decays to quarkonia”. In: *Phys. Rev. D* 90 (11 Dec. 2014), p. 113010. DOI: 10.1103/PhysRevD.90.113010. URL: <https://link.aps.org/doi/10.1103/PhysRevD.90.113010>.
- 1131
- 1132
- 1133 [8] G. Aad, B. Abbott, et al. “Combined Measurement of the Higgs Boson Mass in pp Collisions at $\sqrt{s} = 7$ and 8 TeV with the ATLAS and CMS Experiments”. In: *Phys. Rev. Lett.* 114 (19 May 2015), p. 191803. DOI: 10.1103/PhysRevLett.114.191803. URL: <https://link.aps.org/doi/10.1103/PhysRevLett.114.191803>.
- 1134
- 1135
- 1136
- 1137 [9] Cédric Delaunay et al. “Enhanced Higgs boson coupling to charm pairs”. In: *Phys. Rev. D* 89 (3 Feb. 2014), p. 033014. DOI: 10.1103/PhysRevD.89.033014. URL: <https://link.aps.org/doi/10.1103/PhysRevD.89.033014>.
- 1138
- 1139
- 1140 [10] M. A. PÉREZ, G. TAVARES-VELASCO, and J. J. TOSCANO. “NEW PHYSICS EFFECTS IN RARE Z DECAYS”. In: *International Journal of Modern Physics A* 19.02 (2004), pp. 159–178. DOI: 10.1142/S0217751X04017100.
- 1141
- 1142

- [11] Grossman, Yuval and König, Matthias and Neubert, Matthias. “Exclusive radiative decays of W and Z bosons in QCD factorization”. In: *Journal of High Energy Physics* 2015.4 (Apr. 2015), p. 101. ISSN: 1029-8479. DOI: 10.1007/JHEP04(2015)101. URL: [https://doi.org/10.1007/JHEP04\(2015\)101](https://doi.org/10.1007/JHEP04(2015)101).
- [12] Geoffrey T. Bodwin et al. “Z-boson decays to a vector quarkonium plus a photon”. In: *Phys. Rev. D* 97 (1 Jan. 2018), p. 016009. DOI: 10.1103/PhysRevD.97.016009. URL: <https://link.aps.org/doi/10.1103/PhysRevD.97.016009>.
- [13] Geoffrey T. Bodwin et al. “Addendum: New approach to the resummation of logarithms in Higgs-boson decays to a vector quarkonium plus a photon [Phys. Rev. D 95, 054018 (2017)]”. In: *Phys. Rev. D* 96 (11 Dec. 2017), p. 116014. DOI: 10.1103/PhysRevD.96.116014. URL: <https://link.aps.org/doi/10.1103/PhysRevD.96.116014>.
- [14] Gino Isidori, Aneesh V. Manohar, and Michael Trott. “Probing the nature of the Higgs-like boson via $h \rightarrow Vf$ decays”. In: *Physics Letters B* 728 (2014), pp. 131–135. ISSN: 0370-2693. DOI: <https://doi.org/10.1016/j.physletb.2013.11.054>. URL: <http://www.sciencedirect.com/science/article/pii/S037026931300960X>.
- [15] Alexander L. Kagan et al. “Exclusive Window onto Higgs Yukawa Couplings”. In: *Phys. Rev. Lett.* 114 (10 Mar. 2015), p. 101802. DOI: 10.1103/PhysRevLett.114.101802. URL: <https://link.aps.org/doi/10.1103/PhysRevLett.114.101802>.
- [16] Dao-Neng Gao. “A note on Higgs decays into Z boson and $J/\psi(\Upsilon)$ ”. In: *Physics Letters B* 737 (2014), pp. 366–368. ISSN: 0370-2693. DOI: <https://doi.org/10.1016/j.physletb.2014.09.019>. URL: <http://www.sciencedirect.com/science/article/pii/S0370269314006698>.
- [17] A. M. Sirunyan et al. “Observation of Higgs Boson Decay to Bottom Quarks”. In: *Phys. Rev. Lett.* 121 (12 Sept. 2018), p. 121801. DOI: 10.1103/PhysRevLett.121.121801. URL: <https://link.aps.org/doi/10.1103/PhysRevLett.121.121801>.
- [18] G Apollinari et al. *High-Luminosity Large Hadron Collider (HL-LHC): Preliminary Design Report*. CERN Yellow Reports: Monographs. Geneva: CERN, 2015. DOI: 10.5170/CERN-2015-005. URL: <https://cds.cern.ch/record/2116337>.
- [19] The ATLAS Collaboration et al. “The ATLAS Experiment at the CERN Large Hadron Collider”. In: *Journal of Instrumentation* 3.08 (Aug. 2008), S08003–S08003. DOI: 10.1088/1748-0221/3/08/s08003. URL: <https://doi.org/10.1088%2F1748-0221%2F3%2F08%2Fs08003>.
- [20] G. Aad et al. “Search for Higgs and Z Boson Decays to $J/\psi\gamma$ and $\Upsilon(nS)\gamma$ with the ATLAS Detector”. In: *Phys. Rev. Lett.* 114 (12 Mar. 2015), p. 121801. DOI: 10.1103/PhysRevLett.114.121801. URL: <https://link.aps.org/doi/10.1103/PhysRevLett.114.121801>.
- [21] Morad Aaboud et al. “Searches for exclusive Higgs and Z boson decays into $J/\psi\gamma$, $\psi(2S)\gamma$, and $\Upsilon(nS)\gamma$ at $\sqrt{s} = 13$ TeV with the ATLAS detector”. In: *Phys. Lett. B* 786 (2018), pp. 134–155. DOI: 10.1016/j.physletb.2018.09.024. arXiv: 1807.00802 [hep-ex].
- [22] S. Chatrchyan et al. “The CMS experiment at the CERN LHC”. In: *JINST* 3 (2008), S08004. DOI: 10.1088/1748-0221/3/08/S08004.

- 1181 [23] Albert M Sirunyan et al. “Search for rare decays of Z and Higgs bosons to J/ψ and a photon
1182 in proton-proton collisions at $\sqrt{s} = 13$ TeV”. In: *Eur. Phys. J.* C79.2 (2019), p. 94. DOI:
1183 10.1140/epjc/s10052-019-6562-5. arXiv: 1810.10056 [hep-ex].
- 1184 [24] Albert M Sirunyan et al. “Search for Higgs and Z boson decays to J/ψ or Υ pairs in proton-
1185 proton collisions at $\sqrt{s} = 13$ TeV”. In: *Phys. Lett. B* 797.arXiv:1905.10408. CMS-HIG-18-025-
1186 003 (May 2019). All figures and tables can be found at <http://cms-results.web.cern.ch/cms->
1187 results/public-results/publications/HIG-18-025 (CMS Public Pages), 134811. 31 p. DOI: 10.
1188 1016/j.physletb.2019.134811. URL: <https://cds.cern.ch/record/2676242>.
- 1189 [25] Albert M. Sirunyan et al. “Observation of the $Z \rightarrow \psi\ell^+\ell^-$ decay in pp collisions at $\sqrt{s} =$
1190 13 TeV”. In: *Phys. Rev. Lett.* 121.arXiv:1806.04213. CMS-BPH-16-001-003 (June 2018). Sub-
1191 mitted to *Phys.Rev.Lett.*, 141801. 17 p. DOI: 10.1103/PhysRevLett.121.141801. URL:
1192 <https://cds.cern.ch/record/2623687>.
- 1193 [26] Serguei Chatrchyan et al. “Description and performance of track and primary-vertex recon-
1194 struction with the CMS tracker”. In: *JINST* 9 (2014), P10009. DOI: 10.1088/1748-0221/9/
1195 10/P10009. arXiv: 1405.6569 [physics.ins-det].
- 1196 [27] Vardan Khachatryan et al. “Performance of electron reconstruction and selection with the
1197 CMS detector in proton-proton collisions at $\sqrt{s} = 8$ TeV”. In: *JINST* 10 (2015), P06005. DOI:
1198 10.1088/1748-0221/10/06/P06005. arXiv: 1502.02701 [physics.ins-det].
- 1199 [28] Vardan Khachatryan et al. “Performance of photon reconstruction and identification with the
1200 CMS detector in proton-proton collisions at $\sqrt{s} = 8$ TeV”. In: *JINST* 10 (2015), P08010. DOI:
1201 10.1088/1748-0221/10/08/P08010. arXiv: 1502.02702 [physics.ins-det].
- 1202 [29] A M Sirunyan et al. “Performance of the CMS muon detector and muon reconstruction with
1203 proton-proton collisions at $\sqrt{s} = 13$ TeV”. In: *JINST* 13 (2018), P06015. DOI: 10.1088/1748-
1204 0221/13/06/P06015. arXiv: 1804.04528 [physics.ins-det].
- 1205 [30] Vardan Khachatryan et al. “The CMS trigger system”. In: *JINST* 12 (2017), P01020. DOI:
1206 10.1088/1748-0221/12/01/P01020. arXiv: 1609.02366 [physics.ins-det].
- 1207 [31] S. Chatrchyan et al. “The CMS experiment at the CERN LHC”. In: *JINST* 3 (2008), S08004.
1208 DOI: 10.1088/1748-0221/3/08/S08004.
- 1209 [32] *CMS Luminosity Measurements for the 2016 Data Taking Period*. Tech. rep. CMS-PAS-LUM-
1210 17-001. Geneva: CERN, 2017. URL: <https://cds.cern.ch/record/2257069>.
- 1211 [33] S. Agostinelli et al. “GEANT4—a simulation toolkit”. In: A506 (2003), pp. 250–303. DOI:
1212 10.1016/S0168-9002(03)01368-8.
- 1213 [34] Paolo Nason. “A New method for combining NLO QCD with shower Monte Carlo algorithms”.
1214 In: *JHEP* 11 (2004), p. 040. DOI: 10.1088/1126-6708/2004/11/040. arXiv: hep-ph/0409146
1215 [hep-ph].
- 1216 [35] Stefano Frixione, Paolo Nason, and Carlo Oleari. “Matching NLO QCD computations with
1217 Parton Shower simulations: the POWHEG method”. In: *JHEP* 11 (2007), p. 070. DOI: 10.
1218 1088/1126-6708/2007/11/070. arXiv: 0709.2092 [hep-ph].

- [36] Simone Alioli et al. “A general framework for implementing NLO calculations in shower Monte Carlo programs: the POWHEG BOX”. In: *JHEP* 06 (2010), p. 043. DOI: 10.1007/JHEP06(2010)043. arXiv: 1002.2581 [hep-ph].
- [37] Abdelhak Djouadi. “The anatomy of electroweak symmetry breaking: Tome I: The Higgs boson in the Standard Model”. In: *Physics Reports* 457.1 (2008), pp. 1–216. ISSN: 0370-1573. DOI: <https://doi.org/10.1016/j.physrep.2007.10.004>. URL: <http://www.sciencedirect.com/science/article/pii/S0370157307004334>.
- [38] Torbjörn Sjöstrand, Stephen Mrenna, and Peter Skands. “A brief introduction to PYTHIA 8.1”. In: *Computer Physics Communications* 178.11 (2008), pp. 852–867. ISSN: 0010-4655. DOI: <https://doi.org/10.1016/j.cpc.2008.01.036>. URL: <http://www.sciencedirect.com/science/article/pii/S0010465508000441>.
- [39] Torbjörn Sjöstrand et al. “An Introduction to PYTHIA 8.2”. In: *Comput. Phys. Commun.* 191 (2015), pp. 159–177. DOI: 10.1016/j.cpc.2015.01.024. arXiv: 1410.3012 [hep-ph].
- [40] Vardan Khachatryan et al. “Event generator tunes obtained from underlying event and multi-parton scattering measurements”. In: *Eur. Phys. J. C* 76.3 (2016), p. 155. DOI: 10.1140/epjc/s10052-016-3988-x. arXiv: 1512.00815 [hep-ex].
- [41] The NNPDF collaboration et al. “Parton distributions for the LHC run II”. In: *Journal of High Energy Physics* 2015.4 (Apr. 2015), p. 40. ISSN: 1029-8479. DOI: 10.1007/JHEP04(2015)040. URL: [https://doi.org/10.1007/JHEP04\(2015\)040](https://doi.org/10.1007/JHEP04(2015)040).
- [42] J. Alwall et al. “The automated computation of tree-level and next-to-leading order differential cross sections, and their matching to parton shower simulations”. In: *Journal of High Energy Physics* 2014.7 (July 2014), p. 79. ISSN: 1029-8479. DOI: 10.1007/JHEP07(2014)079. URL: [https://doi.org/10.1007/JHEP07\(2014\)079](https://doi.org/10.1007/JHEP07(2014)079).
- [43] Ali Abbasabadi et al. “Radiative Higgs boson decays $H \rightarrow f\bar{f}\gamma$ ”. In: *Phys. Rev. D* 55 (9 May 1997), pp. 5647–5656. DOI: 10.1103/PhysRevD.55.5647. URL: <https://link.aps.org/doi/10.1103/PhysRevD.55.5647>.
- [44] D. de Florian et al. *Handbook of LHC Higgs Cross Sections: 4. Deciphering the Nature of the Higgs Sector*. CERN Yellow Reports: Monographs. 869 pages, 295 figures, 248 tables and 1645 citations. Working Group web page: <https://twiki.cern.ch/twiki/bin/view/LHCPhysics/LHCHXSWG>. Oct. 2016. DOI: 10.23731/CYRM-2017-002. URL: <https://cds.cern.ch/record/2227475>.
- [45] Ye Li and Frank Petriello. “Combining QCD and electroweak corrections to dilepton production in the framework of the FEWZ simulation code”. In: *Phys. Rev. D* 86 (9 Nov. 2012), p. 094034. DOI: 10.1103/PhysRevD.86.094034. URL: <https://link.aps.org/doi/10.1103/PhysRevD.86.094034>.
- [46] John M. Campbell and R.K. Ellis. “MCFM for the Tevatron and the LHC”. In: *Nuclear Physics B - Proceedings Supplements* 205-206 (2010). Loops and Legs in Quantum Field Theory, pp. 10–15. ISSN: 0920-5632. DOI: <https://doi.org/10.1016/j.nuclphysbps.2010.08.011>. URL: <http://www.sciencedirect.com/science/article/pii/S0920563210001945>.

- 1257 [47] Vardan Khachatryan et al. “Search for a Higgs boson decaying into $\gamma^*\gamma \rightarrow \ell\ell\gamma$ with low
1258 dilepton mass in pp collisions at $\sqrt{s} = 8$ TeV”. In: *Phys. Lett.* B753 (2016), pp. 341–362. DOI:
1259 10.1016/j.physletb.2015.12.039. arXiv: 1507.03031 [hep-ex].
- 1260 [48] N. Brambilla, S. Eidelman, B.K. Heltsley, et al. “Heavy quarkonium: progress, puzzles, and
1261 opportunities”. In: *The European Physical Journal C* 71.2 (Feb. 2011), p. 1534. ISSN: 1434-
1262 6052. DOI: 10.1140/epjc/s10052-010-1534-9. URL: <https://doi.org/10.1140/epjc/s10052-010-1534-9>.
- 1264 [49] Sandro Palestini. “Angular distribution and rotations of frame in vector meson decays into
1265 lepton pairs”. In: *Phys. Rev. D* 83 (3 Feb. 2011), p. 031503. DOI: 10.1103/PhysRevD.83.
1266 031503. URL: <https://link.aps.org/doi/10.1103/PhysRevD.83.031503>.
- 1267 [50] A.M. Sirunyan et al. “Particle-flow reconstruction and global event description with the CMS
1268 detector”. In: *Journal of Instrumentation* 12.10 (2017), P10003. URL: <http://stacks.iop.org/1748-0221/12/i=10/a=P10003>.
- 1270 [51] Matteo Cacciari, Gavin P. Salam, and Gregory Soyez. “The anti- k_t jet clustering algorithm”.
1271 In: *JHEP* 04 (2008), p. 063. DOI: 10.1088/1126-6708/2008/04/063. arXiv: 0802.1189
1272 [hep-ex].
- 1273 [52] Matteo Cacciari, Gavin P. Salam, and Gregory Soyez. “FastJet User Manual”. In: *Eur. Phys. J.*
1274 C72 (2012), p. 1896. DOI: 10.1140/epjc/s10052-012-1896-2. arXiv: 1111.6097 [hep-ph].
- 1275 [53] Albert M Sirunyan et al. “Measurements of properties of the Higgs boson decaying into the
1276 four-lepton final state in pp collisions at $\sqrt{s} = 13$ TeV”. In: *JHEP* 11 (2017), p. 047. DOI:
1277 10.1007/JHEP11(2017)047. arXiv: 1706.09936 [hep-ex].
- 1278 [54] V. Khachatryan et al. “Observation of the diphoton decay of the Higgs boson and measurement
1279 of its properties”. In: *The European Physical Journal C* 74.10 (Oct. 2014), p. 3076. ISSN: 1434-
1280 6052. DOI: 10.1140/epjc/s10052-014-3076-z. URL: <https://doi.org/10.1140/epjc/s10052-014-3076-z>.
- 1282 [55] S. Bernstein. “Démonstration du théorème de Weierstrass fondée sur le calcul des probabilités”. In: *Commun. Soc. Math. Kharkov* 13.1–2 (1912).
- 1284 [56] John Erthal Gaiser. “Charmonium Spectroscopy From Radiative Decays of the J/ψ and ψ' ”.
1285 PhD thesis. SLAC, 1982. URL: <http://www-public.slac.stanford.edu/sciDoc/docMeta.aspx?slacPubNumber=slac-r-255.html>.
- 1287 [57] P. D. Dauncey et al. “Handling uncertainties in background shapes: the discrete profiling
1288 method”. In: *JINST* 10.04 (2015), P04015. DOI: 10.1088/1748-0221/10/04/P04015. arXiv:
1289 1408.6865 [physics.data-an].
- 1290 [58] S. S. Wilks. “The Large-Sample Distribution of the Likelihood Ratio for Testing Compos-
1291 itive Hypotheses”. In: *Ann. Math. Statist.* 9.1 (Mar. 1938), pp. 60–62. DOI: 10.1214/aoms/1177732360. URL: <https://doi.org/10.1214/aoms/1177732360>.
- 1293 [59] Higgs to Gamma Gamma Working Group. *Further measurement of $H \rightarrow \gamma\gamma$ at $\sqrt{13}$ TeV*.
1294 CMS Note 2016/209. CERN, 2016. URL: http://cms.cern.ch/iCMS/jsp/db_notes/noteInfo.jsp?cmsnoteid=CMS%20AN-2016/209.

- [60] Updated measurements of Higgs boson production in the diphoton decay channel at $\sqrt{s} = 13\text{ TeV}$ in pp collisions at CMS. Tech. rep. CMS-PAS-HIG-16-020. Geneva: CERN, 2016. URL: <http://cds.cern.ch/record/2205275>.
- [61] D. de Florian et al. “Handbook of LHC Higgs Cross Sections: 4. Deciphering the Nature of the Higgs Sector”. In: (2016). DOI: 10.23731/CYRM-2017-002. arXiv: 1610.07922 [hep-ph].
- [62] Jon Butterworth et al. “PDF4LHC recommendations for LHC Run II”. In: *J. Phys.* G43 (2016), p. 023001. DOI: 10.1088/0954-3899/43/2/023001. arXiv: 1510.03865 [hep-ph].
- [63] A. D. Martin et al. “Parton distributions for the LHC”. In: *Eur. Phys. J.* C63 (2009), pp. 189–285. DOI: 10.1140/epjc/s10052-009-1072-5. arXiv: 0901.0002 [hep-ph].
- [64] Hung-Liang Lai et al. “New parton distributions for collider physics”. In: *Phys. Rev.* D82 (2010), p. 074024. DOI: 10.1103/PhysRevD.82.074024. arXiv: 1007.2241 [hep-ph].
- [65] Sergey Alekhin et al. “The PDF4LHC Working Group Interim Report”. In: (2011). arXiv: 1101.0536 [hep-ph].
- [66] Michiel Botje et al. “The PDF4LHC Working Group Interim Recommendations”. In: (2011). arXiv: 1101.0538 [hep-ph].
- [67] Richard D. Ball et al. “Impact of Heavy Quark Masses on Parton Distributions and LHC Phenomenology”. In: *Nucl. Phys.* B849 (2011), pp. 296–363. DOI: 10.1016/j.nuclphysb.2011.03.021. arXiv: 1101.1300 [hep-ph].
- [68] Giampiero Passarino. “Higgs Boson Production and Decay: Dalitz Sector”. In: *Phys. Lett.* B727 (2013), pp. 424–431. DOI: 10.1016/j.physletb.2013.10.052. arXiv: 1308.0422 [hep-ph].
- [69] A L Read. “Presentation of search results: the CL_{st} technique”. In: *Journal of Physics G: Nuclear and Particle Physics* 28.10 (Sept. 2002), pp. 2693–2704. DOI: 10.1088/0954-3899/28/10/313. URL: <https://doi.org/10.1088/0954-3899/28/10/313>.
- [70] J. Neyman and E. S. Pearson. “On the Problem of the Most Efficient Tests of Statistical Hypotheses”. In: *Philosophical Transactions of the Royal Society of London. Series A, Containing Papers of a Mathematical or Physical Character* 231 (1933), pp. 289–337. ISSN: 02643952. URL: <http://www.jstor.org/stable/91247>.
- [71] Glen Cowan et al. “Asymptotic formulae for likelihood-based tests of new physics”. In: *The European Physical Journal C* 71.2 (Feb. 2011), p. 1554. ISSN: 1434-6052. DOI: 10.1140/epjc/s10052-011-1554-0. URL: <https://doi.org/10.1140/epjc/s10052-011-1554-0>.
- [72] Procedure for the LHC Higgs boson search combination in Summer 2011. Tech. rep. CMS-NOTE-2011-005. ATL-PHYS-PUB-2011-11. Geneva: CERN, Aug. 2011. URL: <http://cds.cern.ch/record/1379837>.
- [73] M. Aaboud et al. “Searches for exclusive Higgs and Z boson decays into $J/\psi\gamma$, $\psi(2S)\gamma$, and $\Upsilon(nS)\gamma$ at $\sqrt{s} = 13\text{TeV}$ with the ATLAS detector”. In: *Physics Letters B* 786 (Nov. 2018), pp. 134–155. ISSN: 0370-2693. DOI: 10.1016/j.physletb.2018.09.024. URL: <http://dx.doi.org/10.1016/j.physletb.2018.09.024>.

- 1334 [74] R. Santonico and R. Cardarelli. "Development of resistive plate counters". In: *Nuclear Instruments and Methods in Physics Research* 187.2 (1981), pp. 377–380. ISSN: 0167-5087. DOI: [https://doi.org/10.1016/0029-554X\(81\)90363-3](https://doi.org/10.1016/0029-554X(81)90363-3). URL: <http://www.sciencedirect.com/science/article/pii/0029554X81903633>.
- 1335
- 1336
- 1337
- 1338 [75] Marcello Abbrescia, Paulo Fonte, and Vladimir Peskov. *Resistive gaseous detectors: designs, performance, and perspectives*. Weinheim: Wiley-VCH, 2018. DOI: 10.1002/9783527698691.
- 1339
- 1340 [76] *The CMS muon project: Technical Design Report*. Technical Design Report CMS. Geneva: CERN, 1997. URL: <https://cds.cern.ch/record/343814>.
- 1341
- 1342 [77] P. Bernardini et al. "Precise measurements of drift velocities in helium gas mixtures". In: *Nuclear Instruments and Methods in Physics Research Section A: Accelerators, Spectrometers, Detectors and Associated Equipment* 355.2 (1995), pp. 428–433. ISSN: 0168-9002. DOI: [https://doi.org/10.1016/0168-9002\(94\)01144-3](https://doi.org/10.1016/0168-9002(94)01144-3). URL: <http://www.sciencedirect.com/science/article/pii/0168900294011443>.
- 1343
- 1344
- 1345
- 1346
- 1347 [78] E. Gorini et al. "Drift velocity measurements in C₂H₂F₄ based mixtures". In: *Proceedings of the 4th International Workshop on Resistive Plate Chamber and Related Detectors, in Napoli, Italy, 15-16 October* (1997).
- 1348
- 1349
- 1350 [79] Andrea Gelmi. *Longevity studies for the CMS-RPC system*. Tech. rep. CMS-CR-2018-136. Geneva: CERN, July 2018. URL: <https://cds.cern.ch/record/2634505>.
- 1351
- 1352 [80] *Public CMS Data Quality Information*. twiki.cern.ch/twiki/bin/view/CMSPublic/DataQuality. Acessado em: 20/02/2018.
- 1353
- 1354 [81] Johannes Gutleber, Steven Murray, and Luciano Orsini. "Towards a homogeneous architecture for high-energy physics data acquisition systems". In: *Computer Physics Communications* 153.2 (2003), pp. 155–163. ISSN: 0010-4655. DOI: [https://doi.org/10.1016/S0010-4655\(03\)00161-9](https://doi.org/10.1016/S0010-4655(03)00161-9). URL: <http://www.sciencedirect.com/science/article/pii/S0010465503001619>.
- 1355
- 1356
- 1357
- 1358
- 1359 [82] *Dojo*. <https://dojotoolkit.org/>. Acessado em: 20/02/2018.
- 1360 [83] *Polymer Project*. Acessado em: 20/02/2018.
- 1361 [84] M. I. Pedraza-Morales. *RPC upgrade project for CMS Phase II*. 2018. arXiv: 1806.11503 [physics.ins-det].
- 1362
- 1363 [85] Dorothea Pfeiffer et al. "The radiation field in the Gamma Irradiation Facility GIF++ at CERN". In: *Nuclear Instruments and Methods in Physics Research Section A: Accelerators, Spectrometers, Detectors and Associated Equipment* 866 (2017), pp. 91–103. ISSN: 0168-9002. DOI: <https://doi.org/10.1016/j.nima.2017.05.045>. URL: <http://www.sciencedirect.com/science/article/pii/S0168900217306113>.
- 1364
- 1365
- 1366
- 1367
- 1368 [86] A. Augusto Alves Jr. et al. "The LHCb Detector at the LHC". In: *JINST* 3 (2008), S08005. DOI: 10.1088/1748-0221/3/08/S08005.
- 1369
- 1370 [87] Georges Charpak et al. "The Use of Multiwire Proportional Counters to Select and Localize Charged Particles". In: *Nucl. Instrum. Meth.* 62 (1968), pp. 262–268. DOI: 10.1016/0029-554X(68)90371-6.
- 1371
- 1372

- 1373 [88] *LHCb Muon Group Home Page*. [Online; accessed 1-October-2019]. 2019. URL: <http://lhcb-muon.web.cern.ch/lhcb-muon/>.
- 1374
- 1375 [89] *CAEN Programmable Logic Unit - V2495*. [Online; accessed 1-October-2019]. 2019. URL: <https://www.caen.it/products/v2495/>.
- 1376
- 1377 [90] *Resistive Plate Chambers are getting dolled up*. <https://cms.cern/news/resistive-plate-chambers-are-getting-dolled>. Acessado em: 20/09/2019.
- 1378
- 1379 [91] C. Binetti et al. “A new Front-End board for RPC detector of CMS”. In: (Sept. 1999).
- 1380 [92] *Flask (web framework)*. [Online; accessed 1-October-2019]. 2019. URL: <https://palletsprojects.com/p/flask/>.
- 1381